Measurement of the Λ_B Lifetime in the Decay Mode $\Lambda_b \rightarrow J/\psi\Lambda$

A thesis presented

by

Robyn Madrak

to

The Department of Physics

in partial fulfillment of the requirements

for the degree of

Doctor of Philosophy

in the subject of

Physics

Harvard University

Cambridge, Massachusetts

September 2003

Thesis advisor

Melissa Franklin

Author

Robyn Madrak

Measurement of the Λ_B Lifetime in the Decay Mode $\Lambda_b \to J/\psi\Lambda$

Abstract

This thesis describes a measurement of the $\Lambda_B(5624)$ lifetime in the exclusive decay mode $\Lambda_b \to J/\psi\Lambda$, with $J/\psi \to \mu^+\mu^-$ and $\Lambda \to p^+\pi^-$. This is the first measurement of the Λ_B lifetime in a mode where the Λ_B is fully reconstructed. As a control sample, we use the decay mode $B^0 \to J/\psi K^0_s$, with $J/\psi \to \mu^+\mu^-$ and $K^0_s \to \pi^+\pi^-$.

We obtain 46 ± 9 Λ_B and 256 ± 15 B^0 candidate decays in 65 pb^{-1} of $p\bar{p}$ collision data collected by the CDF II experiment at Fermilab. We obtain the value

$$\tau(\Lambda_B) = 1.25 \pm 0.26(stat.) \pm 0.14(syst.)\text{ps}$$

Time is not measured by a watch, but by moments.

— Fortune cookie from the restaurant “Chopsticks”, in Warrenville, IL

Acknowledgements

I want to thank Melissa for demanding that things make sense, and that I understood them, and putting up with me (I know I must have been a real pain) and for rathergood.com, which allowed me to maintain my (in)sanity while finishing up this analysis. She has helped me such a tremendous ammount, especially in writing this thesis. Besides all this, she is a great and understanding person, who is very kind. Andy was also a huge help, in understanding the theory and closing the loop on the analysis. He also tried very hard to get those people at Dali to let me keep my wine bottles. I want to thank Bill that I am happy - it really is possible! I simply cannot believe how lucky I am. I could not have survived without his support throughout this whole thing. I want to thank Aseet and Ken for the most fun time of my life. Both have spent so much time teaching me all of the things that I love to do. And what would I do without coffee breaks? I don't think I can ever thank either of them enough. Thanks to Bob Wagner for being the courageous leader of the COT project, and for many lunches at St. Thomas during the COT construction. The whole COT bunch, Morris, Eiko, Dave Ambrose, Ting, Jim Welch, to name a few, were all fun to work with. Rick Haggerty was right on in saying that "some days are diamond, some days are rock". I had many diamond days in the basement of HEPL. Thanks to

Rick for teaching me so much and letting me use his good vernier calipers. Thanks to Steve for his wonderful machining and helping me clean the epoxy off of the granite table. To Dignan for drinking Guiness with me. George Brandenburg is a terrific guy, the director of HEPL, a place I feel at home. He always made sure things were done fairly for the grad students. Thanks Mom for teaching me the value of being careful, and precise, and Dad for teaching me how to think, and helping me believe that it is OK not to be just like everyone else. My Gramma Madrak is a true saint. My cousin Alissa and I had some of our best times at her summer cottage, but we made a mess! Nothing comes close to Christmas Eve dinner at the Madraks'. Thank you Grandma and Poppop Magda for praying for me during my defense, for saying "I know", and for wonderful childhood memories. Janine has been my lifelong best friend. There are things only she understands. If not for her, right now I might be living in the "gutter" with a shaved head, safety pins in my ear, and no money. Wait a minute, I have no money... Of course I must thank Janine's parents for wonderful times, and pierogies. They fed me for all of those years and we laughed alot. Snag is a true lover of science, and it was catchy. He has encouraged me as far back as I can remember. Mr. Wasilewski started my interest in physics. He was the best teacher, and so different from the rest. Ritchie Patterson introduced me to drift chambers for the first time when I worked for her as an undergrad. These are among the coolest things in all of physics. I want thank Daniel Kim, Chung, Tempkin for doing E&M, and watching Beavis and Butthead with me and Joao for making it possible for me to do work by getting these computers and Kevin for helping me realize I shouldn't mass contrain the Lambda to the Kshort mass. Kevin deserves a page of thanks just for reading my thesis and the very good comments he had. Thank you Carter, for

saying that I am cool in your thesis acknowledgements - I think you are cool! I think we will be forever bonded after those nights measuring field sheet heights, with the neverending beep-beep of the DVM. Ayana was a great friend and is the best artist I know. I am grateful to her, Daniel, and John Paul for being a great audience at my thesis defense. Thank you Lester for buying me beer later that night, and Sal for being a great cook! I am completely sure without a shred of doubt that doing a Run II thesis was the right thing for me. I want to thank Marjorie Shapiro for encouraging me in this endeavor. Thanks to Tom Lecompte for leading the jpsi group, and many interesting stories... Thanks to Mary Bishai, Ting Miao and Slawek Tkaczyk without whose help I never would have finished this analysis, and Avi for harassing me at meetings, because if you don't drop a piece of steel once in a while it will start to think it's aluminium and get all mushy.

I mentioned my parents in the middle of this stream of consciousness, but they deserve the most thanks.

Contents

List of Figures

List of Tables

Chapter 1

Introduction

The Λ_B first appeared on the scene in 1991, when the UA1 experiment at CERN, pursuing a very aggressive analysis, announced its discovery [1]. Their measured of the production fraction times branching ratio

$$F(\Lambda_B) \times B(\Lambda_b \to J/\psi\Lambda) = (1.8 \pm 1.0) \times 10^{-3}$$

This is the fraction of b quarks which hadronize specifically to Λ_B, times the fraction of Λ_B's which decay specifically to $J/\psi\Lambda$. Subsequently, the CDF experiment obtained results using larger data samples which were in disagreement with this observation, setting limits on the branching ratio below UA1's measured value [4].

In 1996, both DELPHI [2] and ALEPH [3] measured the Λ_B mass in the decay channel $\Lambda_c\pi$. Each experiment found only four candidates. Finally, in 1997 the Λ_B appeared unambiguously in CDF's 110 pb^{-1} of data from Run I, with a mass of $5621 \pm 4(stat) \pm 3(syst)$MeV, and a production fraction times branching ratio of

$$F(\Lambda_B) \times B(\Lambda_b \to J/\psi\Lambda) = (3.7 \pm 1.7(stat) \pm 0.7(syst)) \times 10^{-4}[5]$$

Since the signal consisted of only 20 events, only the mass measurement was made; a lifetime measurement in this mode required more data.

This thesis presents a measurement of the lifetime of the b-baryon Λ_B in the fully reconstructed decay mode $\Lambda_B \to J/\psi\Lambda$, where $J/\psi\to \mu^+\mu^-$, $\Lambda \to p^+\pi^-$. Charge conjugation is implied throughout. Measuring the lifetime in this mode is particularly interesting, since no other measurement exists in a fully reconstructed mode.

More importantly, measurements so far are in disagreement with the theoretical predictions for $\tau(\Lambda_B)/\tau(B^0)$. The experimental world average is 0.797 ± 0.052, while theory predicts the value to be between 0.9 and 1.0.

Since the Λ_B is more massive than the mesons B^+ and B^0, it is produced only at the Tevatron. The Λ_B, like B_s^0, is not produced at any other currently operating machine.

The decay of Λ_B, with quark constituents bdu, to $J/\psi\Lambda$ is a color-suppressed decay which proceeds through an internal W decay. The Feynman diagram is shown in Figure 1.1. The decay is color-suppressed because the colors of the quarks from the virtual W must match the colors of the c quark and the remaining diquark system.

The decay mode $\Lambda_B \to J/\psi\Lambda$ is said to be fully reconstructed, because all of the final state particles leave tracks in the detector. Thus, the full momentum and the invariant mass may be determined. This is in contrast to the semileptonic decay modes which contain neutrinos. Neutrinos are neutral and interact very weakly; they leave no signal in the CDF detector.

A Feynman diagram for a semileptonic decay of Λ_B is shown in Figure 1.2. CDF has measured the Λ_B lifetime in Run I, in the semileptonic decay mode $\Lambda_B \to \Lambda_c l\bar{\nu}$, $l = e, \mu$ [37]. The semileptonic decay modes have larger branching ratios, and there

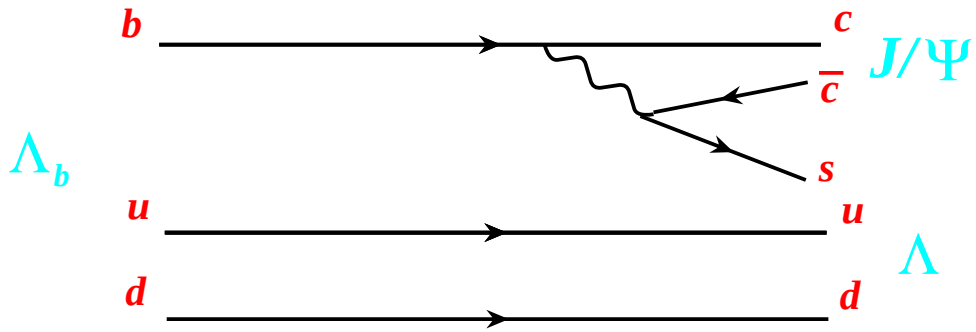

Figure 1.1: Feynman diagram for the decay $\Lambda_B \to J/\psi\Lambda$

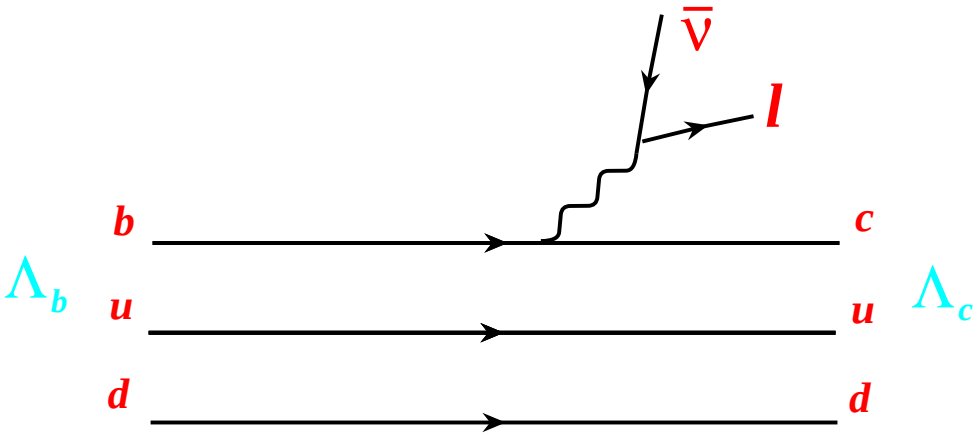

Figure 1.2: Feynman diagram for the decay $\Lambda_B \to \Lambda_c l\bar{\nu}$

are typically more reconstructed. Thus, the statistical errors on these measurements are usually smaller than in the exclusive modes. However, the exclusive modes possess distinct advantages. These stem mainly from the fact that we are able to detect all of the final state particles coming from the decay of the Λ_B. First, the invariant mass of Λ_B is fully reconstructed. This results in clearly defined signal and background regions. In the semileptonic decay, only the invariant mass Λ_c can be computed. Also, the sample is purer, due to the full reconstruction. Many measurements of the lifetime in semileptonic decay modes can only claim to be a measurement of the average b-baryon lifetime. For instance, another signature for b-baryons is the pairing of a Λ with a lepton. This is assumed to be mostly Λ_B but also can be the result of the decay of Ξ_B or Ω_B.

Finally, the momentum of the Λ_B is well measured. Knowing the momentum is important in order to convert measured decay length to proper decay time. For the semileptonic modes, it is unknown (due to the undetected neutrino) and must be estimated using Monte Carlo. Figure 1.3 shows measurements of $\tau(\Lambda_B)$ obtained by various experiments. All have been obtained using partially reconstructed modes.

The following is a brief summary of the analysis. We reconstruct Λ_B candidate events as described in Chapter 4. In addition to reconstructing $\Lambda_b \to J/\psi\Lambda$, we reconstruct $B^0 \to J/\psi K^0_s$. This serves as a control sample, since the decay is similar to that of Λ_B, but the B^0 has a well-known lifetime.

For each candidate event, we obtain the value of the proper decay time. This is determined as described in Chapter 5. We then perform an unbinned maximum likelihood fit to the distribution of proper decay length in data, to extract the value of $c\tau(B^0)$ and $c\tau(\Lambda_B)$.

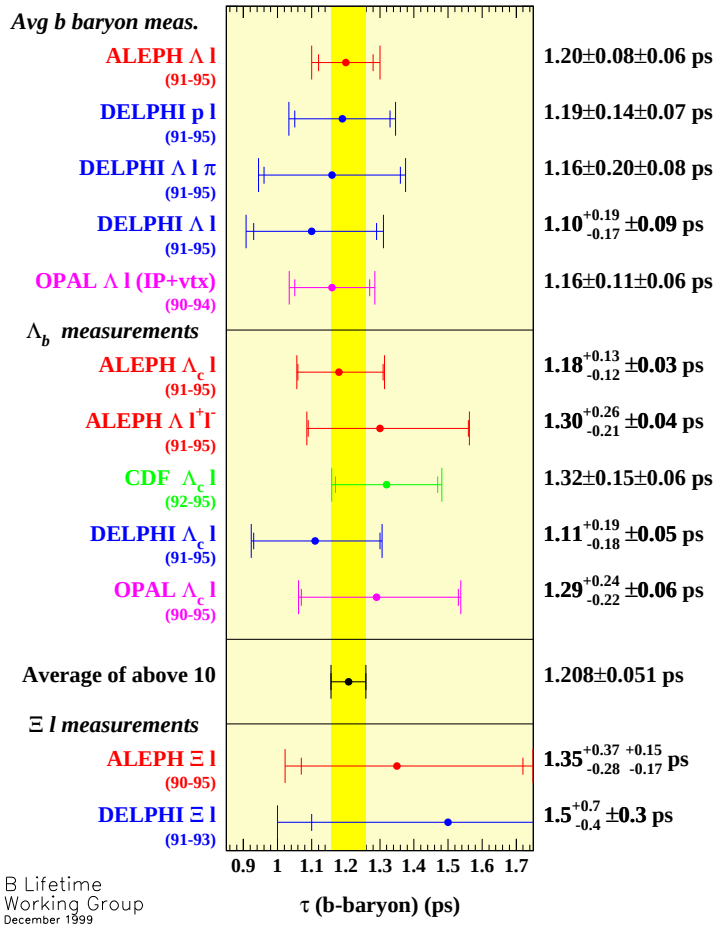

Figure 1.3: Measurements of the b-baryon and Λ_B lifetimes [16].

Chapter 2

Theoretical Overview

2.1 Spectator Model

In the Spectator Model of hadrons, a heavy quark in a hadron is bound to the lighter "spectator" quarks, but the weak decay of the heavy quark can be treated separately. In this approximation, all hadrons containing a given heavy quark have the same lifetime. The heavier the quark, the more valid the approximation. In the simple spectator model, we can write the decay width for a B meson

$$\Gamma(b) = \frac{9V_{cb}^2 G_F^2 M_b^5}{192\pi^3} \tag{2.1}$$

This is simply the formula for the muon decay width, with the CKM matrix element for quark coupling (b to c). We assume b decays mostly to c. The factor of nine is due to 9 possible virtual W decay channels: $\tau\nu_\tau$, $\mu\nu_\mu$, $e\nu_e$, and $u\bar{d}$, $c\bar{s}$, multiplied by a factor of three for color. With $M_b \approx 4.2$ GeV [56] and $V_{cb} \approx 0.045$ [7], this gives

$$\tau = \hbar/\Gamma = 1.2 \ \ \text{ps} \tag{2.2}$$

The lifetime of the B^+ has been measured to be approximately 1.65 ps. In addition, measurement confirms that the various b hadrons have different lifetimes.

Experiments have been precise enough for quite some time now to show that the spectator model is clearly insufficient. This is evident in lifetime ratios of charm hadrons, shown in Table 2.1 [8]. The only charm lifetime ratio near unity is that of the D_s^+/D^0. Since it is expected that the naive spectator approximation becomes more valid for heavier quark masses, it is not surprising the the B lifetime ratios are much closer to one.

Lifetime Ratio	Measurement
$\frac{\tau(D^+)}{\tau(D^0)}$	2.55 ± 0.034
$\frac{\tau(D_s^+)}{\tau(D^0)}$	1.125 ± 0.042 PDG '98 $1.211 \pm 0.0.017$ E791,CLEO,FOCUS
$\frac{\tau(\Lambda_c^+)}{\tau(D^0)}$	0.489 ± 0.008
$\frac{\tau(\Xi_c^+)}{\tau(\Lambda_c^+)}$	1.75 ± 0.36 PDG '98
$\frac{\tau(\Xi_c^0)}{\tau(\Xi_c^+)}$	3.57 ± 0.91 PDG '98
$\frac{\tau(\Xi_c^+)}{\tau(\Omega_c)}$	3.9 ± 1.7 PDG '98
$\frac{\tau B^-}{\tau(B^0)}$	1.074 ± 0.014 [16]
$\frac{\tau B_s}{\tau(B^0)}$	0.949 ± 0.038 [16]
$\frac{\tau(\Lambda_B)}{\tau(B^0)}$	0.792 ± 0.052 [16]

Table 2.1: Lifetime ratios in the charm [8] and bottom sectors.

2.2 The Origin of Lifetime Differences

The main sources of the differences in lifetimes for a given heavy quark are Pauli Interference (PI), Weak Annihilation (WA) (for mesons), and Weak Exchange (WE) (for baryons) [8].

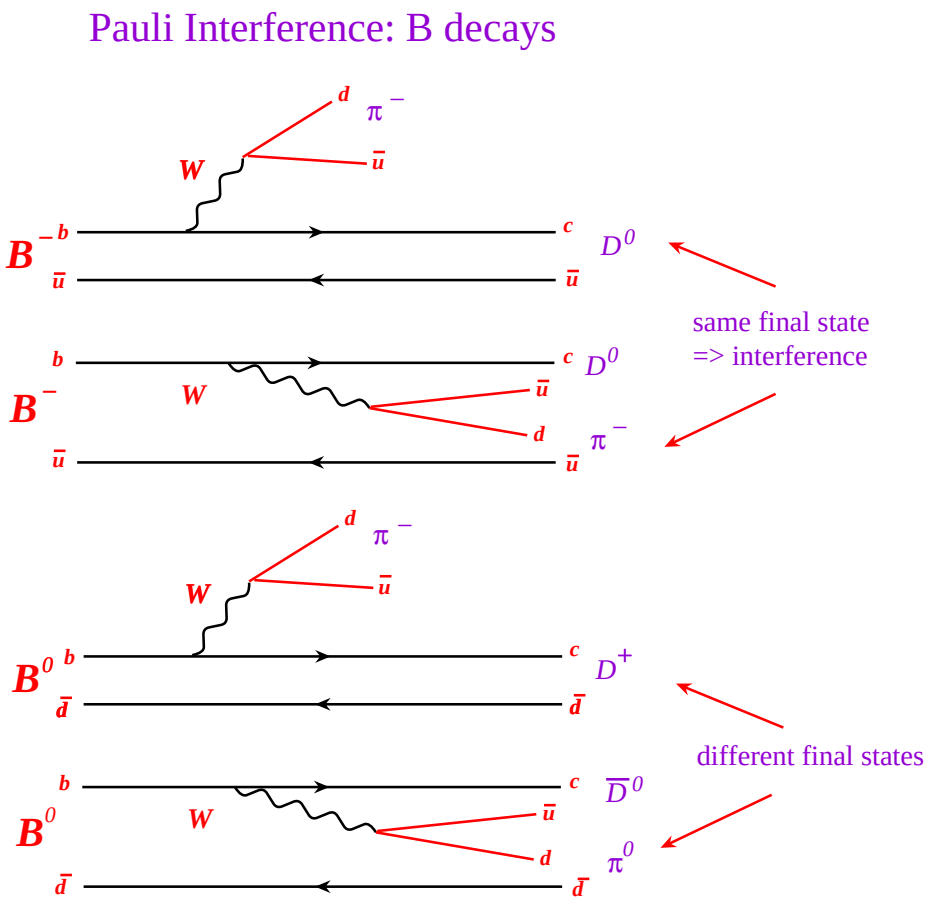

Figure 2.1: An illustration of Pauli Interference in B decays.

A diagram illustrating Pauli Interference(PI) in $B^- \to D^0\pi^-$ is shown in Figure 2.1. There are two mechanisms for the decay: internal and external emission

of a W. The two final states are indistinguishable, resulting in quantum mechanical destructive interference in the calculation of the decay rate. This is not the case for the analogous diagrams in $B^0 \rightarrow D\pi$ since there are two distinguishable final states: $D^+\pi^-$ and $\bar{D}^0\pi^0$. This results in the B^- having a longer lifetime than the B^0. Pauli Interference is also believed to be the main source of the D^+ - D^0 lifetime difference [10].

Weak annihilation (WA), the second source of lifetime differences, is shown for the case of B^- in Figure 2.2. In WA, the constituent quarks of the meson annihilate to form a virtual W. In the case of B^-, with constituent quarks $b\bar{u}$, the amplitude is proportional to V_{ub} so the effect is expected to be small. The effect is larger in the charm system, where it contributes to decays of D^+, but not D^0. This is because the D^0 constituent quarks are $c\bar{u}$, and the weak interaction does not couple c to u. There are no flavor-changing neutral currents.

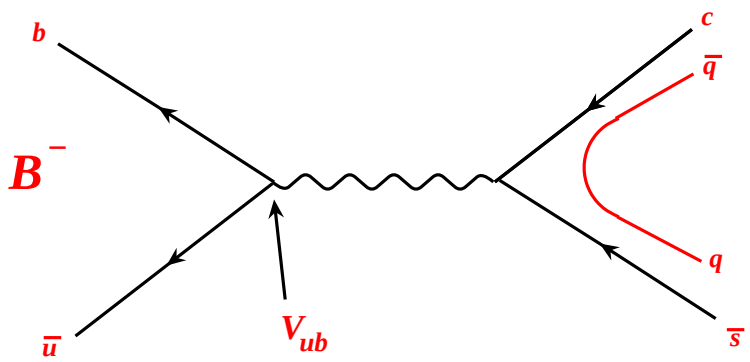

Figure 2.2: An illustration of Weak Annihilation in B^- decays.

Weak Exchange(WE), or Weak Interference, is shown for the B^0 and Λ_B in Figure 2.3. This process is helicity suppressed in mesons, but is not in baryons, and

is thus expected to be the main explanation for a shorter Λ_B lifetime [14]. Helicity suppression of W exchange is present in pseudoscalar mesons for the same reason that the decay $\pi \to e\nu$ is suppressed. The helicity assignments of $V - A$ interaction are left-handed for particles and right handed for antiparticles. For a weak exchange in a B^0 we have $B^0 \to c\bar{u}$. A cartoon illustrating the desired helicity configuration for the decay of a spin-0 particle is shown in Figure 2.4. This conflicts with the configuration where the W couples to a left-handed c-quark and a right-handed $\bar{u}$ quark, since both particles must be left-handed for the spins to add up correctly.

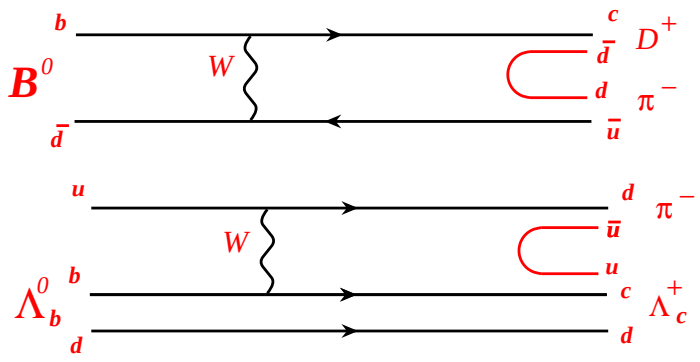

Figure 2.3: An illustration of Weak Interference in B^0 and Λ_B decays.

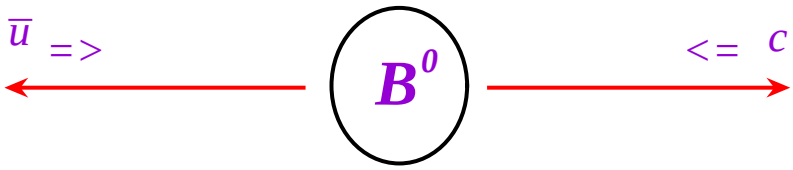

Figure 2.4: Cartoon of $B^0 \to c\bar{u}$. In this figure the direction of travel is designated by $\to$, and the spin direction by $\Rightarrow$. In the configuration shown, the spins of the outgoing quarks add up to zero, which is the spin of the B^0. This results in both the particle and the antiparticle being left-handed, which is a disfavored by the W coupling.

2.3 Theory Predictions

Beyond the simple spectator model, the weak decay width for a heavy flavor hadron H_Q into an inclusive final state f can be expressed in an operator product expansion (OPE) [8] .

$$\Gamma(H_Q \to f) = \frac{G_F^2 m_Q^5}{192\pi^3} |V_{CKM}|^2 \left[c_3^{(f)} \left\langle H_Q \left| \bar{Q}Q \right| H_Q \right\rangle + c_5^{(f)} \frac{\mu_G^2(H_Q)}{m_Q^2} + \sum_i c_{6,i}^{(f)} \frac{\left\langle H_Q \left| (\bar{Q}\Gamma_i q)(\bar{q}\Gamma_i Q) \right| H_Q \right\rangle}{m_Q^3} + O(1/M_Q^4) \right] \tag{2.3}$$

where

$$\mu_G^2(H_q) \equiv \left\langle H_Q | \bar{Q} \frac{i}{2} \sigma \cdot GQ | H_Q \right\rangle . \tag{2.4}$$

and q is the light-quark field.

The expansion separates perturbative short-distances physics ($1/m_q \ll 1/\Lambda_{QCD}$) from the long distance, nonperturbative physics. The coefficients c_i^f are calculable with perturbation theory. The expectation values of the operators are calculated by other nonperturbative means, such as QCD sum rules, lattice studies, or quark models [8].

The operator in the first term can be written as:

$$\left\langle H_Q | \bar{Q}Q | H_Q \right\rangle = 1 + \mathcal{O}(1/m_q^2) \tag{2.5}$$

For $m_q \to \infty$, we are left with the spectator model. The $\mathcal{O}(1/m^2)$ term is proportional to the kinetic energy of the b in the hadron. The difference in kinetic energy for mesons and baryons can be written in terms of the masses of the B^0, D^0, Λ_B, and Λ_c [10].

The second term is also $\mathcal{O}(1/m^2)$. The operator in the second term is referred to as the chromomagnetic operator, and takes into account spin interactions. For this and the first term, there are no light-quark fields. Any lifetime difference among mesons are generated by the third term, which does include fields for the light quarks. This term includes the effects discussed in the previous section. (PI, WA, WE)

The second term can however generate differences between meson and baryon lifetimes for a given heavy flavor:

For *mesons* [10]

$$\left\langle P_Q|\bar{Q}i\sigma\cdot GQ|P_Q\right\rangle_{norm} \simeq 3/2(M^2_{V_Q} - M^2_{P_Q}) \tag{2.6}$$

where P_Q and V_Q denote the pseudoscalar and vector mesons. Then, for the B^0

$$\left\langle \mu^2_G(H_Q)\right\rangle_B \simeq \frac{3}{4}(M^2_{B^*} - M^2_{B^0}) = 0.37 \ \ \text{GeV}^2 \tag{2.7}$$

For *baryons* Λ_Q and Ξ_Q [10]

$$\langle \Lambda_Q|Qi\sigma\cdot GQ|\Lambda_Q\rangle \simeq 0 \simeq \langle \Xi_Q|Qi\sigma\cdot GQ|\Xi_Q\rangle \tag{2.8}$$

since the light diquark system carries no spin.

Thus, meson width differences for a given heavy flavor are of $\mathcal{O}(1/m^3_q)$, while meson-baryon width differences are of $\mathcal{O}(1/m^2_q)$ [10]. For mesons, the four-quark operator in the $1/m^3_q$ term can be expressed in terms of the decay constant, f_B. For baryons this is not the case. The b-baryon calculation is made even more complex by the fact that PI, WA, and WE may all have non-negligible effects, whereas for b-mesons PI dominates.

The Operator Product Expansion has been used to predict ratios of charm lifetimes. These are shown in Table 2.2.

Lifetime Ratio	Theory	Prediction	Measurement
$\frac{\tau(D^+)}{\tau(D^0)}$	PI dominant	~ 2	2.55 ± 0.034
$\frac{\tau(D_s^+)}{\tau(D^0)}$	without WA	$1.0 - 1.07$	1.125 ± 0.042 PDG '98
	with WA	$0.9 - 1.3$	$1.211 \pm 0.0.017$
	QCD sum rules	1.08 ± 0.04	E791,CLEO,FOCUS
$\frac{\tau(\Lambda_c^+)}{\tau(D^0)}$	quark model matrix elements	~ 0.5	0.489 ± 0.008
$\frac{\tau(\Xi_c^+)}{\tau(\Lambda_c^+)}$	"	~ 1.3	1.75 ± 0.36 PDG '98
$\frac{\tau(\Xi_c^0)}{\tau(\Xi_c^+)}$	"	~ 2.8	3.57 ± 0.91 PDG '98
$\frac{\tau(\Xi_c^+)}{\tau(\Omega_c)}$	"	~ 4	3.9 ± 1.7 PDG '98

Table 2.2: Lifetime ratio predictions in the charm sector [8]. The Theory column indicates the expected dominant mechanism, which mechanisms have been included, or the particular treatment used for the calculation. The Prediction column indicates the value of the theory prediction. The Measurement column shows results from various experiments.

Since the b quark is heavier, the predicted lifetime differences for B mesons are much smaller, with a hierarchy of:

$$\tau(\Lambda_B) < \tau(B^0) \sim \tau(B_s) < \tau(B^+) \tag{2.9}$$

Current world-average experimental values and theoretical predictions for b hadrons are shown in Figure 2.5. Given that experimentally $\langle \tau(\Lambda_B)/\tau(B^0) \rangle = 0.783 \pm 0.034$, while theory predicts 0.9-1.0, a discrepancy is evident.

The theoretical result for $\tau(\Lambda_B)/\tau(B^0)$ is understood as a slight enhancement in the decay rate due to weak exchange, which is partially offset by Pauli Interference

[14]. Rosner has published a new evaluation of this enhancement. His result [14] is expressed in terms of the hyperfine splitting $M(\Sigma_B^*) - M(\Sigma_B)$, which has been measured at the DELPHI Collaboration. This relies on the assumption that the wave functions are similar in all baryons with one b quark and two nonstrange quarks. Unfortunately, the result explains only 13% of the needed enhancement in decay rate.

Neubert and Sachrajda have also reanalyzed the problem. They conclude that the current models used to evaluate the matrix elements in the OPE cannot accomodate the low experimental value of $\tau(\Lambda_B)/\tau(B^0)$. The value of theoretical prediction for the ratio is driven by the baryonic parameter r, the ratio of the squares of the wave functions determining the probability to find a light quark at the location of the b quark inside of the Λ_B and the B^0.

$$r = \frac{|\psi^{bq}_{\Lambda_B}(0)|^2}{|\psi^{B_q}_{b\bar{q}}(0)|^2} \tag{2.10}$$

This parameter is used in the calculation of the 4-quark operator matrix element, in the third term of the OPE. Until a reliable field theoretical calculation for r becomes available, the discrepancy between theory and experiment will most likely remain unresolved [15].

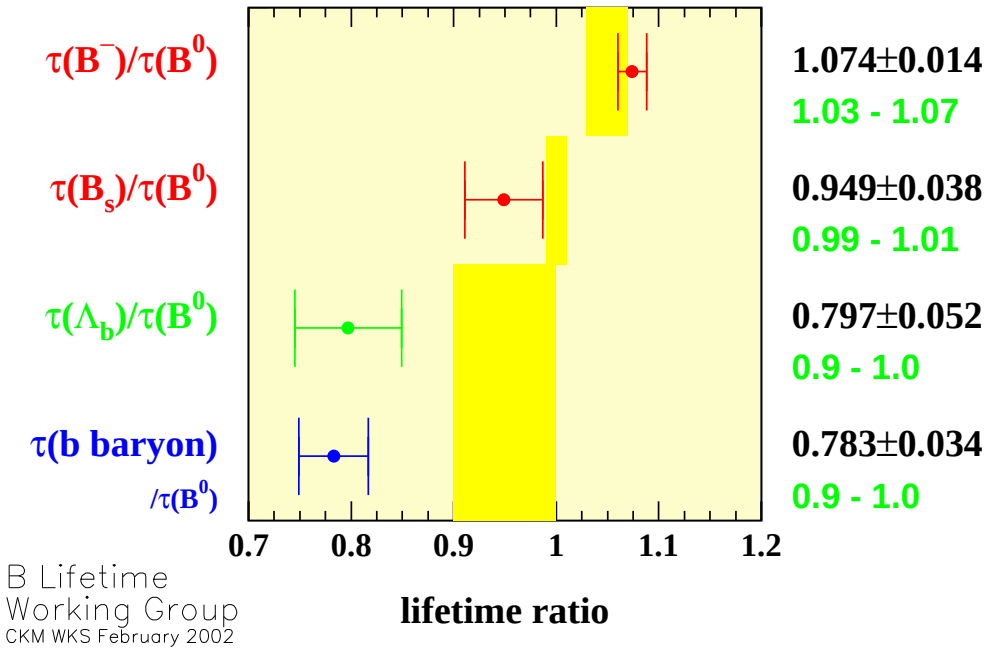

Figure 2.5: Theory predictions (shaded band) and world averages (points with error bars) for B lifetime ratios [16].

Chapter 3

The CDF II Detector

At Fermilab, the world's highest energy accelerator is used to accelerate and collide beams of protons and anti-protons. The collisions occur at two points in an underground ring, which has a circumference of $\approx$ 4-miles (2π km). Situated around these collision points are two experiments: CDF - The Collider Detector at Fermilab, and D0. This analysis was performed using data collected by the CDF experiment.

Between 1997 and 2001, both the accelerator complex and collider detectors underwent major upgrades: the goal being increased instantaneous luminosity, with data samples of eventually 2 fb^{-1} of integrated luminosity or more. The upgraded accelerator has a shorter time between beam crossings than its predecessor: 396 ns in the current 36-bunch mode compared to 3.5 μs in the old 6-bunch mode. The upgrade also includes plans for 132 ns operation.

The new configuration required detector upgrades at CDF to ensure a maximum response time shorter than the time between beam crossings. In the following pages, we describe how the proton and anti-proton beams are produced, accelerated to their

final center of mass energy of 1.96 TeV, and collided. We then describe the detector components used to identify and measure properties of the produced particles.

3.1 $p\bar{p}$ Production and Acceleration

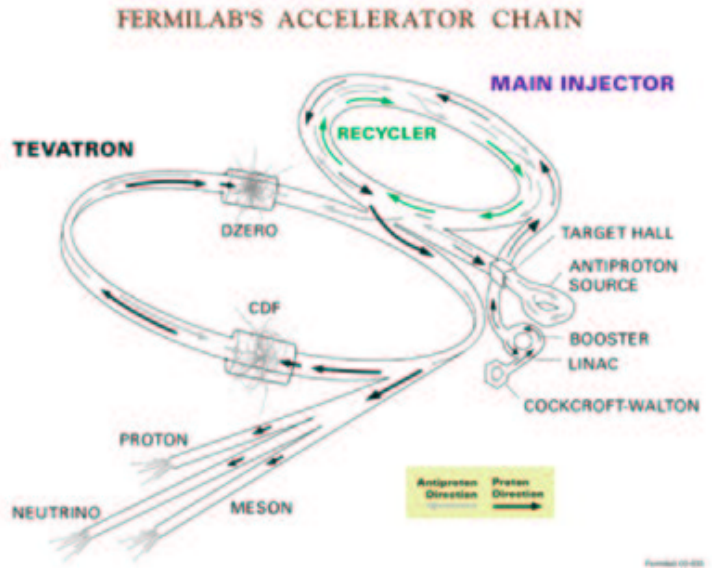

Figure 3.1: Diagram of the Fermilab $p\bar{p}$ accelerators

At the B0 and D0 interaction regions of the Tevatron collider, a beam of 980 GeV protons collides head-on with a beam of 980 GeV anti-protons, resulting in the hard scattering events studied by the CDF and D0 experiments. Producing the proton and anti-proton beams and accelerating them to high energies requires the many specialized stages of Fermilab's accelerator chain, shown in Figure 3.1.

The first stage is a Cockroft-Walton accelerator, which accelerates H^- ions to 750 keV. Next, a linear accelerator (Linac) takes the H^- ions from 750 keV kinetic energy to 400 MeV. The Linac has two parts: a 116 MeV drift-tube (Alvarez) linac operating

at 201.25 MHz and a 400 MeV side-coupled cavity linac operating at 805 MHz [17]. Because of the Linac geometry, the accelerated ions become grouped into bunches.

Next, the 400 MeV H^- ions are injected into the Booster, a 74.5m-diameter circular synchrotron. At injection, a carbon foil strips the electrons from the H^- ions, leaving protons. Successive turns of ions are injected into the same orbit as the circulating protons. The Booster accelerates the protons from 400 MeV to 8 GeV. This is accomplished by a series of electromagnetic kicks applied by RF cavities: about 500 kV per turn.

Next, the protons are extracted to the Main Injector [19], which operates at 53 MHz. They are accelerated to 150 GeV for injection into the Tevatron, or to 120 GeV for anti-proton production. The Main Injector, a new element of the Run II accelerator complex, is capable of larger proton currents than its predecessor, the Main Ring, enabling a higher rate of anti-proton production.

To produce anti-protons, 120 GeV protons from the Main Injector are directed onto a nickel target, creating a multi-particle spray that contains on average 20 anti-protons per million protons, with a mean kinetic energy of 8 GeV. The anti-protons are then focused by a lithium lens and separated from other particle species by a pulsed magnet.

Before the anti-protons can be used in the narrow beams needed in the collider, they must be cooled. New batches of anti-protons are initially cooled in the Debuncher synchrotron, then collected and further cooled, using stochastic cooling [18], in the 8 GeV Accumulator synchrotron. Over a period of 10 to 20 hours, a stack of anti-protons is built up, in preparation for a new store in the Tevatron-the final stage of Fermilab's accelerator chain.

At the start of a store, about once per day, 36 bunches of about $3{\times}10^{11}$ protons and 36 bunches of roughly 3×10^{10} anti-protons are accelerated to 150 GeV by the Main Injector, transferred to the Tevatron, and accelerated to 980 GeV.

In 36-bunch mode, the time between beam crossings is 396 ns, compared with 3.5 μs in the Run I 6-bunch mode. The Luminosity can be expressed as:

$$\mathcal{L} = \frac{fBN_pN_{\bar{p}}}{2\pi({\sigma_p}^2 + \sigma_{\bar{p}}^2)} F\left(\frac{\sigma_l}{\beta^*}\right) \tag{3.1}$$

Here, f is the revolution frequency, B is the number of bunches, $N_{p/\bar{p}}$ are the number of protons/anti-protons per bunch, and $\sigma_{p/\bar{p}}$ are the rms beam sizes at the interaction point. F is a form factor which depends on the ratio of σ_l, the bunch length, to β^*, the beta function, at the interaction point. The beta function is a measure of the beam width, and is proportional to the beam's x and y extent in phase space. Antiproton availability is the most limiting factor for attaining high luminosities [19].

Table 3.1 shows a comparison of Run I and Run II accelerator parameters. Figure 3.2 shows the initial luminosities for stores used in this analysis.

Run	Ib (6×6)	IIa (36×36)
protons/bunch	2.3×10^{11}	2.7×10^{11}
anti-protons/bunch	5.5×10^{10}	3.0×10^{10}
total anti-protons	3.3×10^{11}	1.1×10^{12}
proton emittance(mm-mrad)	23π	20π
anti-proton emittance(mm-mrad)	13π	15π
β^* (cm)	35	35
anti-proton bunches	6	36
bunch length (m)	0.6	0.37
bunch spacing (ns)	3500	396
interactions/crossing	2.5	2.3

Table 3.1: Parameters describing the accelerator configuration in Run I and Run II. The Run Ib column shows typical operating parameters during Run Ib. The Run IIa column shows projections for Run IIa in 36×36 operation [19].

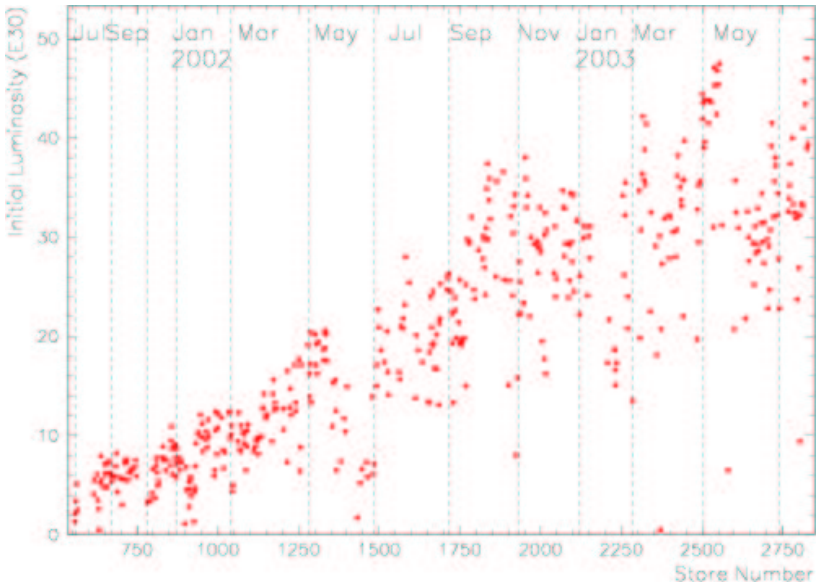

Figure 3.2: The initial instantaneous luminosity, in units of $\mathrm{cm}^{-2}\mathrm{s}^{-1}$, of $p\bar{p}$ stores during the period from June 2002 to May 2003.

3.2 CDF II: The Collider Detector at Fermilab for Run II

3.2.1 Detector Overview

Before describing the detector, we establish the CDF coordinate system. Protons travel from west to east through CDF, and anti-protons in the opposite direction. The positive z-axis is defined to be along the direction traveled by the protons. CDF is approximately cylindrically symmetric, so the origin is placed at the center of the cylinder along z, at $r = 0$. The y axis is in the direction parallel to gravity, with positive y being "up". This also defines x, since the coordinate system is right handed. The polar and azimuthal angles are θ and ϕ.

At the most basic level, the CDF detector can be separated into 4 parts: Tracking, Calorimetry, Muon identification, and Particle Identification. An elevation view of the CDF detector is shown in Figure 3.3

CDF has both electromagnetic and hadronic calorimetry, segmented into towers in η, the pseudorapidity, and ϕ. η is defined as:

$$\eta \equiv -\ln \tan(\theta/2) \tag{3.2}$$

Towers in the central calorimeter span 15° in azimuth and 0.11 in pseudorapidity. The coverage is $0 < |\eta| < 1.3$. For Run II, there is a new Plug Calorimeter, with variable tower size, which extends coverage out to $|\eta| = 3.6$. This analysis uses only Tracking and Muon Identification. For a more detailed description of the calorimetry, we refer the reader to the Run I description of the CDF detector [20] and the Run II Technical Design Report [21], which discusses the Plug Upgrade Calorimeter.

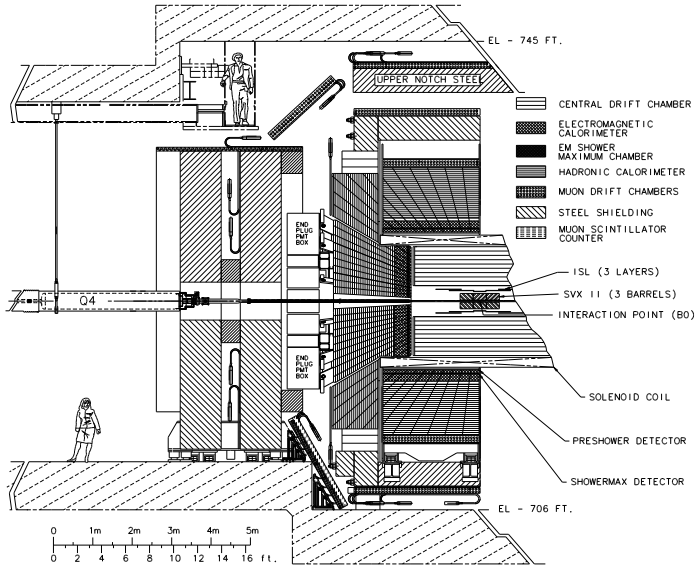

Figure 3.3: Elevation view of the CDF II detector.

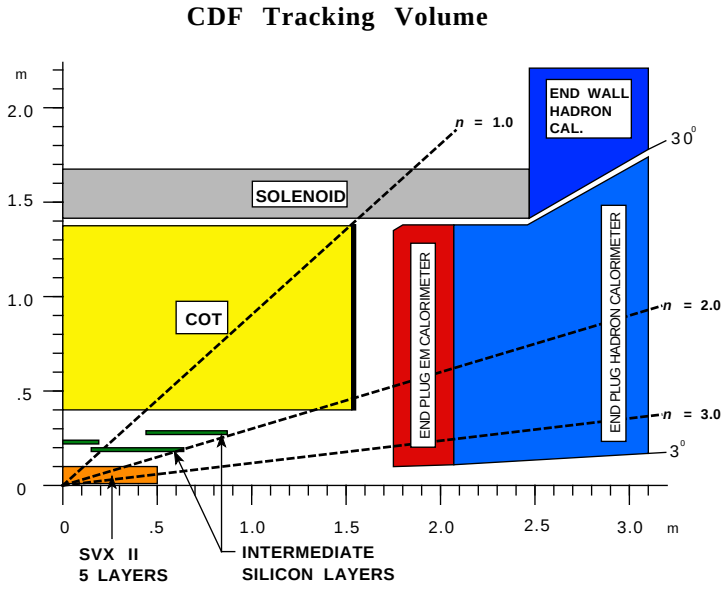

Figure 3.4: One quadrant of the CDF Tracking Volume

The tracking system is cylindrically symmetric. One quarter is shown in Figure 3.4. The parts of the tracking furthest from the interaction point are the Superconducting Solenoid of 1.41 T, and the Central Outer Tracker (COT), a jet-cell wire chamber. These two devices function together as a magnetic spectrometer, which measures the momenta of charged particles.

Further inward, we encounter the silicon detector: the main purpose is precision vertex information. Its outermost piece is the ISL, or Intermediate Silicon Layers, with coverage for large pseudorapidities, up to $|\eta| = 2$. Closer to the interaction point, is the five layer Silicon Vertex Detector named SVX II. An additional silicon device called Layer 00, mounted on the beampipe, is the innermost detector. In this analysis, we use only SVX II.

Outside both the tracking volume and the calorimeters are the Muon identification systems. There are 3 pieces to this detector: the CMU (central muon system), CMP (central muon upgrade detector), and the CMX (central muon extension) for higher pseudorapidity coverage of $0.6 < |\eta| < 1.0$. Any charged particle which survives passage through the calorimeter and leaves a signal in one of these detectors (matched to a track in the COT) is considered a muon candidate.

Particle Identification is done both in the COT, using dE/dx, and in the Time Of Flight (TOF) [22]. This detector is situated between the solenoid and COT, and measures the time between a beam crossing and a particle incident upon the detector itself. We haven't made use of it in this particular analysis because we could not afford the loss in efficiency.

3.2.2 The CDF Trigger System

An important component for a detector at a hadron collider is the trigger system. We cannot record all events that occur in the $p\bar{p}$ collisions. The size of a typical event is 250 kB. At the 2.5 MHz beam crossing rate, the system would have to be capable of recording 625 GB/sec. This is assuming that there is an interaction every beam crossing, which is not unreasonable, given that we expect an average of 2.3 interactions per crossing (See Table 3.1.)

Much of this data would never be analyzed, since most of the products of $p\bar{p}$ collisions are rather ordinary events. We are interested in events containing particles with large transverse energy. This reflects hard scattering of quarks in the protons and anti-protons. The uninteresting inelastic events, called "minimum bias", occur 10 orders of magnitude more frequently than $t\bar{t}$ events, and 4 orders of magnitude more often than events with b's. Currently, the maximum event rate to disk is $\approx$ 70 Hz. If events were selected randomly, we would have no chance of acquiring interesting data samples large enough to make precise measurements.

The complex system of digital electronics called the trigger allows the experiment to decide, in a very short amount of time, whether an event is interesting enough to record. It is of the utmost importance that the decision is fast, so that collisions are not missed while the trigger is thinking about its decision

CDF uses a three level trigger. At every beam crossing, data from all detectors is digitized, excepting the silicon, which samples and holds only. This data is made available to the Level 1 trigger, which can identify rudimentary physics signatures. Since Level 1 takes longer than one beam crossing to make its decision, data from

detector subsystems are provided to it in a 5 μs deep pipeline. Level 1 can then perform such functions as the matching of muon "stubs" and calorimeter energy clusters to charged particle tracks in the drift chamber. Charged particle tracking on this timescale is accomplished by the use of custom hardware called the eXtremely Fast Tracker (XFT) [23]. The XFT performs a coarse measurement of the tracks' transverse momenta using what is essentially a fast lookup table. It is efficient for transverse momenta above 1.5 GeV.

An event will pass Level 1, to be stored in one of four data buffers, if an interesting signature is found. Since this analysis begins with a sample of $J/\psi \to \mu^+\mu^-$, we are most concerned with muon stubs matched to tracks in the drift chamber. This is one of a handful of physics signatures which lead to Level 1 accepting an event. Level 1 reduces the event rate from 2.5 MHz to 25 kHz.

If the event does pass Level 1, it is passed to the Level 2 trigger. The information from the silicon is then digitized. Fast silicon tracking in $r - \phi$ (no z information) is performed by the Silicon Vertex Trigger (SVT) [24]. Calorimeter clustering is also done here. The Level 2 decision is made in a single computer, based on higher level information that can be derived from the data available. Some examples of this information are the transverse mass of two muons, and the impact parameter of a track with hits in the SVXII (found by the SVT). Level 2 reduces the event rate to $\approx$ 250 Hz, and requires $\approx 30\mu$s.

The next stage is the software of Level 3, on $\approx$ 200 standard pc's running Linux. Full 3d tracking is performed with parallel event processing. On one CPU, one event is processed in approximately 1 second. More complex quantities, such as dimuon invariant mass, are calculated here. Since the tracking here is more precise than at

Level 1, quantities on which requirements were made at Level 2 may be subjected to more stringent requirements. About 150 separate trigger paths are pursued. If an event passes Level 3, it is written to disk, with a maximum event rate of approximately 70 Hz.

3.2.3 Tracking System

Tracks

We reconstruct the trajectories of charged particles, called tracks, in the COT and SVXII. The tracks bend to form helices in the 1.41T magnetic field. Their transverse momenta can be related to half-curvature C by $p_T = (B/2cC)$, where c is the speed of light and B the magnitude of the magnetic field. The half-curvature is generally referred to as curvature. The tracking uses 5 parameters to describe the helices: impact parameter (d_0), curvature(C), ϕ_0, z_0 and $\lambda = cot\theta$. These are illustrated in Figure 3.5.

The helix is a circle in the xy plane, whose curvature is related inversely to transverse momentum, as described above. The sign of the curvature is the charge of the particle. The circle in the xy plane has a well-defined point of closest approach to the origin, $\vec{P}$. ϕ_0 is the angle between the x axis and a line tangent to the track at $\vec{P}$, and the signed impact parameter d_0 is the y-intercept of the track, after rotating the coordinate system so that $\phi_0 = 0$. z_0 is the position of the track along the z-axis at $\vec{P}$, and λ is defined as $cot\theta = p_z/p_T$. The axial parameters, which provide information in the xy plane only, are C, d_0 and ϕ_0. λ and z_0 are called stereo parameters, since they provide z information.

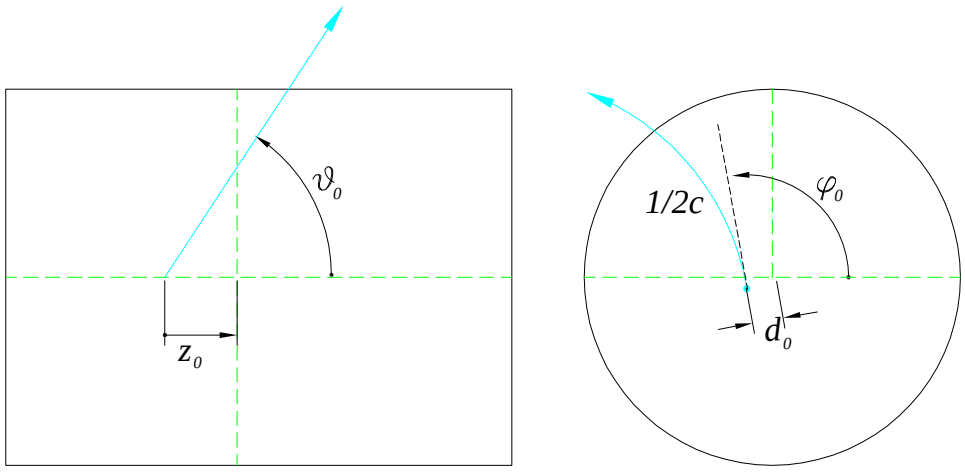

Figure 3.5: An illustration of the tracking parameters: the figure on the left shows a charged track in the $r-z$ view of the tracking volume. The figure on the right shows an $r-\phi$ view of the track. d_0 is the track's impact parameter, or point of closest approach to the origin. c is the curvature.

COT

The COT, or Central Outer Tracker, is the main tracking chamber in CDF. It is a cylindrical drift chamber segmented into 8 concentric superlayers. The active volume extends 122 in. in z, and from 17.1 to 52.1 in. in radius. Each superlayer is sectioned in ϕ into separate cells. A cell is defined as one sense plane (active and read-out) with two adjacent field planes, which are grounded. A diagram of a section of the endplate, with slots for the field and sense planes, is shown in Figure 3.6

Figure 3.7 shows a diagram of 3 cells in the $r-\phi$ plane. The rows of small circles represent high voltage wireplanes. There are a total of 29 wires in each cell, 12 of which are read out. These are called sense wires. The remaining wires are needed to shape the electric field, adjusting for the taper of the cell with decreasing radius. The lines adjacent to the sense planes represent the grounded field planes.

The sense plane wires are composed of 40 μm gold-plated tungsten wire. The main

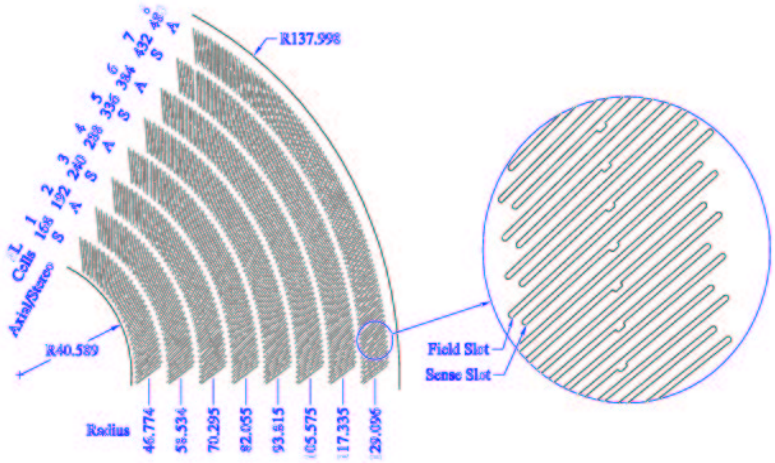

Figure 3.6: A section of the COT endplate, showing the cell counts in superlayers 1-8. The radii at the center of each superlayer are shown in cm. The endplate has inner and outer radii of 40.589 cm and 137.998 cm.

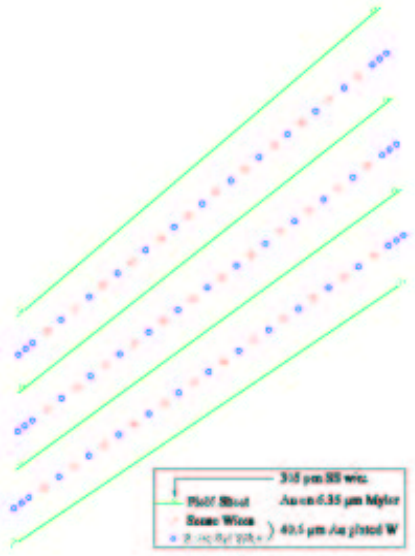

Figure 3.7: An transverse view of three cells in the COT. The continuous lines represent field sheets, which are grounded, and approximately 11.8 cm wide. The arrays of circles represent a high-voltage wireplanes. The lighter-shaded circles are the sense wires, which are read out. The darker shaded circles are the field wires.

body of the field sheets is 0.25 mil gold-coated mylar. The mylar is stretched and supported by two 12 mil stainless steel wires, which are epoxied in a parabolic shape along the each side of the field sheet. In axial superlayers, they are approximately parallel to the z-axis. The field sheets are much closer to a true grounded plane than arrays of wires, which have often been used in wire chambers, including the predecessor to the COT. Use of the field sheets results in a smaller total radiation length, and allows the COT to operate at much higher drift field than with an array of wires. This is an important factor in maximum drift time. In addition to this, the total endplate load is less, because a single field plane requires less tension than an array of field wires.

The eight superlayers of the COT alternate between stereo and axial, beginning with superlayer 1, which is a stereo layer. In an axial layer, the wires and fieldplanes are parallel to the z axis, and thus provide only $r - \phi$ information. In stereo layers, a given wireplane or field sheet which starts at a slot in one endplate does not end at the mirror-image slot in the other. Instead, it is offset by 6 cells. This generates a stereo angle of $\pm 2^\circ$, depending upon the direction.

The COT is filled with Argon/Ethane(50:50). When a charged particle passes through, the gas is ionized. Electrons drift towards the sense wires, resulting in an avalanche at the wire surface, which provides a gain of $\approx 10^4$. Due to the magnetic field, the electrons drift with a Lorentz angle of $\approx 35^\circ$. It is for this reason that the cells are tilted with respect to the radial direction. An illustration of the electron drift using the `GARFIELD` simulation is shown in Figure 3.8 [25]. The voltage on the wire planes is set in order to insure a maximum drift time which is less than the time between beam crossings, which is currently 396 ns.

Signals on the sense wires are processed by the ASDQ (Amplifier-Shaper-Discriminator with Charge Encoding), which provides input protection, amplification, pulse shaping, baseline restoration, discrimination, and charge measurement [26]. This charge measurement is encoded in the width of the discriminator output pulse, and is used in the measurement of dE/dx, for particle ID. The pulse is sent through $\approx$ 35 ft. of micro-coaxial cable, through repeater cards, and finally to the TDC's, which reside in the collision hall. Hit times are then processed by pattern recognition and fitting algorithms to form helices. These algorithms are collectively referred to as "tracking". Figure 3.9 shows the COT hit resolution vs. drift distance, measured by an online monitoring program, `STAGE0`. The single hit resolution is about 150 μm in the center of the cell.

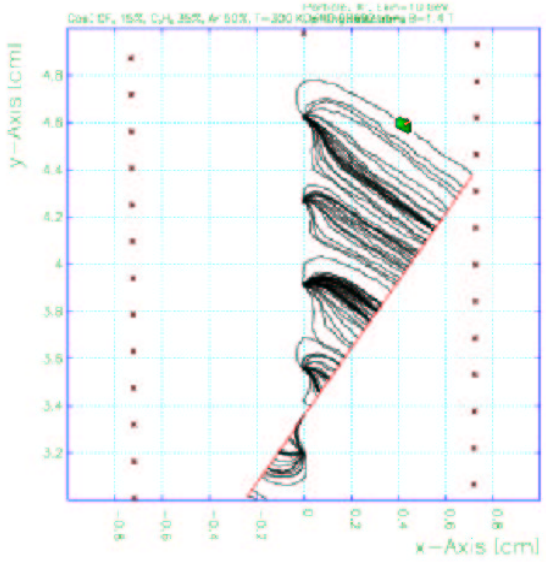

Figure 3.8: The drift of electrons towards the sense wires, as predicted by the `GARFIELD` Simulation [25]. The straight line represents a charged particle passing through the detector. Along the track, ionizations occur, and the liberated electrons, or clusters of electrons, drift towards the sense wires. The direction of drift is determined by the electric field (due to the sense wires, potential wires, and field sheets) and the magnetic field, which is required for the COT to function as a spectrometer.

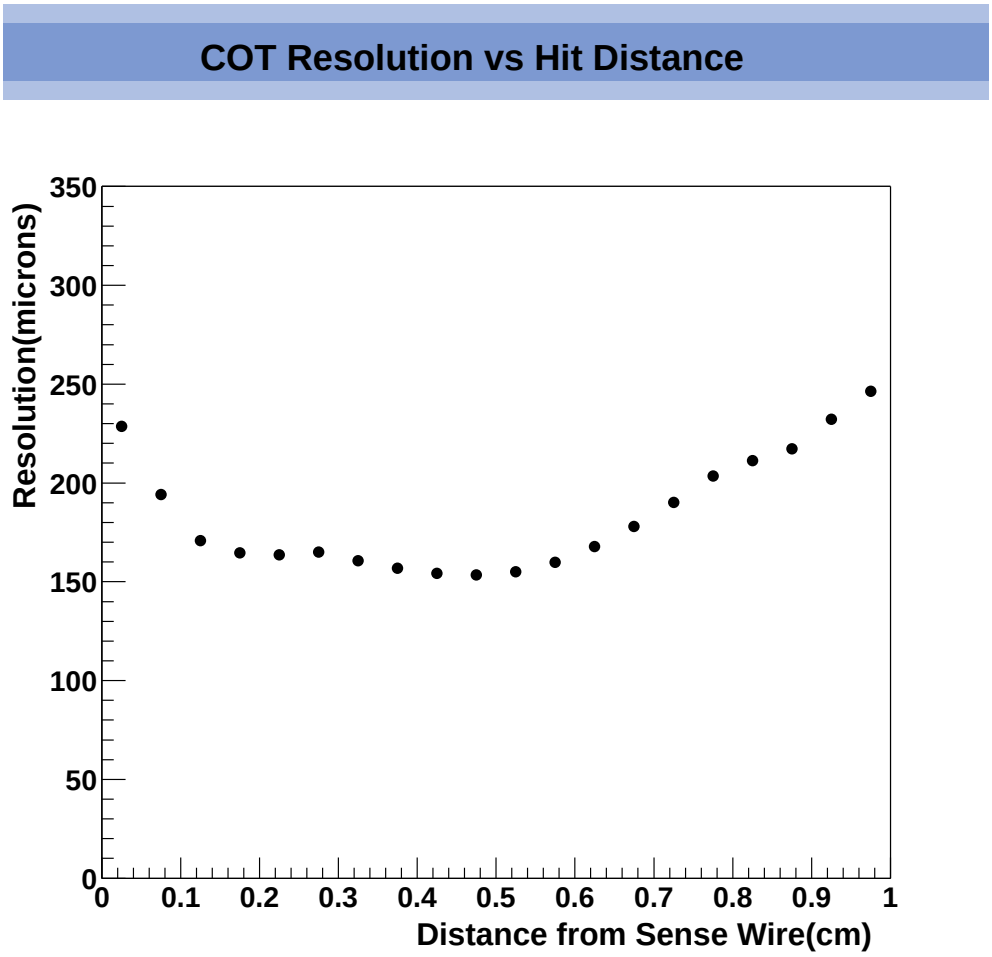

Figure 3.9: Single hit resolution vs. drift distance measured in data. The measurements are an average over all superlayers.

Silicon Vertex Detector

The CDF Silicon Vertex Detector has three separate subdetectors: ISL (intermediate silicon layers) from 20 to 28 cm in radius, the SVXII, from 2.45 to 10.6 cm, and Layer 00, which is mounted on the beampipe, with sensors at 1.35 and 1.62 cm. A diagram of the $r - z$ coverage of the detectors is shown in Figure 3.10.

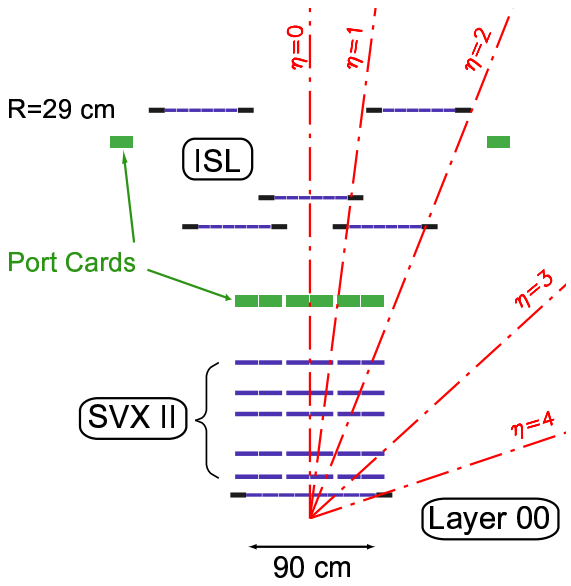

Figure 3.10: Placement in r and z of the three silicon detectors.

The SVXII is composed of wire bonded pairs of double-sided silicon sensors. Each side provides information in either ϕ or z. On the ϕ measurement side, the sensors have 65 μm pitch strips of p-type material (material which is doped with positive charge) implanted near the surface of lightly doped n-type material. The strips on the ϕ side run axially. The z sides have strips of n^+ material; these strips are more negatively doped than the lightly doped bulk material. The strips run either perpendicular to the axial strips (90 degree layers), or are tilted by a small angle (small

angle stereo, or SAS layers). The strip pitch depends on the layer, varying from 60 to 141 μm.

When the detector is reverse-biased, passage of a charged particle through the material results in the creation of electron-hole pairs. The charge then drifts and accumulates on the readout strips, providing position measurements.

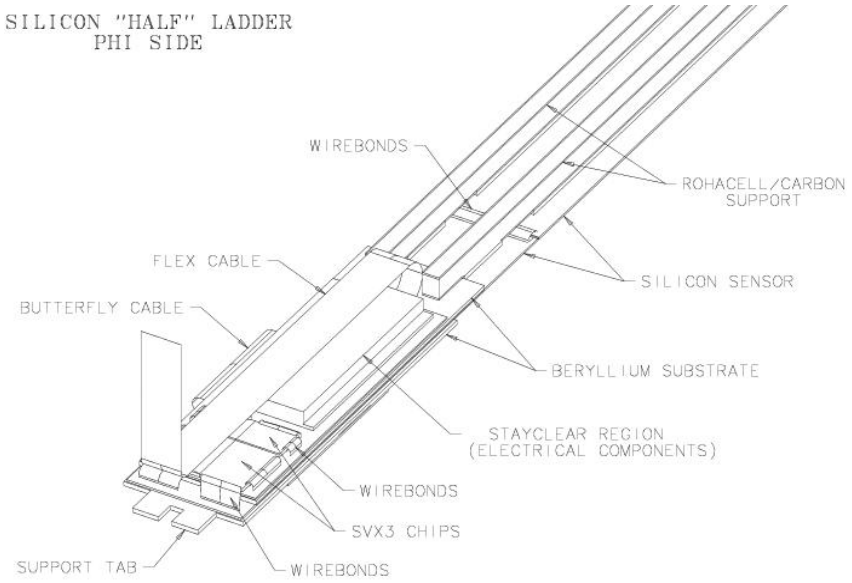

Figure 3.11: Details of a ϕ side of a "half" ladder in SVXII

A ladder assembly, shown in Figure 3.11, is composed of four silicon sensors, and is a total of 29 cm long. Readout electronics are mounted directly on top of the sensors at each end of the ladder. The ladders are arranged in an approximately cylindrically symmetric configuration, in three 29 cm long barrels. The barrels are positioned end-to-end, nominally centered on the CDF detector z-axis. Each barrel is segmented azimuthally into 12 wedges. All wedges contain 5 layers of silicon. A transverse view of the entire SVXII is shown in Figure 3.12

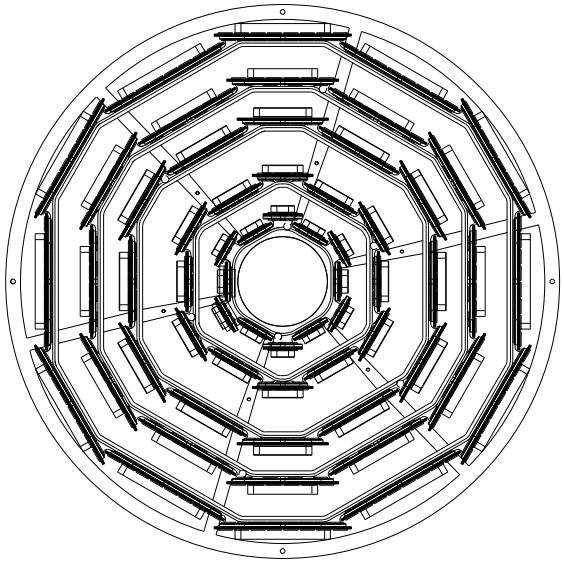

Figure 3.12: Cross-sectional view of the SVXII

The detector is read out using the 128 channel SVX3 chip. This chip is manufactured in the radiation-hard CMOS process. It has been tested to be fully functional up to a dose of 4 Megarads. Each channel contains a set of charge integrators followed by 47 cells of analog storage, and a Wilkenson ADC with 8 bits of precision [27].

Without Layer 00 or the ISL, we achieve a track impact parameter resolution σ_{d_0} of $\approx 50\mu$m. This includes a 30μm uncertainty due to the transverse size of the beam.

3.2.4 Pattern Recognition in Tracking

Track reconstruction begins in the outer tracking chamber - the COT. The first step in the pattern recognition is to form line segments from hits in each superlayer. Line segments from the axial layers which are consistent with lying tangent to a common circle are linked together to form a track. A 2d circle fit is then performed. Line segments in stereo layers are then linked to the 2d track, and finally a helix fit is performed. At this point we have a set of tracks which have only COT hits [28]. These are referred to as COT-only tracks.

The next step is to extrapolate the COT-only track into the SVX and add hits which are consistent with lying on that track. This starts in the outermost layer in the SVX. A road, or window around the track is established based on the errors on the COT track parameters. If hits lie within the road, they are added to the track. A new track fit is then performed, resulting in a new error matrix and a new road. This road is then used to add hits from the next SVX layer. This procedure is repeated until there are no SVX layers left. There may be multiple tracks with different combinations of SVX hits associated with one COT track. In this case, the track with the largest number of SVX hits is chosen [29].

The set of tracks which remain after SVX hits have been added are referred to as the "default Tracks", or `defTracks`. This is a mix of tracks with varying numbers of SVX hits. Some tracks have had no SVX hits added. These are referred to as COT-only tracks. Every track in `defTracks` has a unique COT-only parent, which is stored in the event record. We point this out here, because in this analysis we sometimes prefer the COT-only tracks. This means we use the COT-only parent of

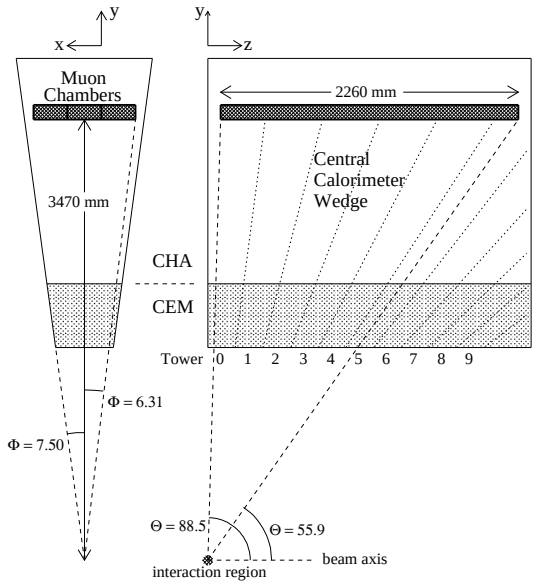

Figure 3.13: Location of Central Muon Detector(CMU) inside of central calorimeter.

a given `defTrack`.

3.2.5 Muon Systems

There are 4 muon systems in CDF: the Central Muon Detector (CMU), Central Muon Upgrade Detector (CMP), Central Muon Extension Detector (CMX), and Intermediate Muon Detector (IMU). For this analysis, we make use of the first three, which were installed in Run I.

All muon systems are located behind both the electromagnetic and hadronic calorimeters, which function as absorbers for particles which are not muons. Electrons are absorbed in the electromagnetic calorimeter, where their energy loss is dominated by bremsstrahlung. The amount of energy lost is proportional to $1/m^2$. Hadrons (pions and kaons) are absorbed in the hadronic calorimeter. Muons do not interact hadronically, and pass through. Pions and kaons which survive passage through

the calorimeter are a source of non-muon background, and are referred to as "punch through".

CMU

The CMU is the oldest muon detector, and is fully documented in [30]. It covers $|\eta| < 0.6$, and is embedded in the cylindrically symmetric central calorimeter, at a radius of 347 cm. The muon chambers are segmented in ϕ into 12.6° wedges. The calorimeter towers cover 15°, so there is an uninstrumented gap in muon coverage of 2.4° between wedges. The wedges are divided further in ϕ into three modules, as can be seen on the left top of Figure 3.13. Each of these three modules contains 4 layers of 4 rectangular drift cells, with dimensions 63.5 mm (x) × 26.8 mm (y) × 2262 mm (z). Each has a 50 μm sense wire, which runs parallel to the z-axis, located at the center of the cell. A diagram of one module is shown in Figure 3.14.

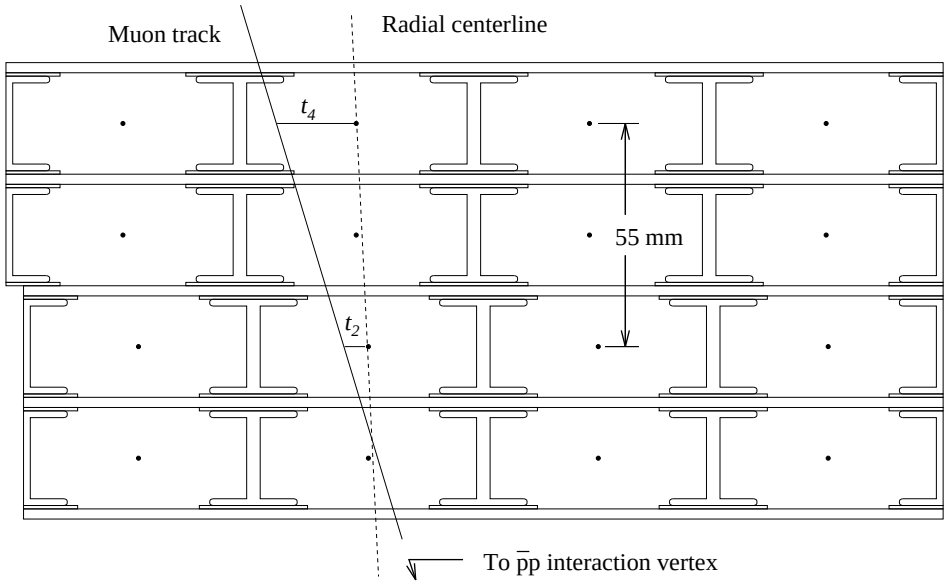

Figure 3.14: End view of a CMU module, with 4 layers of 4 rectangular drift cells. Each cell has a 50μm sense wire in the center.

CMP

The CMP is a second set of muon chambers, again with coverage up to $|\eta| < 0.6$. It covers only 53% of the azimuth, and forms a box around the central detector. Approximately 0.5% of charged pions are sources of punch through in the CMU [31]. To reduce this background in the CMP, it is situated behind an additional 60 cm of steel. As in the CMU, the drift cells are rectangular, but with cross-sectional dimensions of 2.5 cm $\times$ 15 cm.

CMX

The CMX covers $0.6 < |\eta| < 1.0$. "It's the most beautiful of the muon detectors [35]." It consists of a conical arrangement of drift cells and scintillation counters, which are used to reject background based on timing information.

The CMX covers 240° in ϕ. At the top is a 30° gap for the Tevatron Main Ring and the solenoid refrigerator. There is a 90° gap at the bottom, due to interference with the floor of the collision hall. This section, called the miniskirt, is being instrumented for Run II.

The drift cells differ from those of the CMP only in length. They are arranged in azimuthal sections, as is the case in the central detector: in each of the 24 ϕ sectors, there are 4 layers of 12 drift cells. Adjacent layers are offset by one half cell, in order to reduce ambiguities.

3.2.6 Muon Stubs

A muon tower consists of 4 drift tubes, with successively larger radii. The drift tubes are filled with Argon-Ethane. As in the COT, when a charged particle passes through, it leaves a trail of ionization. The electrons liberated during the ionization drift towards the sense wire at high voltage, causing an avalanche. Pulses generated by the avalanches are sent to amplifier-shaper-discriminators in the collision hall, which in turn generate differential digital pulses. TDC's (time to digitial converters) give hit times for the pulses. The hit times are used to reconstruct short tracks, referred to as "stubs".

Muon stubs are matched to tracks in the drift chamber. Tracks are extrapolated to the muon chambers, and the distance between the track and stub is computed. To obtain quality muons, we place an upper limit on the value of the quantity χ^2_ϕ. This is the χ^2 of the track-muon match. It is computed based the distance between the track and stub, the difference in direction of the track and stub, and the covariance matrix of the track.

3.3 The CDF Offline

Though the CDF Offline software is not part of the detector, we include it here.

After data is accepted by the trigger and written to disk, it is copied to tape. Reconstruction code called Production is then run on the raw data. Production is run by the Farms Processing Systems [36] in the Feynman Center. During Production, the code which produces the physics quantities required by most analyses is run. Tracking, muon finding, primary vertex finding, calorimetry and jet clustering are a few examples. In this analysis, we use output of the 4.8.4a version of Production.

Chapter 4

Data Sample and Event Selection

4.1 Control Sample

For our measurement of the Λ_B lifetime, we select a sample of Λ_B candidates consistent with the decay chain $\Lambda_B \to J/\psi\Lambda$ followed by $J/\psi \to \mu^+\mu^-$ and $\Lambda \to p^+\pi^-$. In addition to the Λ_B signal sample, we select a control sample of B^0 candidates consistent with the decay chain $B^0 \to J/\psi K_s^0$ followed by $J/\psi \to \mu^+\mu^-$ and $K_s^0 \to \pi^+\pi^-$. The B^0 control sample is kinematically similar to the Λ_B sample but is approximately four times as large. The B^0 lifetime is known with a precision of 1% [56]. We use this relatively large, independent control sample of known lifetime to optimize Λ_B selection criteria, to test the lifetime fitting method, and to evaluate sources of systematic uncertainty.

Like the decay $\Lambda_b \to J/\psi\Lambda$, $B^0 \to J/\psi K_s^0$ includes one J/ψ and one long-lived neutral particle. A cartoon of these decays is shown in Figure 4.1. Yet there are significant differences. The K_s^0 has a mean decay length($c\tau$) of 2.7 cm, while the

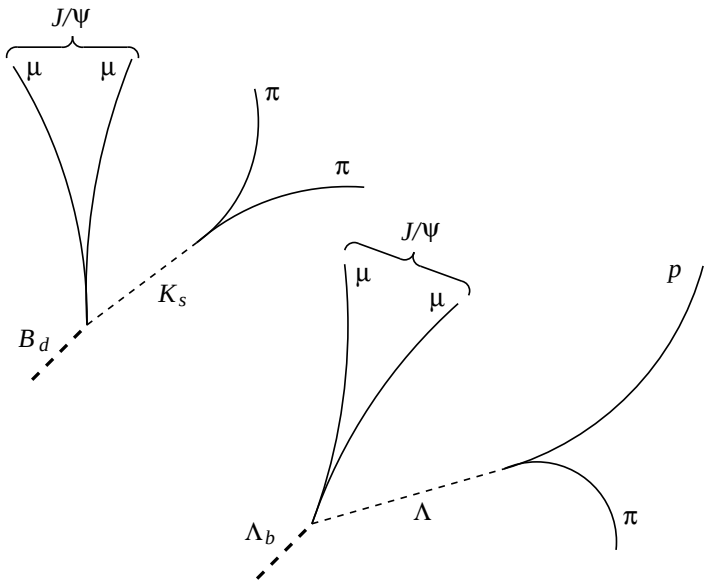

Figure 4.1: Conceptual diagram of $B^0 \to J/\psi K_s^0$ and $\Lambda_b \to J/\psi\Lambda$ decays.

Λ's is longer: 7.9 cm. The decay $K_s^0 \to \pi^+\pi^-$ has a higher Q-value than that of $\Lambda \to p^+\pi^-$ (218 MeV compared to 38 MeV). That is, the mass of the Λ decay is closer to the sum of the masses of its decay products. The result of this is that the pion from Λ decay is softer than that from K_s^0 decay. About 75% of the pions from Λ decay (in the case of $\Lambda_b \to J/\psi\Lambda$) have a transverse momentum less than 500 Mev, whereas this is only true for about 30% of K_s^0 decays. This results in a lower reconstruction efficiency for Λ, since the COT tracking efficiency falls sharply below 500 MeV [38].

Since the proton is so much more massive than the pion, it almost always has at least 3 times the momentum of the pion. This also is not true in the case of $K_s^0 \to \pi^+\pi^-$. Figure 4.2 shows p_T of the harder pion vs pt of the softer pion for K_s^0 decays, from $B^0 \to J/\psi K_s^0$ Monte Carlo, and $p_T(p)$ vs. $p_T(\pi)$ from Λ decays, from

$\Lambda_b \to J/\psi\Lambda$ Monte Carlo. We have plotted transverse momenta at the generator level. (No detector simulation was used.)

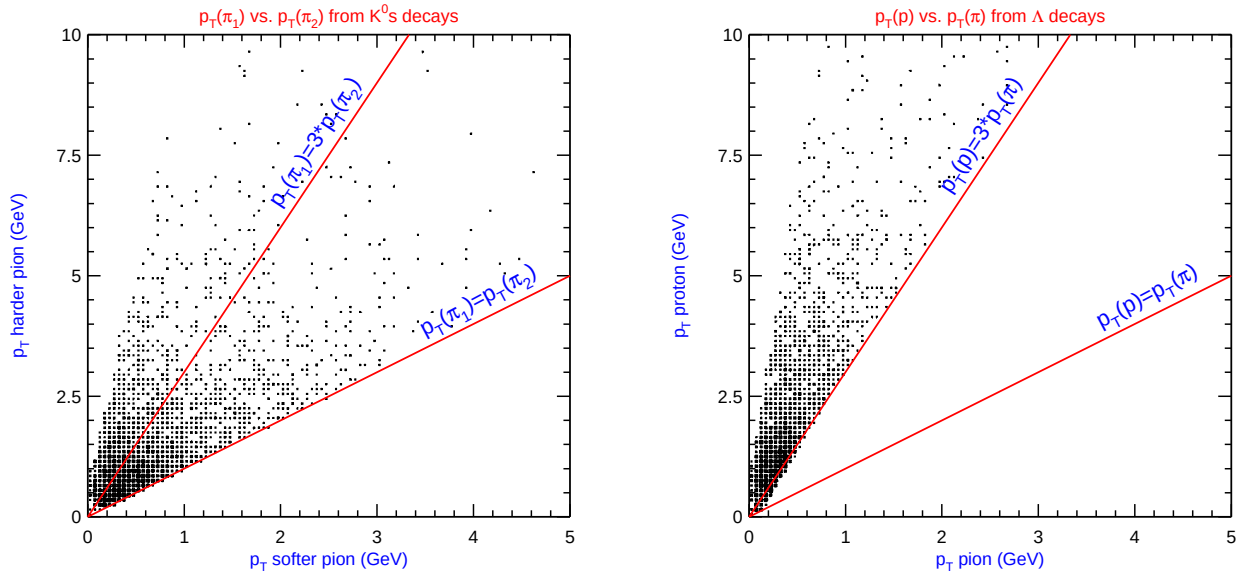

Figure 4.2: p_T of proton vs. p_T of pion in Λ decay and p_T of high momentum pion vs. p_T of low momentum pion in K^0_s decay. The plot on the left shows $p_T(\pi_1)$ vs. $p_T(\pi_2)$ from K^0_s decay. π_1 is the pion with larger p_T. The plot on the right shows $p_T(p)$ vs. $p_T(\pi)$ from Λ decay. Plots are from $B^0 \to J/\psi K^0_s$ and $\Lambda_b \to J/\psi\Lambda$ Monte Carlo generated without simulation. Lines draw on the plots represent $y = x$ and $y = 3x$.

4.2 Data Sample and J/ψ Selection

4.2.1 Data Sample

Our data is the $J/\psi \to \mu^+\mu^-$ sample. It is defined by specific trigger requirements at Level 1 and Level 3. In this data sample, any event which passes the Level 1 J/ψ trigger is automatically accepted by Level 2.

To be considered a J/ψ candidate at Level 1, there must be either two muon stubs in the CMU, or one muon stub in the CMU and one in the CMX. The muon stubs must be matched to an XFT track. The XTRP [39] extrapolates the XFT tracks into the muon chambers. Taking into account multiple scattering and alignment corrections, it determines a maximum $\delta\phi$ between the track and muon stub. In the CMU, the XFT tracks are required to have $p_T > 1.5$ GeV. Stubs in the CMX must match an XFT track with $p_T > 2.0$ GeV.

As noted above, if an event passes the Level 1 J/ψ trigger it is automatically accepted by Level 2, and passed on to Level 3. At Level 3, all muon pairs are required to have opposite charge. Muon matching requirements are again enforced. The requirement is Δx(track,stub)$<$ 30 cm for CMU muons and Δx(track,stub)$<$ 50 cm for CMX muons. The two muon tracks are required to have $\Delta z < 5$ cm at the point of closest approach to the origin. Finally, for an event to be part of the J/ψ dataset, it is required that $2.7 < m_{\mu\mu} < 4$ GeV, where $m_{\mu\mu}$ is the invariant mass of the dimuon pair. A list of the Level 3 J/ψ trigger paths is shown in Table 4.2. For about half of the data used in this analysis, Level 3 placed a requirement on the dimuon pair: $\Delta\phi(\mu,\mu) < 2.25$ radians. This was essentially dropped in later data by adding a new Level 3 trigger without this requirement.

In CDF jargon, the datasets which correspond to the trigger paths described above are called `jbot0h` and `jpmm08`. The former is a stripped version of the J-stream muon data sample, `jbmu08`, which contained all muon events (not only J/ψ), and was processed with the 4.8.4 version of Production. In the stripping, events which passed the Level 3 J/ψ trigger are selected. The second sample contains later data, after the splitting scheme was changed so that J/ψ events were separated from other muon data at Level 3. It was also processed by Production from offline version 4.8.4.

A lifetime measurement of the Λ_B requires that the position of the J/ψ vertex is well measured in the SVX. We require SVX information on the muons, which restricts us to a subsample of the data where the SVX was fully functioning. This was not always true during the earlier running periods. This results in a sample which contains ≈ 65 pb^{-1} of integrated luminosity.

Before PHYSICS_1_02_v2 (requires $\Delta\phi(\mu,\mu) < 2.25$)	L3_JPSI_CMUCMU L3_JPSI_CMUPCMU L3_JPSI_CMUCMX L3_JPSI_CMUPCMX L3_JPSI_CMU2CMU1.5
PHYSICS_1_02_v2 and later	L3_JPSI_CMUCMU L3_JPSI_CMUPCMU L3_JPSI_CMUCMX L3_JPSI_CMUPCMX L3_JPSI_CMUCMU_ALLPHI L3_JPSI_CMUCMX_ALLPHI L3_JPSI_CMUCMU_HIGHPT L3_JPSI_CMUCMX_HIGHPT L3_JPSI_CMU2CMU1.5

Table 4.1: This table lists the Level 3 J/ψ Triggers. To be part of the datasets used in this analysis, an event must have passed one of these triggers. The various triggers include J/ψ's with both legs in the CMU, one in CMU and one in CMX, and one in the CMX with the other in both the CMU and CMP. In the second part of the table, events passing L3_JPSI_CMUCMU are a subset of those passing L3_JPSI_CMUCMU_ALLPHI. All triggers whose names do not have an _ALLPHI subscript require that $\Delta\phi(\mu,\mu) < 2.25$. The _HIGHPT triggers have a looser requirement on dimuon invariant mass than the other triggers ($2 < m_{\mu\mu} < 5$), but require that the vector sum of p_T for the dimuon pair be greater than 9 GeV.

CMU muons	$\Delta x < 30$ cm $p_t > 1.5$ GeV
CMX muons	$\Delta x < 50$ cm $p_T > 2.0$ GeV
Dimuons	$\Delta z > 5$ cm $2.7 < m_{\mu\mu}(\mathrm{GeV}) < 4.0$ opposite charge muon tracks

Table 4.2: This table lists the Level 3 Trigger requirements on muons and dimuon pairs. It can be used to define all triggers in Table 4.2. For instance, L3_JPSI_CMUCMU_ALLPHI has the requirements listed as CMU muons applied to both muons.

4.2.2 J/ψ Reconstruction

We begin the reconstruction of J/ψ's by selecting muons with $p_T > 1.5$ GeV. The muons can be of any type: CMU, CMP, CMUP, or CMX. We select only muons whose corresponding tracks have 3 or more $r-\phi$ hits in the SVX. We also impose track quality requirements by requiring a minimum number of COT axial(20) and stereo(16) hits on the muon tracks.

The dimuon invariant mass is determined using the kinematic fitting program, `CTVMFT` [40], with the C++ wrapper `VertexFit`. Here, the two muons are constrained to come from a common vertex. The dimuon invariant mass distribution is shown in Figure 4.3. We require that the probability of the χ^2 of this fit be greater than 0.1%, in order to reject background. The distribution of $Prob(\chi^2)$ for signal and background is shown in Figure 4.3. The signal is assumed to have a mass within $\pm 3\sigma_m$ of the fitted J/ψ mass, where σ_m is the fitted width of the J/ψ mass peak. The background is taken from the sidebands of the J/ψ mass peak.

A perfect distribution of $Prob(\chi^2)$ for signal is flat from zero to one. A large number of events in bins near zero indicates the presence of background. Mismeasured tracks and incorrect errors on track parameters also cause an excess near zero.

Figure 4.4 shows the mass distribution for all J/ψ's which pass our requirements. We fit the mass distribution to a double gaussian, and obtain $\sim 612,000$ candidates. The requirements are summarized in Table 4.3. As discussed in Section 4.5, we drop SVX stereo hits, Layer 00 hits, and ISL hits on the J/ψ legs for the lifetime measurement. This is *not* done in Figure 4.4. Here we simply require 3 or more $r\phi$ hits, where the hits can be from any SVX layer.

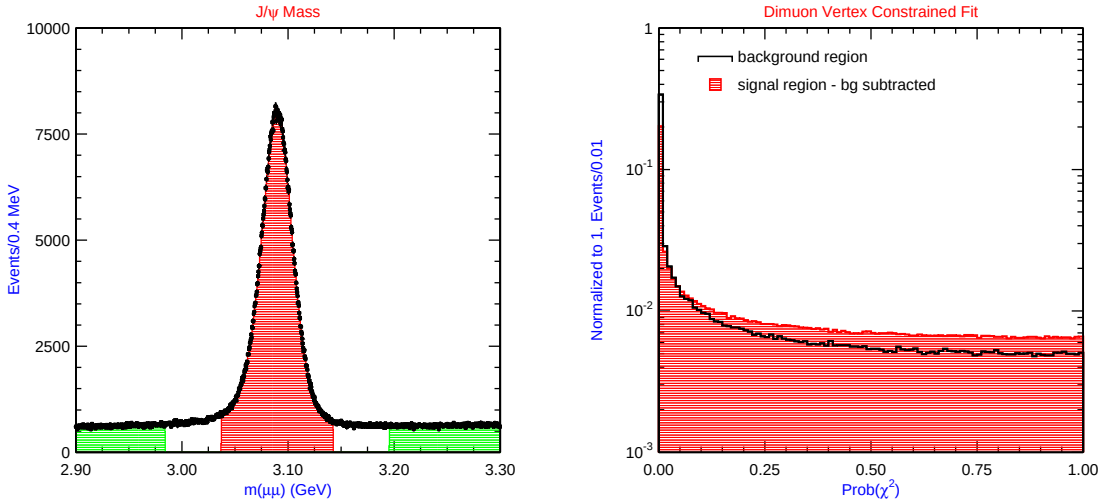

Figure 4.3: J/ψ mass distribution, from the J/ψ sample(left), showing signal region and sideband (background) region in the shaded areas. Distribution of $Prob(\chi^2)$ (right) for vertex constrained dimuon fit, for signal and background. The histograms at the right are normalized to unit area.

Tracks	N (COT axial) ≥ 20 N (COT stereo) ≥ 16
Muons	≥ 3 $r-\phi$ SVX hits $p_T(\mu) > 1.5$ GeV
J/ψ	$Prob(\chi^2) > 0.1\%$

Table 4.3: Requirements for J/ψ candidates

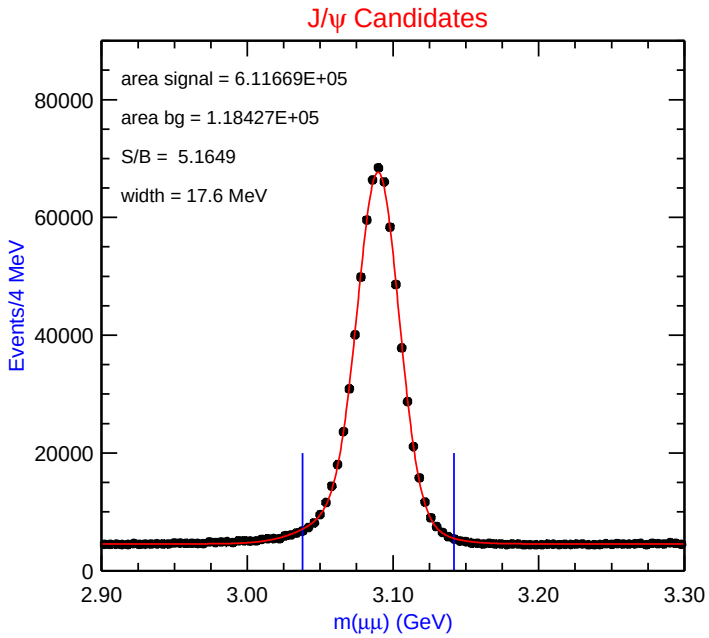

Figure 4.4: Mass distribution for $J/\psi \rightarrow \mu^+\mu^-$ candidates with selection requirements. The lines on either side of the peak represent the $\pm 3\sigma_m$ points. We integrate the fitted double gaussian between these points, and obtain 612k signal J/ψ's. As discussed in Section 4.5, we drop SVX stereo hits, Layer 00 hits, and ISL hits on the J/ψ legs for the lifetime measurement. This is *not* done in this plot. Here we simply require 3 or more $r\phi$ hits, where the hits can be from any SVX layer.

4.2.3 Monte Carlo

To determine our requirements as defined in the following sections, we optimize $S^2/(S+B)$, where S and B are the number of signal and background events in the signal region. For the signal, we use a Monte Carlo for $B^0 \to J/\psi K^0_s$. For the background, we use the B^0 sidebands from data. The Monte Carlo event generator is `BGenerator` [41]. The decays of B hadrons are handled by the CDF interface to `CLEOMC` [42]. For the detector simulation, we use `CdfSim` [43].

4.3 Λ and K_s^0 Selection

We reconstruct Λ's and K_s^0's by looping over pairs of oppositely charged tracks in J/ψ events and forming their invariant mass. We exclude muons which come from J/ψ's passing our requirements. If the mass is between 0.4 and 0.6 GeV for a K_s^0, or 1.08 and 1.18 GeV for a Λ, the pair is kept as a possible candidate. Since there are many track combinations, we speed up this process by first calculating the invariant mass without a vertex constrained fit.

For tracks from promptly decaying particles

$$p_x = p_T \cos(\phi_0), p_y = p_T \sin(\phi_0) \tag{4.1}$$

where ϕ_0 is the ϕ coordinate of the track at its point of closest approach to the origin. Equation 4.1 does not hold for the daughter tracks of long-lived particles, where the distances of closest approach of the tracks are not the same as the particle decay point. This is illustrated in Figure 4.5.

To compute the momenta, we obtain the geometrical intersection of the two tracks in the transverse plane. Then

$$p_x = p_T \cos(\phi_{int}), p_y = p_T \sin(\phi_{int}) \tag{4.2}$$

where ϕ_{int} is the ϕ coordinate of the two track intersection. We compute the raw mass using the above momenta. For K_s^0 reconstruction, we assume the pion mass for both tracks, and for Λ reconstruction we assume the proton mass for the higher momentum track, and the pion mass for the lower momentum track. If the raw mass is between 1.0 and 1.18 (0.4 and 0.6) GeV for the Λ (K_s^0) we perform a vertex constrained fit to

obtain a more precise value for the invariant mass. As with the J/ψ, we require that the probability of the χ^2 of the fit be greater than 0.1%. This value was determined by maximizing the $S^2/(S+B)$ for B^0. The effect of this requirement on the K_s^0 mass distribution is shown in Figure 4.6.

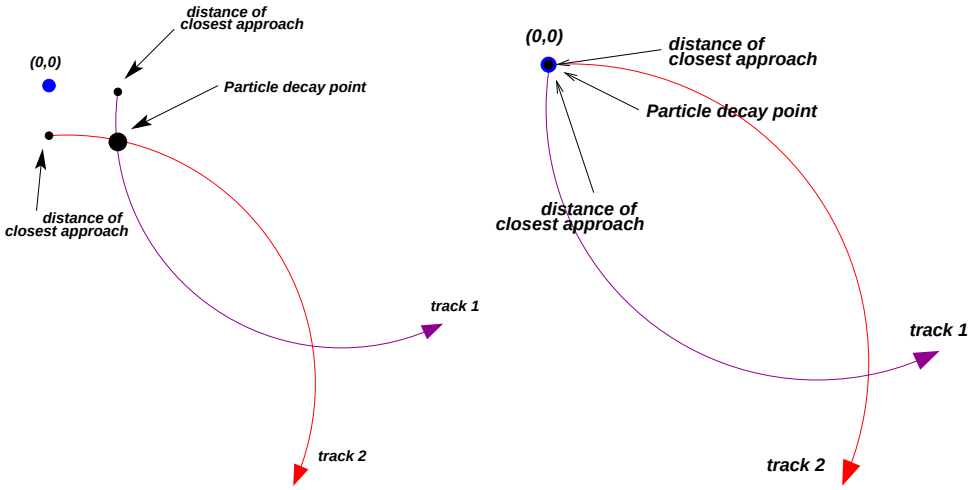

Figure 4.5: Decay of a long-lived (left) and prompt (right) particle.

Since the last layer of the SVX has a radius of 10.6 cm, tracks from a V_0 with $L_{xy} > 11$ cm should not have any SVX hits. If the decay does occur within the SVX, we would like to use the information there to obtain the most precise possible track measurements. Thus, for $L_{xy} < 11$ cm, we allow SVX hits on V_0 daughters. In making the V_0 selection, and in computing the invariant masses, we divide the sample into two sub-samples: one for which $L_{xy}(V_0) < 11$ cm, and one for which $L_{xy}(V_0) > 11$ cm. We use `defTracks`, which often have SVX hits, for the V_0 daughters in the first sample (See Section 3.2.4 for a description of different track types). We use COT

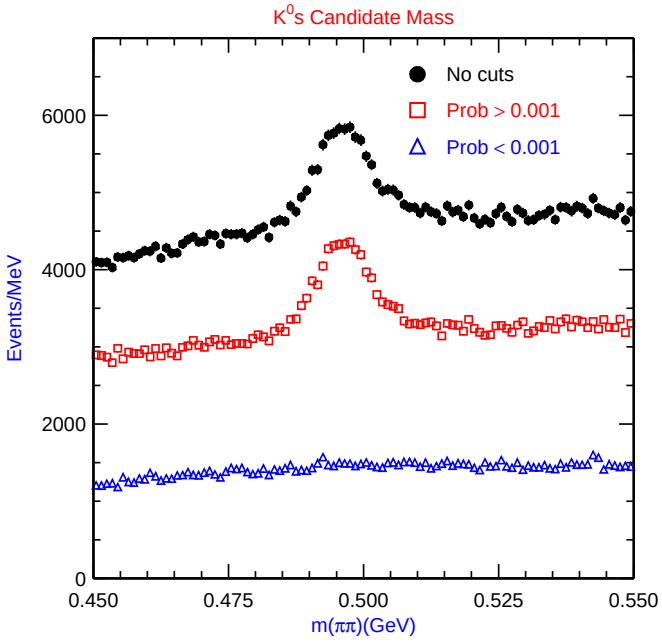

Figure 4.6: $m_{\pi\pi}$ for K^0_s candidates from the J/ψ sample. The histogram shown in solid circles is the K^0_s invariant mass with only a requirement that $p_T(\pi) > 400$ MeV. The histogram with open squares shows the K^0_s invariant mass with a requirement of 0.001 on $Prob(\chi^2)$ of the 2 track kinematic fit. The histogram with open triangles is the result when the anti-requirement is applied.

only tracks for the second sample.

When using `defTracks`, we drop the SVX hits at radii smaller than that of the V_0 decay vertex. This is discussed in greater detail in Section 4.5

In order to increase our signal purity, we require that $L_{xy}(K^0_s,\Lambda) > 0.25$ cm. Figure 4.7 and Figure 4.8 show mass and L_{xy} distributions for K^0_s and Λ candidates in the J/ψ sample.

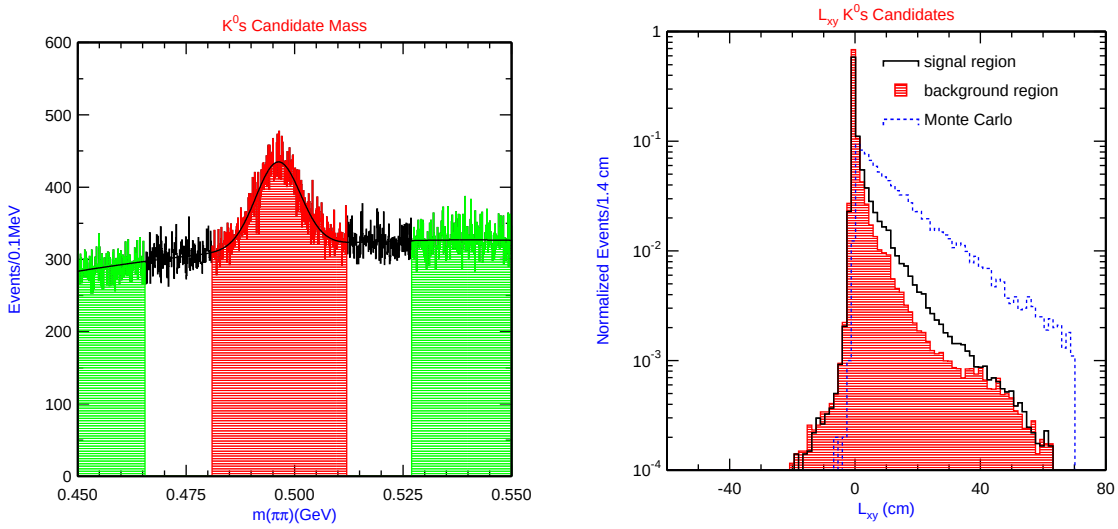

Figure 4.7: Left: K_s^0 mass distribution for K_s^0 candidates in the J/ψ sample: We require $Prob(\chi^2)$ >0.001, $p_T(\pi) > 400$ MeV, and $5.1 < m_{\mu\mu\pi\pi} < 5.5$ GeV. The shaded regions are the signal and background regions. Right: $L_{xy}(K_s^0)$ for signal region, background region, and signal Monte Carlo. For the B^0 sample we require $L_{xy} > 0.25$ cm.

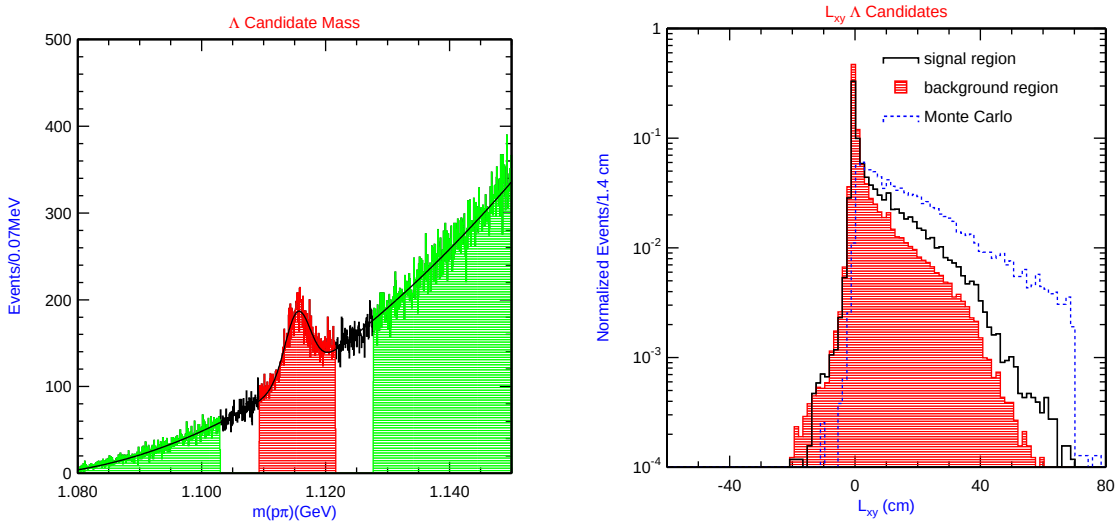

Figure 4.8: Left: Λ mass distribution for Λ candidates in the J/ψ sample: We require $Prob(\chi^2)$ >0.001 and $5.4 < m_{\mu\mu p\pi} < 5.8$ GeV. The shaded regions are the signal and background regions. Right: $L_{xy}(\Lambda)$ for signal region, background region, and signal Monte Carlo. For the Λ_B sample we require $L_{xy} > 0.25$ cm.

We have also investigated making requirements on $L_{xy}/\sigma_{L_{xy}}$ and d_0/σ_{d_0}. A simple requirement on L_{xy} yielded the best $S^2/(S+B)$ and efficiency. It is true that a requirement on decay length which is optimal for K_s^0's will not be optimal for Λ's. Since Λ's are longer lived than K_s^0's, we expect that a more stringent requirement would result in a cleaner signal. For the time being, however, we leave the requirements for both samples the same. In the future, with higher statistics, a more stringent requirement on L_{xy} of the Λ will be an option worth considering.

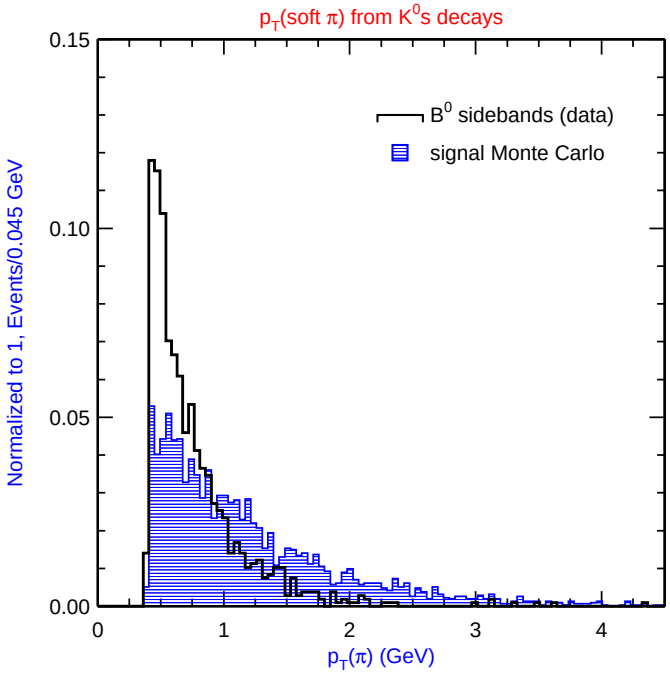

Figure 4.9: p_T of the softer π from K_s^0 decay. The shaded histogram is from $B^0 \rightarrow J/\psi K_s^0$ signal Monte Carlo. The unshaded histogram shows the background; it is made using the B^0 sidebands. We require $p_T > 0.4$ GeV. It is still evident that the background rises substantially more than the signal below 0.4 GeV.

In order to reduce background and execution time for our jobs, we require that the p_T of the K_s^0 daughter pions be greater than 400 MeV. Figure 4.9 shows p_T of the

softer pion in data (background) and Monte Carlo. The background for $B^0 \to J/\psi K_s^0$ increases drastically below 400 MeV, but the signal does not. We do *not* require $p_T >$ 400 MeV for the pions from Λ's. This is inefficient for soft pions resulting from the asymmetric decay. Monte Carlo with simulation predicts that 35% of reconstructed Λ decays have $p_T(\pi) < 400$ MeV, where this is only true for 23% of the K_s^0 decays. Also, we are more concerned about efficiency in the case of the Λ_B, since the number of decays reconstructible is smaller than that for B^0.

There is one additional complication in Λ selection. There is a non-negligible probability of reconstructing a Λ out of a true K_s^0 if the proton/pion mass hypothesis is assumed for the track pair. Thus, when we are reconstructing Λ's, we also try the pion/pion mass hypothesis for each track pair. If the invariant mass falls within the window 0.48 to 0.513 GeV, we no longer consider this a Λ candidate.

4.4 B^0 and Λ_B selection

We reconstruct the B^0 and Λ_B by performing a 4-track kinematic fit with the two J/ψ muons, and the V_0 (K_s^0 or Λ) decay daughters. Each of these tracks must have at least 20 axial hits and 16 stereo hits in the COT, to insure that they are well-measured. In the 4-track fit we require that the two muons come from a common vertex, and that the two pions, (or the proton and the pion in the case of the Λ) come from a common vertex. We also constrain the dimuon mass of the J/ψ candidate to the world average J/ψ mass of 3.097 GeV [56], for better resolution.

The mass pull is defined as

$$\left(\bar{m} - m^i(\mu\mu)\right) / \sigma^i_{m(\mu\mu)} \tag{4.3}$$

where $\bar{m}$ is the fitted mean J/ψ mass, $m^i(\mu\mu)$ is the per event dimuon mass, and $\sigma^i_{m(\mu\mu)}$ is the per event error on the dimuon mass. The reconstructed J/ψ mass and mass pull for events in which the K^0_s and J/ψ have an invariant mass between 5.1 and 5.5 are shown in Figure 4.10.

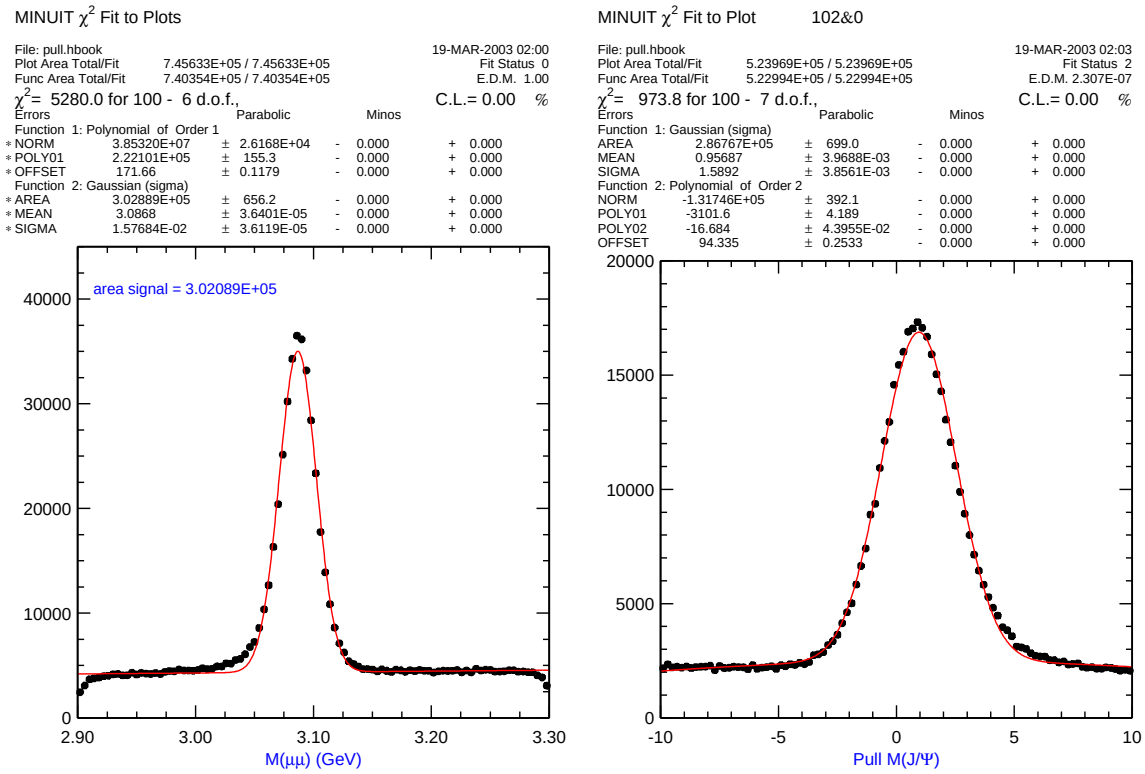

Figure 4.10: $m_{\mu\mu}$ and pull distribution for J/ψ candidates

Ideally, we should obtain the world average mass of 3.097 GeV, and a pull centered at zero with unit width. A width greater than one indicates that the errors on the track parameters are underestimated. We find that the central value of the mass is 10 MeV low, and the width of the mass pull distribution is about 1.6. Current studies indicate that these effects are due mainly to an underestimation of the passive material in the SVX; the material composition and distribution are not perfectly known [46].

This should not affect the lifetime measurement.

Also in the 4-track kinematic fit, the V_0 is constrained to point back to the J/ψ in 3 dimensions. We require then that $Prob(\chi^2)$ (4-track fit) $> 0.1\%$. The distribution of $Prob(\chi^2)$ and the effect of this requirement are shown in Figure 4.11.

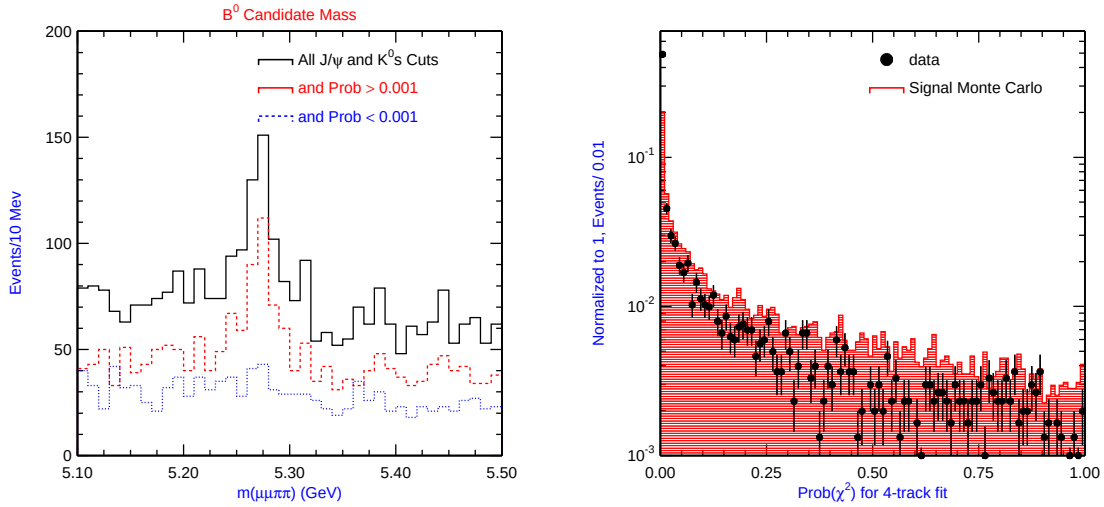

Figure 4.11: B^0 candidates with a requirement and anti-requirement on $Prob(\chi^2)$ of the 4-track fit. We enforce all of the requirements shown in Table 4.4, except for that on $Prob(\chi^2)$ of the 4-track fit.

For our final selection, we make requirements on the invariant masses of the J/ψ and V_0, and require that $\cos(\theta_T) > 0.9999$, where θ_T is the angle in the transverse plane between the V_0 momentum and the vector from the J/ψ to the V_0. The track parameters used in the computation of θ_T are those which have not been adjusted in the kinematic fitting. Here we are making a direct requirement on the value of the pointing angle, in addition to the pointing constraint we apply in the 4-track fit. This method results in the highest possible $S^2/(S+B)$ for the B^0 , which is not attainable with only a requirement on $Prob(\chi^2)$ of the 4-track fit. Figure 4.12 shows the distribution of $\cos(\theta_T)$ for B^0 candidates with an invariant mass between

5.1 and 5.5 GeV, along with the distribution for signal Monte Carlo. Here we apply all analysis requirements shown in Table 4.4, except for the $\cos(\theta_T)$ requirement. Figure 4.13 shows the B^0 mass distribution with and without the requirement on $\cos(\theta_T)$. We lose no signal events, and increase the $S^2/(S+B)$ from 62 to 75.

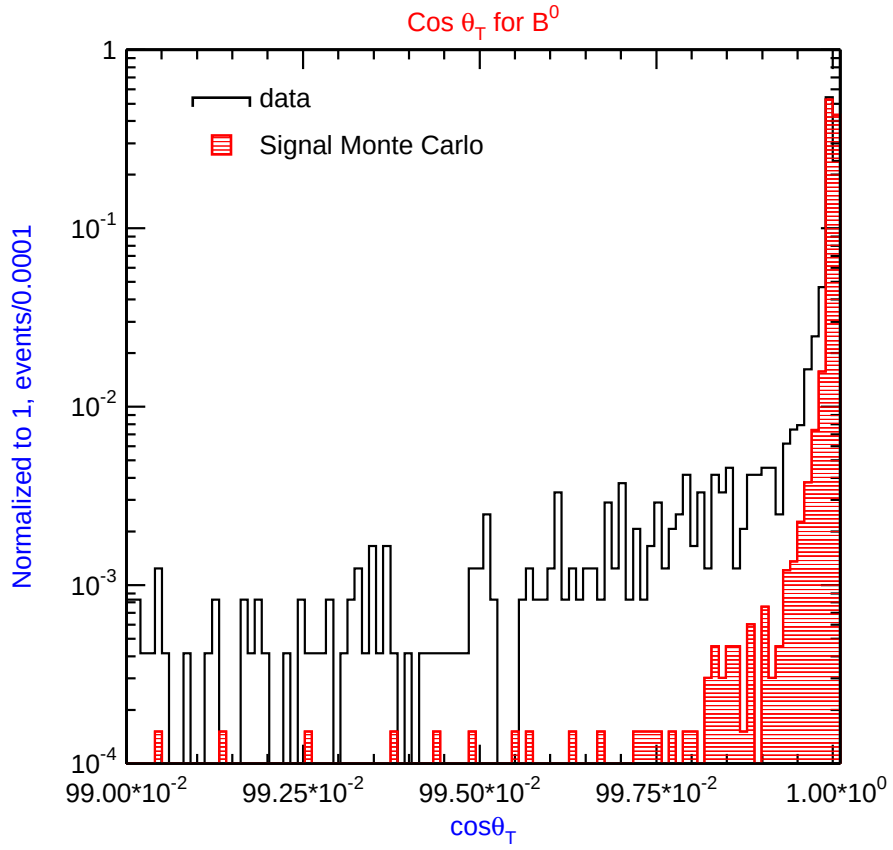

Figure 4.12: Distribution of $\cos(\theta_T)$ for data and signal Monte Carlo. We enforce all of the requirements listed in Table 4.4, except for that on $\cos(\theta_T)$.

We have also investigated making requirements based on the impact parameter of the V_0 with respect to the J/ψ vertex, but we find that the $\cos(\theta_T)$ requirement is better for significance and efficiency.

We require that $p_T(B_0)$ or $p_T(\Lambda_B) > 4.5$ GeV/c. Figure 4.14 shows the distribu-

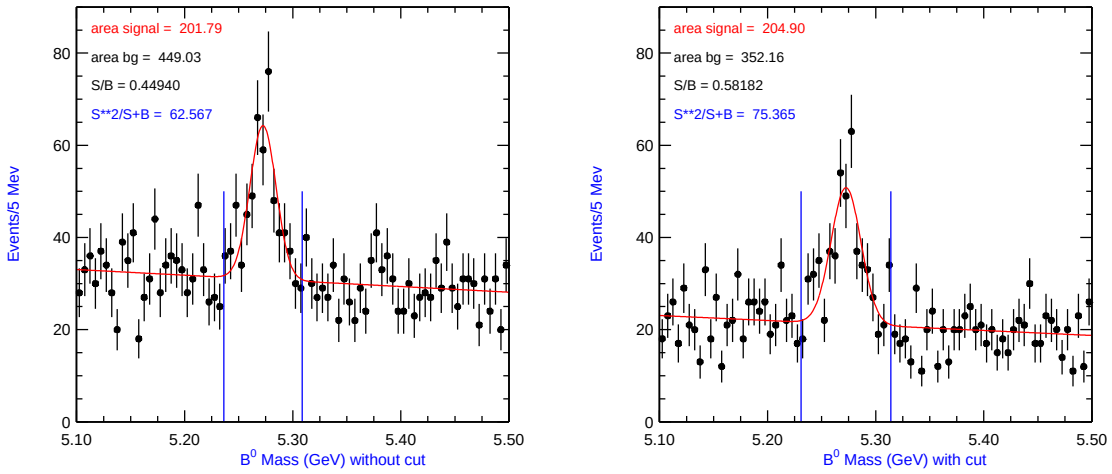

Figure 4.13: B^0 candidates without (left) and with (right) $\cos(\theta_T)$ requirement. We make all requirements listed in Table 4.4.

tion of $p_T(B^0)$ in the data, for B^0 invariant masses between 5.1 and 5.5 GeV, and in signal Monte Carlo.

Figure 4.15 shows the candidate B^0 and Λ_B after making all of the analysis requirements (those listed in Table 4.4). We obtain 205 $\pm$ 28 B^0 candidates, and 52 $\pm$ 15 Λ_B candidates.

Figure 4.16 shows the invariant mass distributions for K^0_s and Λ, with all analysis requirements, excluding the K^0_s or Λ invariant mass requirement. As described in Section 4.3, we divide our data sample into two subsamples depending on $L_{xy}(V_0)$. We allow SVX hits on tracks for V_0's with $L_{xy} < 11$ cm, wheras for $L_{xy} > 11$ cm we use COT-only tracks when computing any V_0 related quantities. For the B^0 there are approximately an equal number of events in each subsample. For the Λ_B, 80% of the events have $L_{xy}(\Lambda)$ >11 cm.

The requirements discussed in this and the preceding sections are listed in Table 4.4.

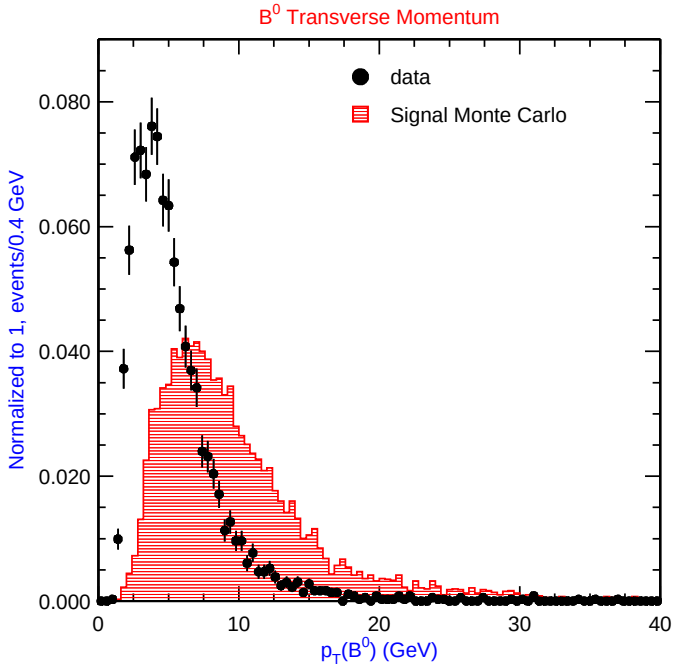

Figure 4.14: Distribution of $p_T(B^0)$ for data and signal Monte Carlo. We use all requirements listed in Table 4.4, except for that on $p_T(B^0)$.

Tracks	N (COT axial) ≥ 20 N (COT stereo) ≥ 16
Muons	≥ 3 $r-\phi$ SVX hits $p_T(\mu) > 1.5$ GeV
J/ψ	$Prob(\chi^2) > 0.1\%$ $3.01 \leq m_{\mu\mu}$ (GeV) ≤ 3.17
V_0	$Prob(\chi^2) > 0.1\%$ $0.477 \leq m_{\pi\pi}$ (GeV) ≤ 0.517 $1.104 \leq m_{p\pi}$ (GeV) ≤ 1.128 $L_{xy} > 0.25$ cm K^0_s only: $p_T(\pi) > 400$ MeV Λ only: reject events where $0.48 < m_{\pi\pi} < 0.513$, $m_{\pi\pi}$ using Λ tracks
B	$Prob(\chi^2) > 0.01\%$ $\theta_T > 0.9999$ $p_T > 4.5$ GeV

Table 4.4: Requirements in selecting Λ_B and B^0 from the J/ψ sample. The J/ψ sample is discussed in Section 4.2.

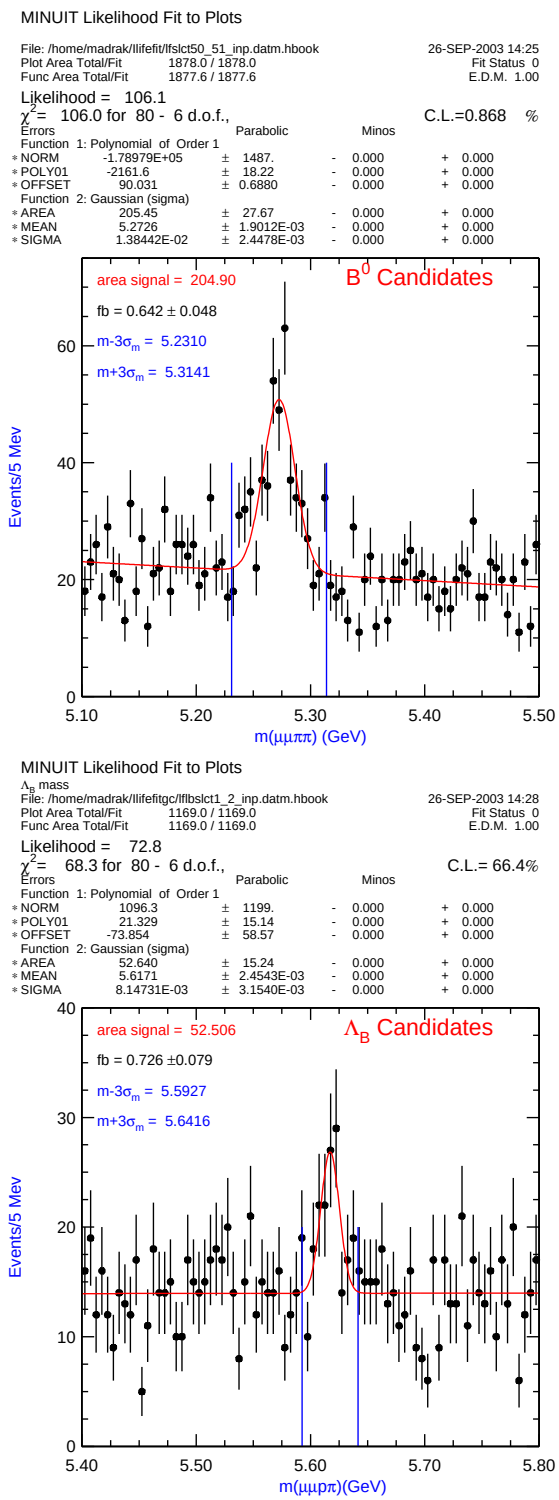

Figure 4.15: B^0(top) and Λ_B(bottom) candidates with all analysis requirements

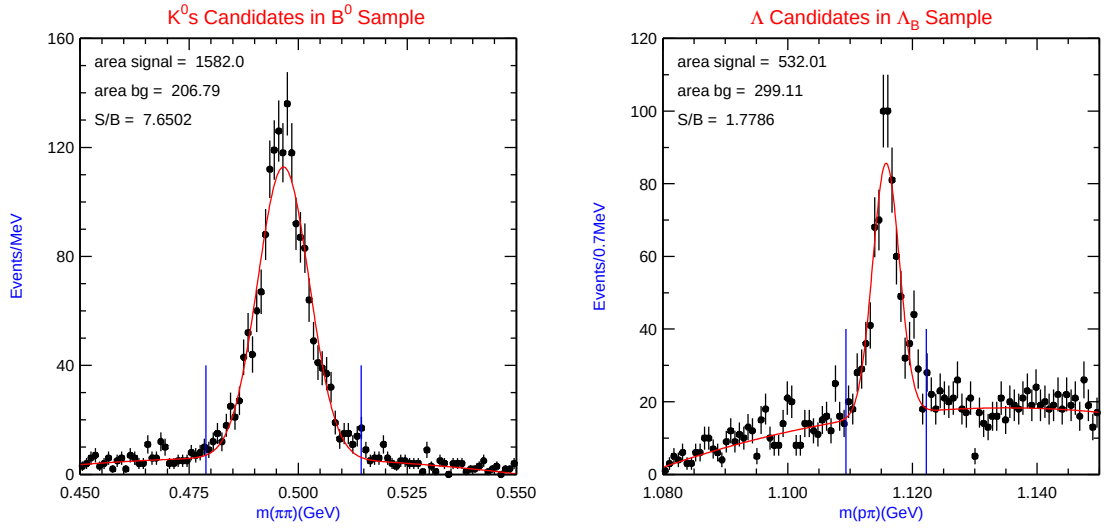

Figure 4.16: K_s^0 candidates in the B^0 sample (left) and Λ candidates in the Λ_B sample with all analysis requirements, excluding those on the K_s^0 and Λ invariant mass. All requirements are listed in Table 4.4. For the K_s^0 plot we require that the mass of the B^0 is between 5.1 and 5.5 GeV. For the Λ plot we require that the mass of the Λ_B is between 5.4 and 5.8 Gev.

4.5 Track Refitting

To account for energy loss and multiple scattering, we refit every track. To perform the refit, one must know the material through which a given track passed. In refitting muon tracks from J/ψ 's, we include all material in to $r = 0$, whereas for tracks from V_0's we only consider material outside of the V_0 decay radius.

The refit requires a starting point, or a *precursor* for the fit. This is the original COT track associated with any track. (If the track has no SVX hits, it is the track itself). It has been shown that for COT tracks, the errors returned on the track parameters are underestimated, since the COT tracking code does not account for multiple scattering in the COT volume [49]. To correct for this, we scale the error matrix of the precursor before the refit. Then, after the refit, the errors on the track parameters are more correct.

Before refitting, we drop any SVX hits attached to tracks which are from Layer 00 or ISL. The reason for this is that the pedestals in Layer 00 are not currently understood well enough for it to be used in physics analysis, and the alignment for the ISL is a work in progress.

Before refitting V_0 tracks, we drop any SVX hits which are not consistent with being on the V_0 tracks. These are SVX hits which have a radius less than r_{V_0}, the radius of decay of the V_0. Because tracks which have incorrect SVX hits attached may bias the vertex constrained fit for the V_0, we use COT-only tracks to compute r_{V0}.

To determine the position of the J/ψ vertex used for the lifetime fit, we refit the muon daughter tracks as described above. Before the refit, we drop all of the

SVX stereo hits (small angle and 90-degree stereo). We do not lose any lifetime information here, since we need only L_{xy}, the transverse decay length, and p_T, the transverse momentum of the Λ_B, to compute the proper decay time. This is shown in equation 5.1. In addition, including SVX stereo information has been shown to cause bias in other lifetime measurements [51]. This is likely a temporary problem which will be resolved when CDF's tracking software is more mature.

The SVX stereo hits are used when computing the masses and the quantities on which we make requirements. This results in a larger $S^2/(S+B)$. We make the $Prob(\chi^2)$ requirement on the J/ψ vertex in both the 2d and 3d cases. This is because we use the 2d J/ψ vertex for the evaluation of the proper decay length and the 3d J/ψ information for the computation of the invariant mass of the B^0 and Λ_B.

Chapter 5

Analysis Method

5.1 Determination of the Proper Lifetime

For each candidate Λ_B event, we reconstruct the proper decay length of the Λ_B, given by

$$ct = L \cdot \frac{1}{\beta\gamma} = L \cdot \frac{m_B}{p^B} = L_{xy} \cdot \frac{m_B}{p_T^B} \tag{5.1}$$

L is the three dimensional distance in the lab frame between the Λ_B production and decay points. p_T^B is the transverse momentum of the Λ_B. L_{xy} is the transverse distance between the Λ_B production and decay points, projected onto the Λ_B transverse momentum. The Λ_B is produced in the hard scattering of protons and anti-protons, which occurs at the primary vertex of the event. Therefore, to determine ct, we need to know 3 quantities: the x, y position of the primary vertex, the x, y position of the Λ_B decay point (the secondary vertex), and p_T of the Λ_B.

The x, y position of the primary vertex is taken from the run-averaged beamline.

Since the beam has a slope in x and y as a function of z, the beam position in x, y must be determined for a given z. We use $z = z_{VC}$, where z_{VC} is the z position of the primary vertex found by the dedicated three-dimensional primary vertex finder `VXPRIM` [52]. If more than one primary vertex is found, we choose the one with z closest to the z position of the J/ψ vertex. The distribution of $z_{J/\psi} - z_{VC}$ is shown in Figure 5.1. The width of this distribution is determined by the COT z_0 resolution, which is on the order of a centimeter. Since we drop the stereo SVX hits from the J/ψ muons, the only stereo information comes from the COT.

The secondary vertex is the J/ψ vertex. It is determined by performing a two-track vertex constrained kinematic fit for the dimuon pair. p_T of the Λ_B is determined by summing the transverse momenta of the decay products.

We reject events with poorly measured secondary vertices by requiring

$$\sigma_{ct} \approx \sigma_{L_{xy}} \cdot m/p_T < 150\mu\text{m}.$$

The distribution of σ_{ct} for the B^0 before this requirement is shown in Figure 5.2.

Figure 5.3 shows the B^0 decay length distribution (in the lab frame) and a distribution of the boost, $p_T(B^0)/m(B^0)$, from Monte Carlo.

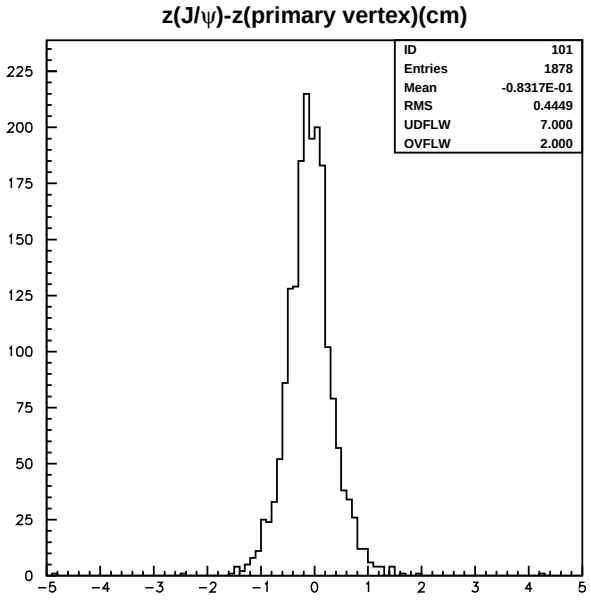

Figure 5.1: Distribution of $z_{J/\psi} - z(\text{primary vertex})$ for B^0 candidate events. We use the primary vertex which is closest in z to the J/ψ vertex.

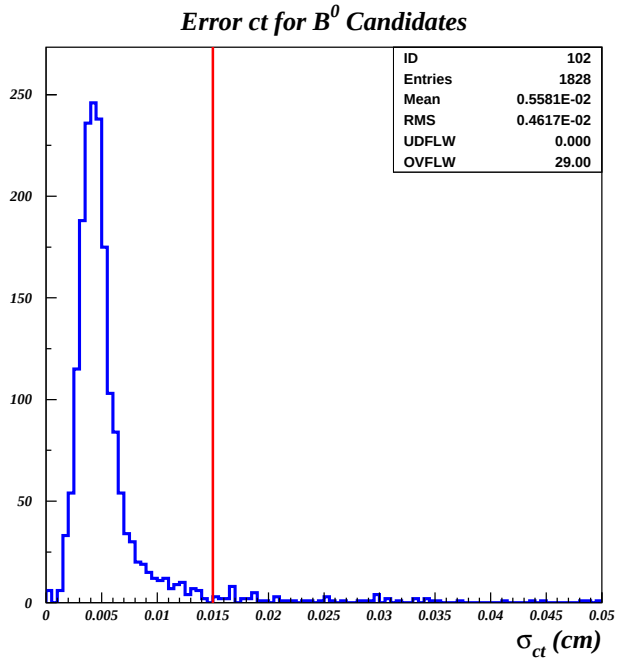

Figure 5.2: Error on proper lifetime, σ_{ct}, for B^0 candidates. We require that $\sigma_{ct} < 150\mu$m.

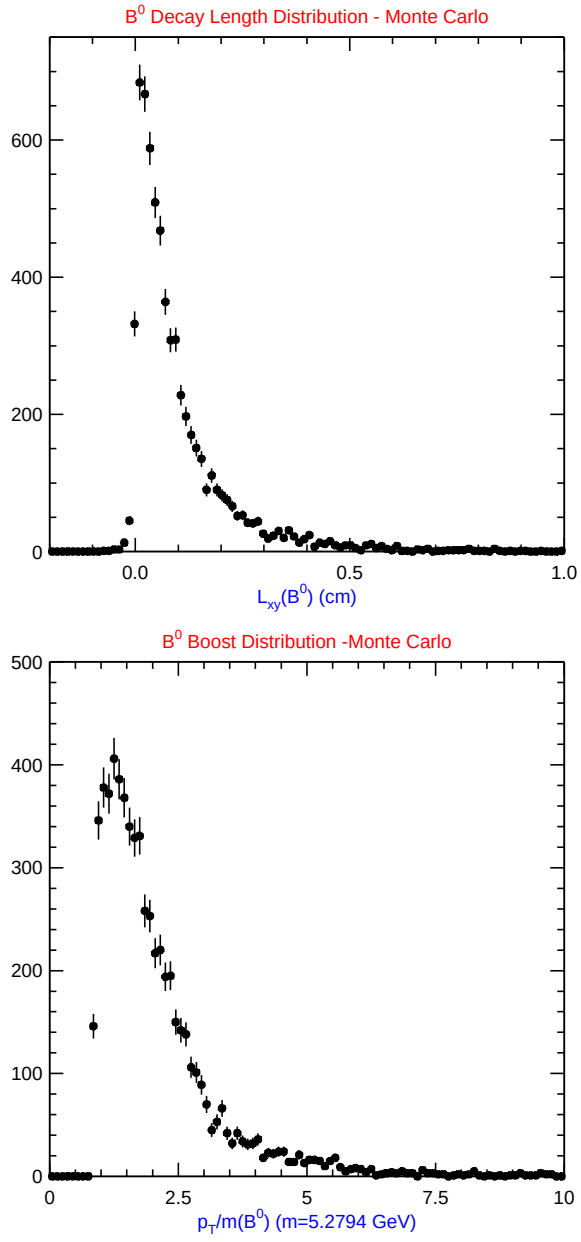

Figure 5.3: Distribution of decay length and boost for B^0, from Monte Carlo. The decay length is that in the lab frame. The boost is given by $p_T(B^0)/m(B^0)$, where $m(B^0) = 5.2794$ GeV [56]. We apply all of our analysis selection requirements, summarized in Table 4.4.

5.2 Unbinned Maximum Likelihood Fit

To extract the Λ_B lifetime, we perform an unbinned maximum likelihood fit to the distributions of ct in the Λ_B signal and sideband regions. We use two methods, which are described in the following sections. In both cases, the inputs to the fit are ct, σ_{ct}, the error on proper decay length, and m, the mass of the Λ_B candidate.

5.2.1 Method 1 - The Separate Fit

The first fitting method, which is our standard one, is unbinned for the lifetime fit only. There is a clear distinction here between signal and background regions. These regions are determined in a binned likelihood fit to a histogram of invariant mass before the lifetime fit is performed. The functional form used for the fit to the invariant mass distribution is the sum a gaussian, for the signal, and a first order polynomial, for the background. The signal region events are those with invariant masses within $3\sigma_m$ of the fitted mean mass, where σ_m is the fitted width of the gaussian mass peak. The background region events are those in the sidebands, starting at $6\sigma_m$ away from the average invariant mass. For Λ_B the upper and lower limits of the sidebands are 5.4 and 5.8 GeV. For the B^0, they are 5.183 and 5.5 GeV.

The lower limit on to B^0 mass is chosen to reject background coming from decays with similar topologies. The decays $B^+ \to J/\psi K^{*+}$, with $K^{*+} \to K^0_s\pi^+$ and $B^0 \to J/\psi K^{*0}$ with $K^{*0} \to K^0_s\pi^0$, can be reconstructed as $B^0 \to J/\psi K^0_s$ because the final states include a J/ψ and K^0_s. The reconstructed mass will be approximately m_π below the B^+/B^0 mass (the same mass), due to the missing pion. We place the lower limit at $m_{B^0} + \sigma_{m_{B^0}} - m_{\pi^0}$.

After the signal and background regions have been determined, we fit the distributions of ct to extract the lifetime. We refer to this fit as the "separate fit" because the mass distribution and the lifetime distribution fits are performed in two separate steps.

The probability density function(PDF) describing the ct distribution of signal events is:

$$F^i_{sig}(c\tau_B) = Exp \otimes G(ct^i, \sigma^i_{ct}, s_{ct}, c\tau_B) \tag{5.2}$$

$$= \frac{1}{c\tau_B} exp\left\{\frac{(s_{ct}\sigma^i_{ct})^2}{2(c\tau_B)^2} - \frac{(ct)^i}{c\tau_B}\right\} \cdot \left[1 - \text{freq}\left(\frac{s_{ct}\sigma^i_{ct}}{c\tau_B} - \frac{(ct)^i}{s_{ct}\sigma^i_{ct}}\right)\right] \tag{5.3}$$

where $(ct)^i$ and σ^i_{ct} are the measured proper decay length and proper decay length error for each event, and freq is the Normal Frequency function.

The derivation of equation 5.3 from equation 5.2 is given in [45].

The error due to the 35 μm size of the beam in the xy plane is included in σ^i_{ct}. The free parameters are $c\tau_B$, the average lifetime of the signal, and s_{ct}, a scale factor to allow for scaling of decay length errors. This allows the fit to adjust for cases in which the input errors are over or underestimated.

The background functional form is the sum of a gaussian, a positive going exponential, and a negative going exponential. The gaussian represents prompt (zero-lifetime) background smeared by detector resolution. The exponentials parametrize both tails in the resolution function and any real long-lived background.

The PDF for the background is

$$F^i_{bgr} = (1 - f_- - f_+) \cdot \frac{1}{\sqrt{2\pi} s_{ct} \sigma^i_{ct}} \cdot exp\left\{ \frac{-(ct^i)^2}{2(s_{ct}\sigma^i_{ct})^2} \right\} \tag{5.4}$$

$$+ \begin{cases} \frac{f_+}{\lambda_+} \cdot e^{(ct)^i/\lambda_+} & \text{if } (ct)^i > 0 \\ \frac{f_-}{\lambda_-} \cdot e^{(ct)^i/\lambda_-} & \text{if } (ct)^i < 0 \end{cases}$$

where λ_+ and λ_- are the characteristic lengths of the exponentials, and f_+ and f_- are the background fractions in the positive and negative tails.

For the separate fit, the full PDF is given by

$$\mathcal{F}^i_{lik} = (1 - f_B) \cdot F^i_{sig} + f_B \cdot F^i_{bgr} \tag{5.5}$$

where f_B, the background fraction in the signal region, is also a fit parameter.

We maximize the Likelihood function with respect to its free parameters $\vec{\alpha}$:

$$\vec{\alpha} = \{c\tau, s_{ct}, f_B, f^+, f^-, \lambda^+, \lambda^-\} \tag{5.6}$$

$$L = \prod_{i=1}^{N} \mathcal{F}^i_{lik}(\vec{\alpha}) \tag{5.7}$$

In practice, one actually minimizes the negative ln-likelihood:

$$\mathcal{L} = -2 \ln \prod_{i=1}^{N} \mathcal{F}^i_{lik}(\vec{\alpha}) = -2 \sum_{i=1}^{N} \ln \mathcal{F}^i_{lik}(\vec{\alpha}) \tag{5.8}$$

The minimization is done using the MINUIT package [53].

We add to $-\ln \mathcal{F}_{lik}$ the following "gaussian constraint" term:

$$\left(\frac{f_B - \hat{f_B}}{\sigma_{f_B}} \right)^2 \tag{5.9}$$

Where $\hat{f_B}$ and σ_{f_B} are determined by fitting a histogram of only the mass distribution to a gaussian plus linear background. This term constrains f_B to within its errors, determined in the mass histogram fit.

5.2.2 Method Two - The Two Dimensional Simultaneous Mass and Lifetime Fit

The second method is a two dimensional fit in mass and lifetime. We use this method as a cross-check of the results from the first method. We simultaneously fit for the mass distribution shape and the lifetime distribution shape. We use same the functional forms for the lifetime of the signal and background as in the separate fit. We do not exclude data between 3 and $6\sigma_m$ in the invariant mass distribution. This data is required to fit for a mass distribution shape.

The PDF for the signal mass distribution is a gaussian:

$$M^i_{sig} = \frac{1}{\sqrt{2\pi}\sigma_{m_B}} \cdot exp\left\{-\frac{(m^i - m_B)^2}{2\sigma^2_{m_B}}\right\} \tag{5.10}$$

where m_B and σ_{m_B} are the Λ_B or B^0 mass and width.

The mass background (sidebands) are fit to a first order polynomial, which normally has two free parameters. Due to the normalization condition here, it has only one (C_0).

The mass background function is given by

$$M^{bgr} = \left(\frac{2}{M^2_{max} - M^2_{min}} - \frac{2C_0}{M_{max} + M_{min}}\right) \cdot m^i + C_0 \tag{5.11}$$

where M_{max} and M_{min} are the maximum and minimum masses included in the fit. These are the same as in the mass histogram fit of Method 1.

The full PDF for the 2-d simultaneous mass and lifetime fit is

$$\mathcal{F}^i_{lik} = (1 - f_B) \cdot F^i_{sig} \cdot M^i_{sig} + f_B \cdot F^i_{bgr} \cdot M^i_{bgr} \tag{5.12}$$

Here, f_B is a free parameter in the fit with no gaussian constraint. F^i_{sig} and F^i_{bgr} are the same as in Method 1, and are given in equations 5.2 and 5.4.

The free parameters are

$$\vec{\alpha} = \{c\tau, s_{ct}, f_B, f^+, f^-, \lambda^+, \lambda^-, m_B, \sigma_{m_B}, C_0\} \tag{5.13}$$

We obtain the free parameters which give the maximum likelihood by minimizing equation 5.8

5.2.3 Improvement on Method 2

In addition to the above, we try an additional fitting method as a cross check. This is a small perturbation to the 2d simultaneous mass and lifetime fit. Instead of fitting for σ_{m_B}, the fitter is given an additional input - the error on the mass for each event. Then, we fit for a mass-error scale factor instead of directly for the width. In this case the signal region mass distribution has the following PDF:

$$M^i_{sig} = \frac{1}{\sqrt{2\pi}\sigma_{m_B}} \cdot exp\left\{-\frac{(m^i - m_B)^2}{2(s_M\sigma^i_m)^2}\right\} \tag{5.14}$$

The advantage of this method is that an event near the mean mass, with a small error on the mass will have more weight in the fit as signal than an event with the

same mass value, but a large error. We have chosen to use this method only as a cross-check, because we observe a run-dependent mass resolution. The width of the B^0 mass distribution is larger in later runs than in earlier runs. The mass pull distributions have a larger width in later runs than in earlier runs. This means that in later runs, the mass errors are underestimated. The fit described above assumes uniform underestimation or overestimation of errors, taken into account by one scale factor. The run dependence is discussed in Section A.2.

5.3 Tracking Algorithm

CDF currently has two algorithms which perform COT tracking. The first algorithm, Segment Linking (SL) is very similar to the Run I tracking algorithm which is described in detail in Reference [47]. This method links full segments at the pattern recognition stage. The second algorithm, Histogram Linking (HL) is a supplemental algorithm intended to add tracks that SL failed to find. Hits added to the track are not required to be part of a complete segment. This algorithm is most efficient for primary tracks because the search road is constrained to point to the beam spot, thus assuming a track with negligible impact parameter. The implementation and performance of this algorithm are described in [48].

During the axial pattern recognition stage of COT tracking, both algorithms are run. The final set of COT tracks is a merged set of both HL and SL tracks. We show in Section A.1 that the use of HL tracks causes a bias in the B^0 control sample lifetime. To measure the Λ_B lifetime, we use a sample where the COT tracking has been rerun using only the SL algorithm. Since SVX tracking proceeds by adding hits

to COT tracks, the SVX tracking has also been rerun.

5.4 Results

In this section, we describe results obtained obtained in two ways.

The first method, which we use for the measurement of the Λ_B lifetime, is the separate mass and lifetime fit. The second method, which we use as a cross-check, is the 2-d simultaneous mass and lifetime fit. We use only the sample that has had tracking rerun with SL-only COT tracking.

5.4.1 Separate Mass and Lifetime Fit

For the results presented here, we use the separate fit. We obtain 205 $\pm$ 28 B^0 candidates, and 52 $\pm$ 15 Λ_B candidates, with background fractions of $f_B(B^0) = 0.642 \pm 0.048$ and $f_B(\Lambda_B) = 0.726 \pm 0.079$. The plots of invariant mass are shown in Figure 5.4. These are the same plots as shown in Section 4.4, which describes our event selection. We include them again here for convenience.

For the control sample, we obtain $c\tau(B^0) = 414 \pm 31 \mu$m(stat.). This is acceptable, since it is within 1.6 σ of the current world-average B^0 lifetime of 462μm.

For the Λ_B, we measure $c\tau(\Lambda_B) = 374 \pm 78 \mu$m)(stat.). The fits to the data for B^0 and Λ_B are shown in Figure 5.5 and Figure 5.6. A summary of the fit parameters and their errors are shown in Tables 5.1 and 5.2. If we count the number of events in the signal region, and then multiply by $(1 - f_B)$, where f_B is the value obtained from the lifetime fit, we obtain 246 $\pm$ 16 B^0 candidates, and 46 $\pm$ 9 Λ_B candidates.

In both lifetime fits, we obtain values of the scale factor s_{ct} which are larger than

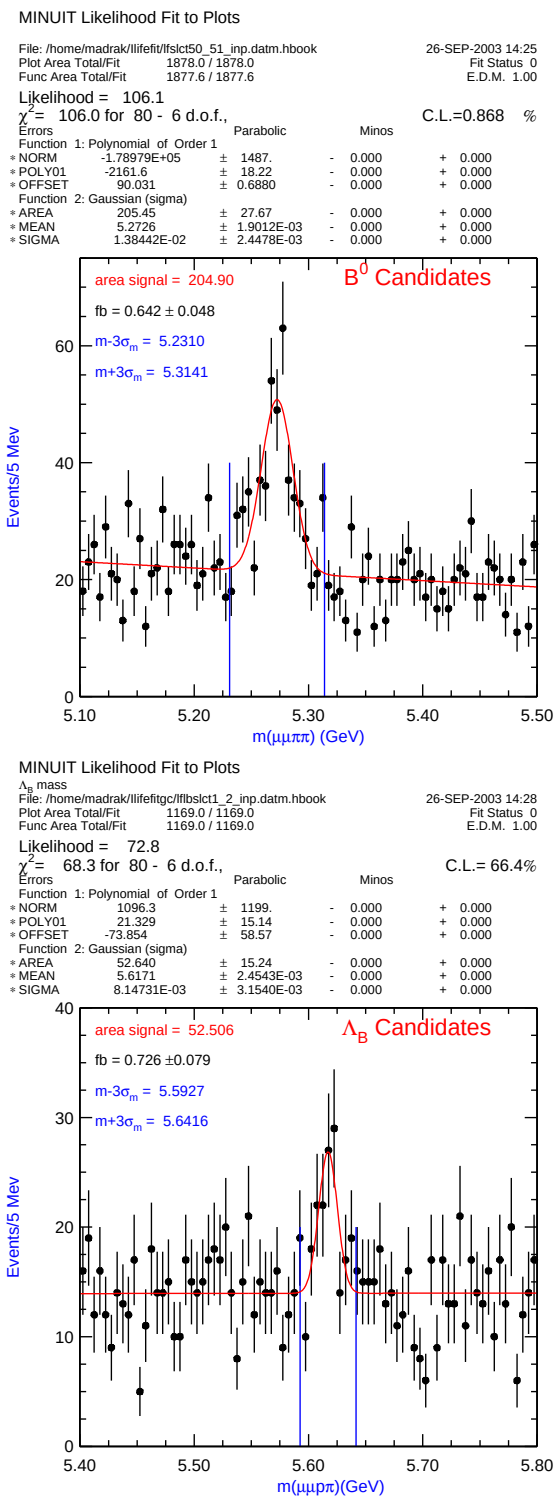

Figure 5.4: B^0(top) and Λ_B(bottom) candidates in the SL-only sample

one: 1.26±0.05 for the B^0 and 1.27 ± 0.04 for the Λ_B. This indicates that the errors on the proper decay length are underestimated.

Parameter	Units	Value	parabolic error	negative error (MINOS)	positive error (MINOS)
$c\tau$	(μm)	414.2	31.2	29.8	32.8
s_{ct}		1.263	0.050	0.050	0.050
f_-		0.029	0.0094	0.0084	0.010
λ_-	(μm)	499.3	138.5	114.6	173.0
f_+		0.13	0.020	0.019	0.020
λ_+	(μm)	307.2	43.0	38.9	48.0
f_B		0.571	0.0276	0.0274	0.0276

Table 5.1: Fit parameter values obtained in the separate mass and lifetime fit for B^0.

Parameter	Units	Value	parabolic error	negative error (MINOS)	positive error (MINOS)
$c\tau$	(μm)	374.0	78.1	72.1	87.3
s_{ct}		1.268	0.044	0.043	0.045
f_-		0.027	0.0080	0.0072	0.0090
λ_-	(μm)	446.4	115.5	97.5	140.9
f_+		0.17	0.017	0.017	0.018
λ_+	(μm)	377.0	36.4	34.1	39.0
f_B		0.758	0.0458	0.0462	0.0453

Table 5.2: Fit parameter values obtained in the separate mass and lifetime fit for Λ_B.

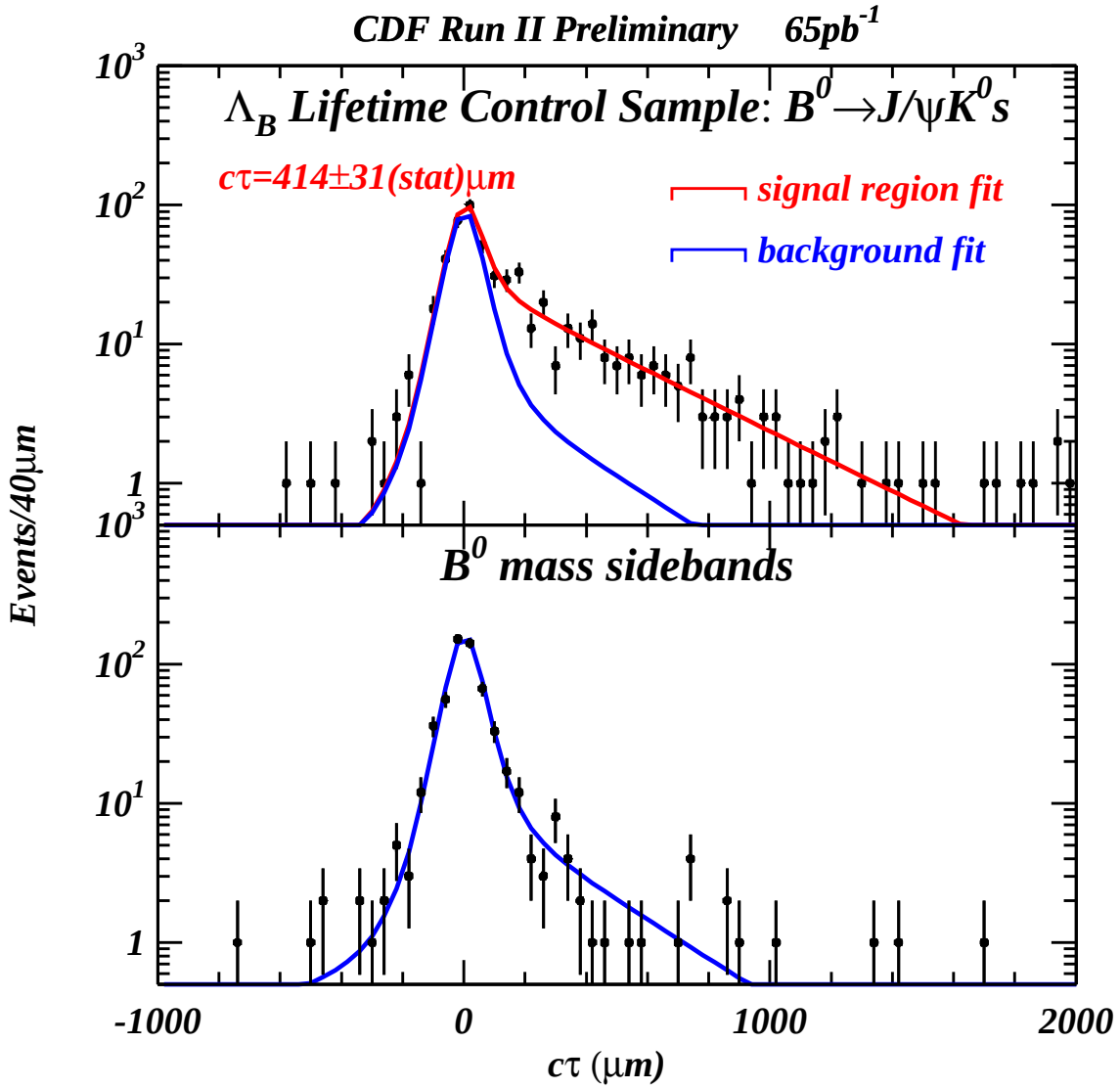

Figure 5.5: Separate lifetime fit with gaussian constraint on f_B, for B^0. The upper histogram shows data in the signal region, with the signal plus background fit overlaid, and the projected background fit overlaid(the line with darker shading). The lower histogram shows data from the sidebands, with the background fit overlaid. We show only the regions -1000μm $< ct <$ 2000μm, though all data is included in the fit.

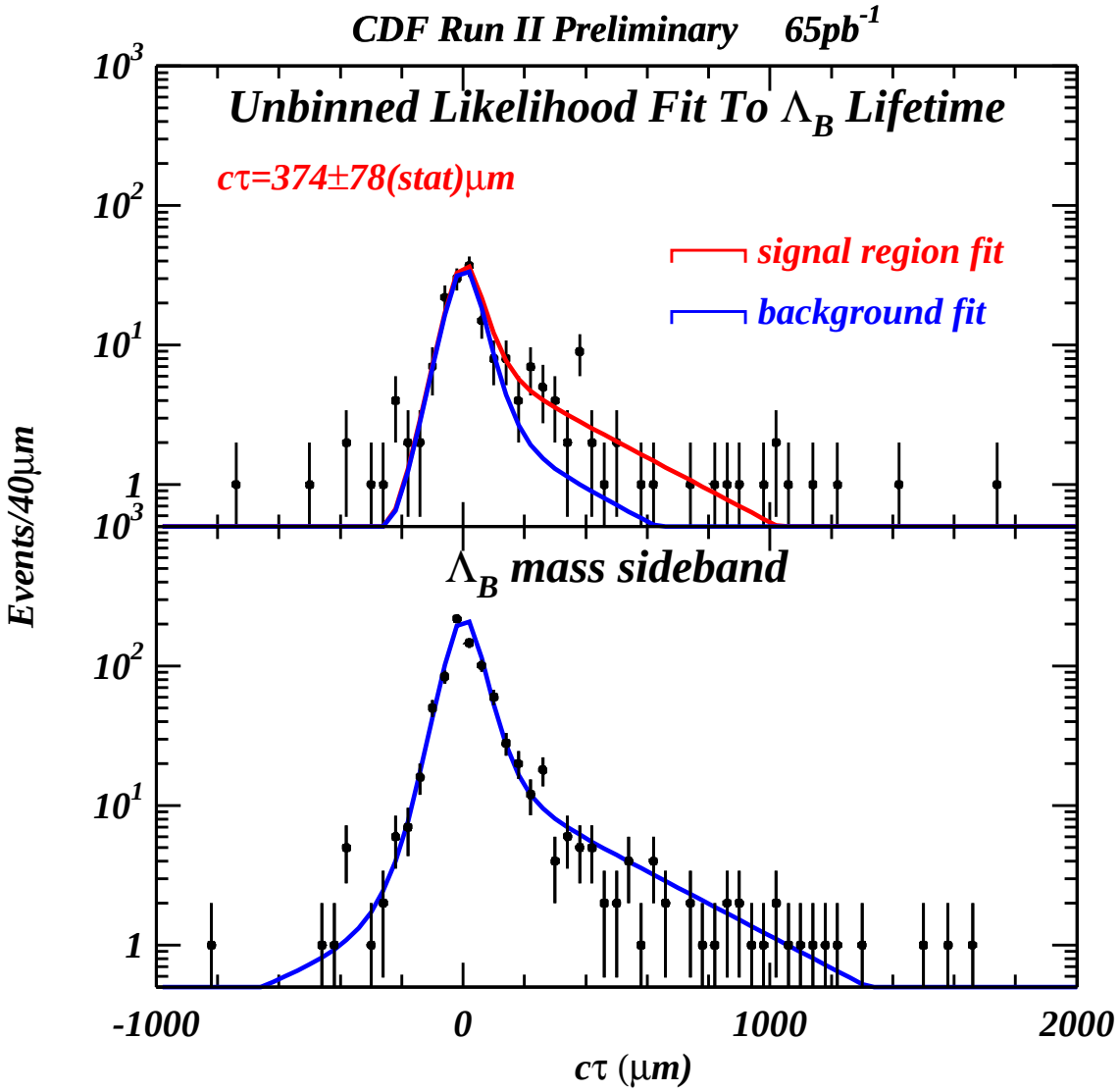

Figure 5.6: Separate lifetime fit with gaussian constraint, for Λ_B. The upper histogram shows data in the signal region, with the signal plus background fit overlaid, and the projected background fit overlaid(the line with darker shading). The lower histogram shows data from the sidebands, with the background fit overlaid. We show only the regions -1000μm $< ct <$ 2000μm, though all data is included in the fit.

5.4.2 2-d Simultaneous Mass and Lifetime Fit

Results from the second fitting method, the 2-d simultaneous mass and lifetime fit, are shown in Figure 5.7 and Figure 5.8. We use this fit as a cross-check. Fit parameters and their errors are shown in 5.3 and 5.4. For $c\tau(B^0)$, we obtain 420±32μm. This is 6 μm larger than our result with the standard method (Method 1). For the Λ_B, we obtain $c\tau = 351 \pm 69\mu$m. This is 23 μm smaller than the result using our standard method.

Parameter	Units	Value	parabolic error	negative error (MINOS)	positive error (MINOS)
$c\tau$	(μm)	420.3	32.1	30.6	33.8
s_{ct}		1.228	0.038	0.038	0.038
f_-		0.023	0.006	0.006	0.007
λ_-	(μm)	541.4	131.6	111.7	158.9
f_+		0.16	0.017	0.017	0.017
λ_+	(μm)	324.9	30.8	29.2	32.7
f_B		0.850	0.0137	0.0140	0.0134
m_B	(GeV)	5.274	0.0012	0.0012	0.0012
σ_{m_B}	(GeV)	0.0130	0.0017	0.0016	0.0018
C_0	$(\text{GeV})^{-1}$	14.6	5.3	5.3	5.2

Table 5.3: Fit parameter values obtained in the 2-d simultaneous mass and lifetime fit for the B^0.

Parameter	Units	Value	parabolic error	negative error (MINOS)	positive error (MINOS)
$c\tau$	(μm)	350.7	68.8	63.8	75.9
s_{ct}		1.264	0.0402	0.0397	0.0408
f_-		0.022	0.007	0.006	0.007
λ_-	(μm)	462.9	120.9	101.9	147.3
f_+		0.17	0.016	0.016	0.016
λ_+	(μm)	376.5	34.3	32.3	36.7
f_B		0.958	0.0084	0.0088	0.0080
m_B	(GeV)	5.617	0.0020	0.0020	0.0021
σ_{m_B}	(GeV)	0.0090	0.0018	0.0016	0.0019
C_0	$(\text{GeV})^{-1}$	3.3	3.7	3.6	3.6

Table 5.4: Fit parameter values obtained in the 2-d simultaneous mass and lifetime fit for the Λ_B.

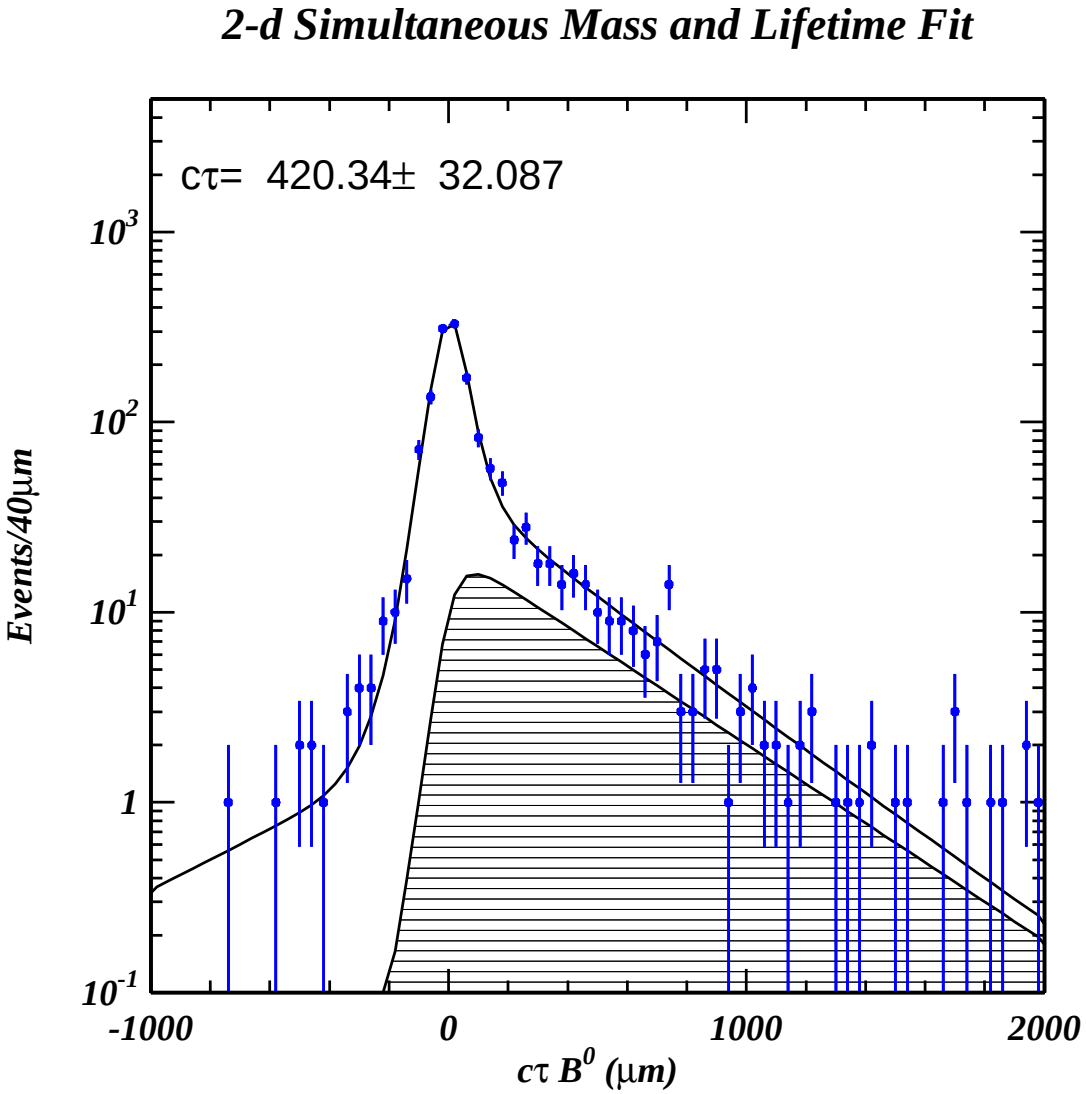

Figure 5.7: Lifetime projection of 2-d simultaneous mass and lifetime fit for B^0. The histogram shows the data in both the signal and background regions. The solid line shows the combined signal and background lifetime part of the fit to the data. The shaded region shows the signal lifetime fit.

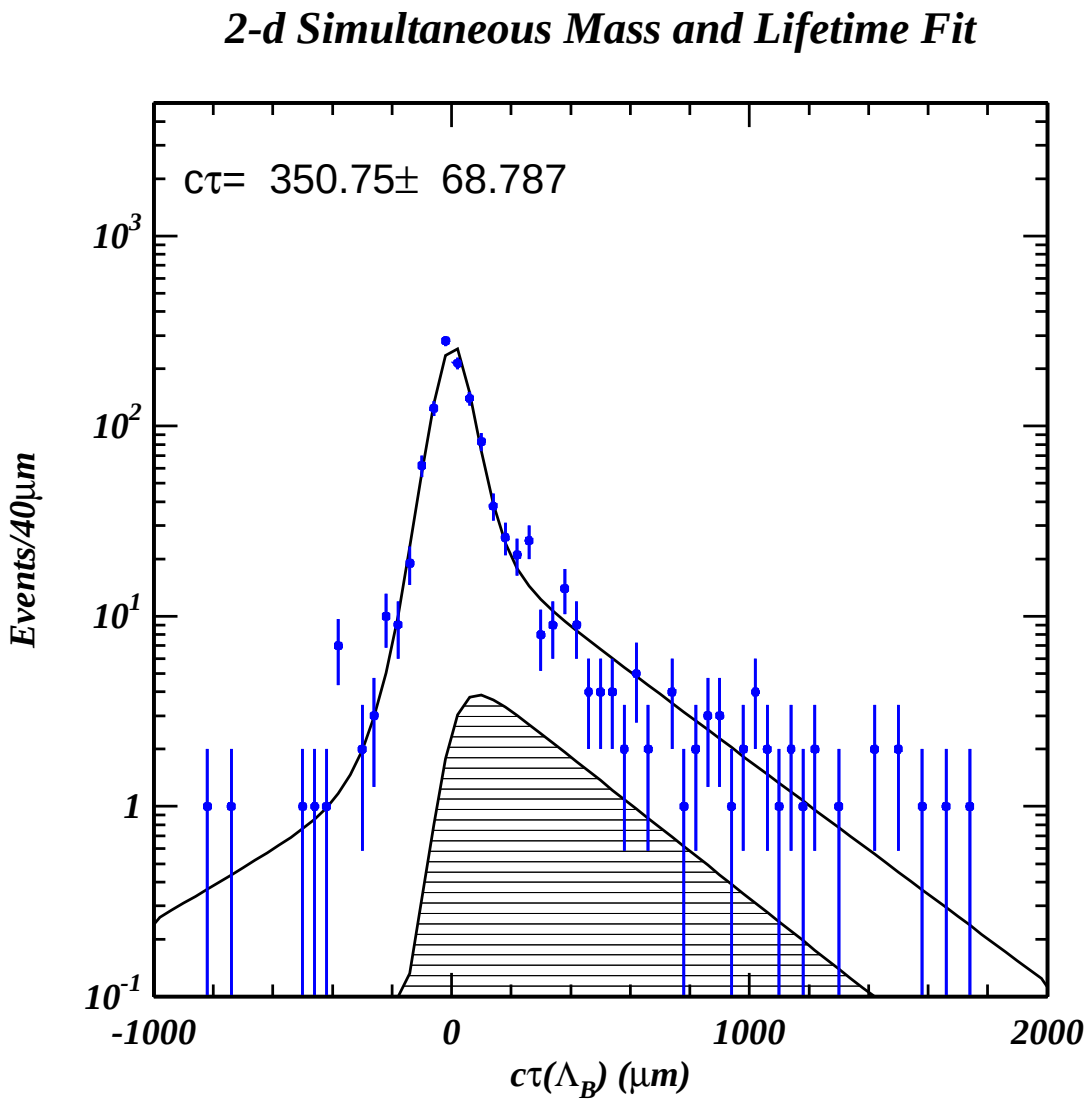

Figure 5.8: Lifetime projection of 2-d simultaneous mass and lifetime fit for Λ_B. The histogram shows the data in both the signal and background regions. The solid line shows the combined signal and background lifetime part of the fit to the data. The shaded region shows the signal lifetime fit.

5.5 Fitting Method Validation and Goodness of Fit Tests

5.5.1 Toy Monte Carlo

We test our lifetime fitting method to insure that there are no programming bugs or fitting biases. In our first test, we use a Toy Monte Carlo. We generate 5000 experiments containing signal and background. Each of these has the same number of signal and background events as the data, within Poisson statistics.

Values of the proper decay length ct are randomly drawn from a distribution which has the same functional form that we fit in the data. The errors σ_{ct} are selected randomly from a histogram of the errors in the data.

To show that the fitting method passes this test, the average $c\tau$ obtained in the 5000 experiments must be within the statistical error of the generated $c\tau$. The pull distribution of

$$\left(c\tau_{\text{generated}} - c\tau^{i}_{\text{fit}}\right)/\sigma^{i}_{c\tau}$$

should have a width of one. This indicates that the error returned by the fit is correct.

Figure 5.9 shows the distribution of fit values of $c\tau$, as well pulls, for B^0 and Λ_B. A gaussian fit to the distribution of fit B^0 $c\tau$ results in a mean of 413 $\pm$ 0.5μm. The mean value used for the generation was 414μm. A gaussian fit to the distribution of fit Λ_B $c\tau$ results in a mean of 373 $\pm$ 1μm. In this case the mean value used for the generation was 374μm. In both cases, the width of the $c\tau$ pull distributions is very close to one - 1.05 $\pm$0.02 for the B^0, and 0.96 $\pm$ 0.02 for the Λ_B.

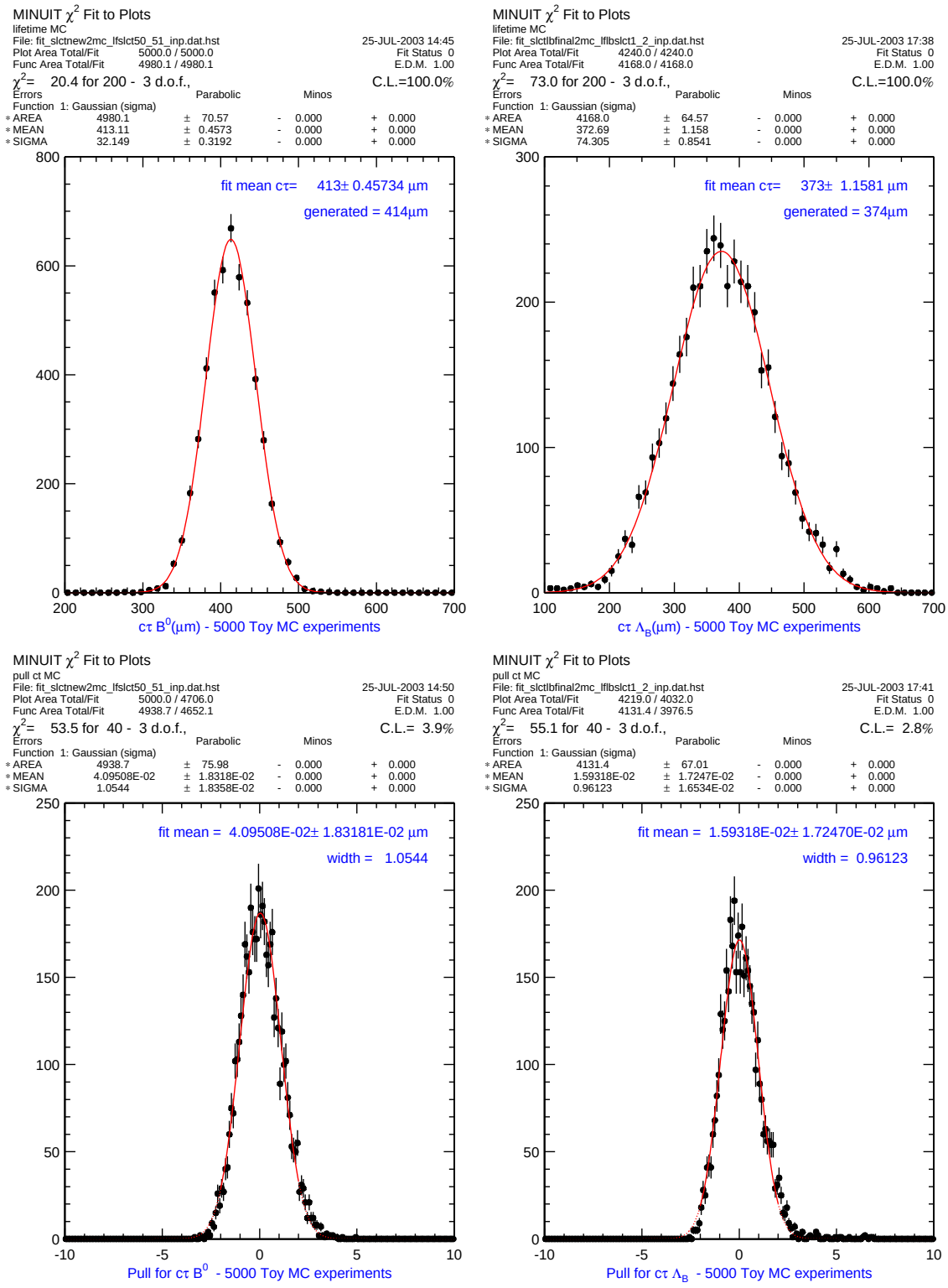

Figure 5.9: Results for lifetime fits to 5000 toy Monte Carlo experiments. The top two plots show the distributions of fitted lifetime for B^0 and Λ_B. The bottom two plots show the pull on the lifetime.

5.5.2 Full Monte Carlo with Detector Simulation

In addition to the toy Monte Carlo test of the fitting method, we have run a full Monte Carlo simulation for $B^0 \to J/\psi K_s^0$. The event generation is done using `Bgenerator` [41], and the detector simulation using `CdfSim` [43].

In this case, we do not simulate 5000 experiments. Instead, we simulate one background free experiment with approximately 3000 B^0 decays. Since there is no background, we fit only for the signal region parameters. Using the same reconstruction code and fitting code that we use on the data, we obtain $c\tau(B^0) = 484 \pm 6\mu$m. The generated value was 486μm. The fit to the lifetime distribution is shown in Figure 5.10.

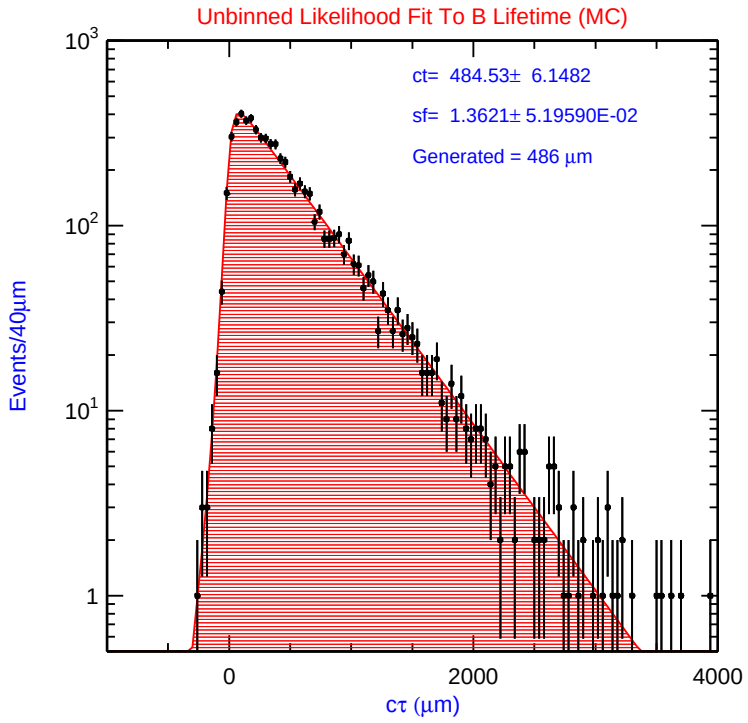

Figure 5.10: Fit to B^0 lifetime from realistic Monte Carlo

5.5.3 Goodness of Fit

We use two tests for Goodness of Fit. In the first test, we compare the value of the log-likelihood from the data fit to the values obtained in the toy Monte Carlo experiments. For B^0 and Λ_B the data values fall approximately in the center of the distributions of the toy Monte Carlo values. This is shown in Figure 5.11. We conclude that this test is satisfactory. Figure 5.11 also shows scans of the likelihood functions for the data, around the minimum.

Next, we use a χ^2 test. We bin our data and fit in histograms with variable bin sizes, to insure that no bin contains less than 20 entries. The histograms are shown in Figure 5.12 and Figure 5.13 for various ranges. For the B^0 lifetime fit we obtain a χ^2 probability of 3%. For the Λ_B fit we obtain 1.2%.

The fit parameter correlation coefficients for the fits to the B^0 and Λ_B data are shown in tables 5.5 and 5.6. The parameters which are most correlated with $c\tau$ are f_B and λ^+.

	$c\tau$	s_{ct}	f_-	λ_-	f_+	λ_+	f_B
$c\tau$	1.000	-0.004	-0.018	-0.001	0.146	-0.231	0.286
s_{ct}	-0.004	1.000	-0.482	0.400	-0.191	0.121	0.009
f_-	-0.018	-0.482	1.000	-0.563	0.079	-0.079	-0.041
λ_-	-0.001	0.400	-0.563	1.000	-0.104	0.071	0.006
f_+	0.146	-0.191	0.079	-0.104	1.000	-0.398	0.316
λ_+	-0.231	0.121	-0.079	0.071	-0.398	1.000	-0.086
f_B	0.286	0.009	-0.041	0.006	0.316	-0.086	1.000

Table 5.5: Parameter correlation coefficients for the B^0 lifetime fit.

	$c\tau$	s_{ct}	f_-	λ_-	f_+	λ_+	f_B
$c\tau$	1.000	-0.011	-0.004	-0.004	0.050	-0.200	0.240
s_{ct}	-0.011	1.000	-0.330	0.253	-0.233	0.149	-0.014
f_-	-0.004	-0.330	1.000	-0.497	0.064	-0.073	-0.015
λ_-	-0.004	0.253	-0.497	1.000	-0.087	0.060	-0.005
f_+	0.050	-0.233	0.064	-0.087	1.000	-0.339	0.205
λ_+	-0.200	0.149	-0.073	0.060	-0.339	1.000	-0.056
f_B	0.240	-0.014	-0.015	-0.005	0.205	-0.056	1.000

Table 5.6: Parameter correlation coefficients for the Λ_B lifetime fit.

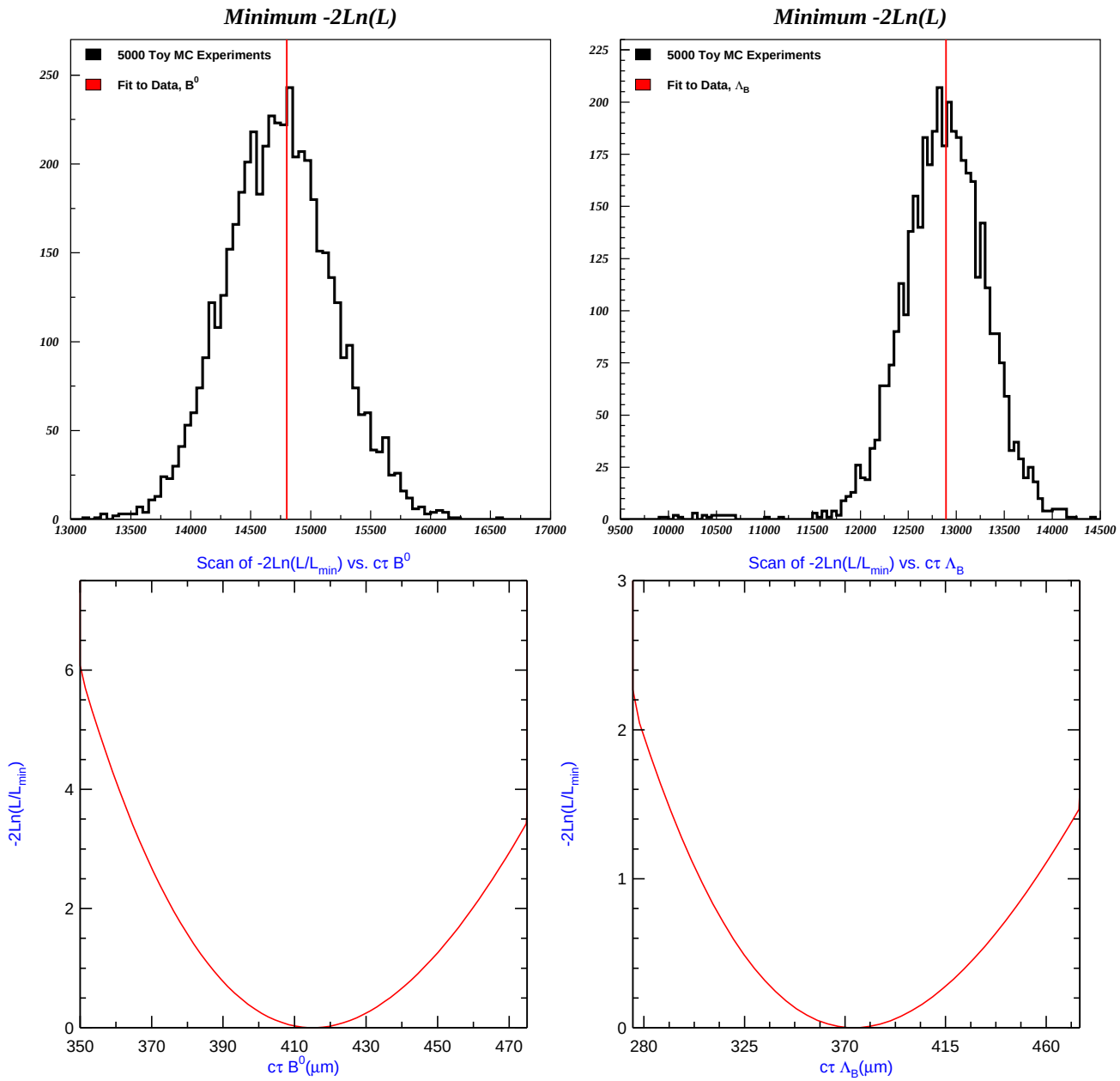

Figure 5.11: Top: Comparison of the minimum value of Ln Likelihood obtained from the fit to the data, and in toy Monte Carlo experiments, for $B^0$and Λ_B. Bottom: Scan of the likelihood function around the minimum for the fit to the data.

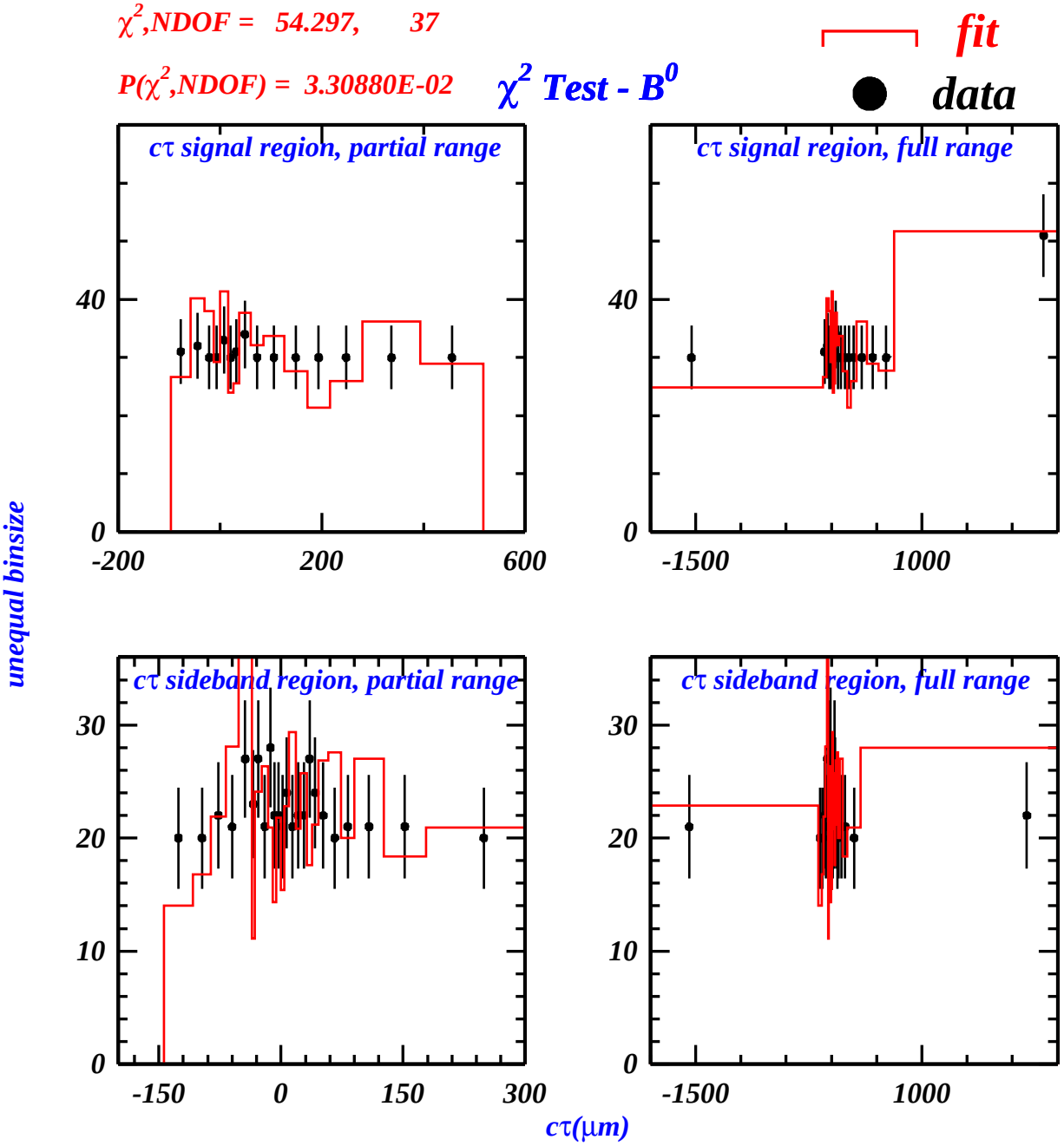

Figure 5.12: χ^2 test for Goodness of Fit, for the B^0 lifetime. The data shown here are from the final sample. The data are the points with error bars, and the fit is shown in the overlaid histogram. We have varied the binsize so that each bin contains at least 20 events. The top plots show the signal region, and the bottom show the sideband region. Plots on the left show a subset of the entire range, and plots on the right show the entire range.

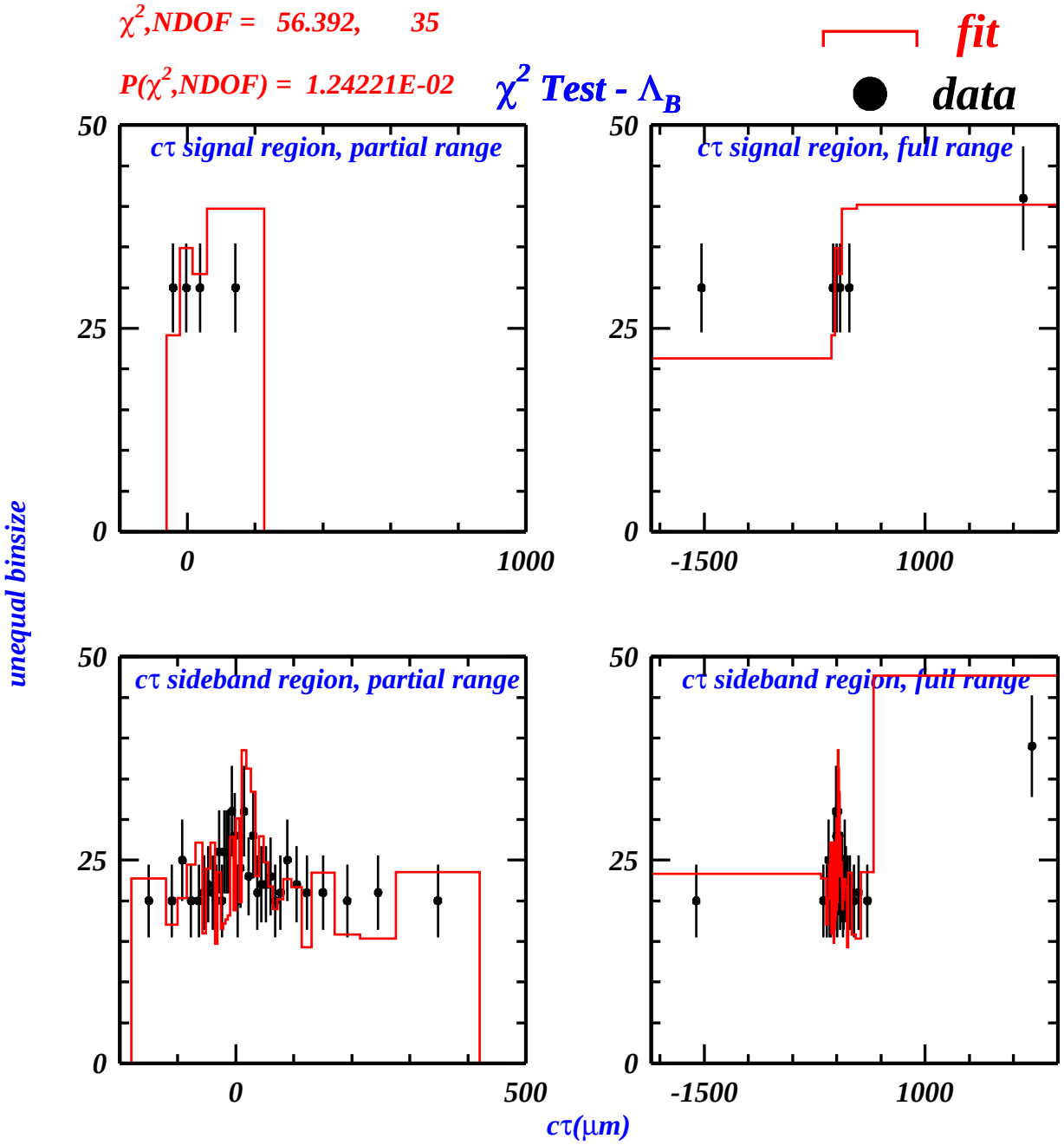

Figure 5.13: χ^2 test for Goodness of Fit, for the Λ_B lifetime. The data are the points with error bars, and the fit is shown in the overlaid histogram. We have varied the binsize so that each bin contains at least 20 events. The top plots show the signal region, and the bottom show the sideband region. Plots on the left show a subset of the entire range, and plots on the right show the entire range.

5.6 Ratio of Lifetimes

For comparisons with theoretical predictions, the quantity of interest is the ratio $\tau(\Lambda_B)/\tau(B^0)$. With $c\tau(\Lambda_B) = 374 \pm 89\mu$m (this includes the systematic error which is discussed in the next chapter), and $c\tau(B^0) = 462 \pm 5\mu$m (from the PDG) [56], we obtain

$$\frac{\tau(\Lambda_B)}{\tau(B^0)} = 0.810 \pm 0.193 \tag{5.15}$$

The central value is consistent with the theoretical prediction of 0.9 to 1.0. It is also in agreement with the world average experimental number from semileptonic modes: 0.797 ± 0.052. More data is needed to test the agreement between theory and experiment in this mode alone.

This measurement was done with 65 pb^{-1} of data. We have used toy Monte Carlo to predict the error on the Λ_B lifetime and on the lifetime ratio with the inclusion of more data. The toy Monte Carlo is as described in Section 5.5.1. We set f_B, the ratio of the number of signal to background events in the signal region, to the current value for Λ_B: 0.726.

We assume no error on f_B. With the data presented in this thesis, the statistical error on the Λ_B lifetime is 78μm. If we assume no error on f_B, the statistical error on the Λ_B lifetime is 70μm. In the case of the B^0, we have approximately four times as many signal events. The statistical error on the B^0 lifetime is the same whether we use the current value for σ_{f_B} or set it to zero. Thus, we expect the predicted error on the Λ_B lifetime to be slightly underestimated, until the number of signal events is a factor of four larger than the currrent number.

We show predictions for three scenarios:

1. Statistical error only

2. Statistical error, plus a systematic error of 20μm

3. Statistical error, plus a systematic error of 5μm

The systematic errors on this measurement are described in Chapter 6. A total systematic error of 20μm would have been a reasonable result. It is larger due to to tracking uncertainties. This will hopefully be eliminated once the CDF tracking is better understood and more mature. We also show results for a systematic of 5μm. We choose this because it is close to the current systematic error of 6μm assigned to the measurement of the B_s lifetime in the decay mode $B_s \to J/\psi\phi$ [44].

Figure 5.14 shows predictions for the errors on the Λ_B lifetime and the ratio of the Λ_B to the B^0 lifetime. For a 10% error on the ratio of lifetimes, we need ~ 2 to 2.5 times as much data as used in this thesis. This would make the measurement interesting, since the theoretical prediction for the ratio of lifetimes extends down to 90%.

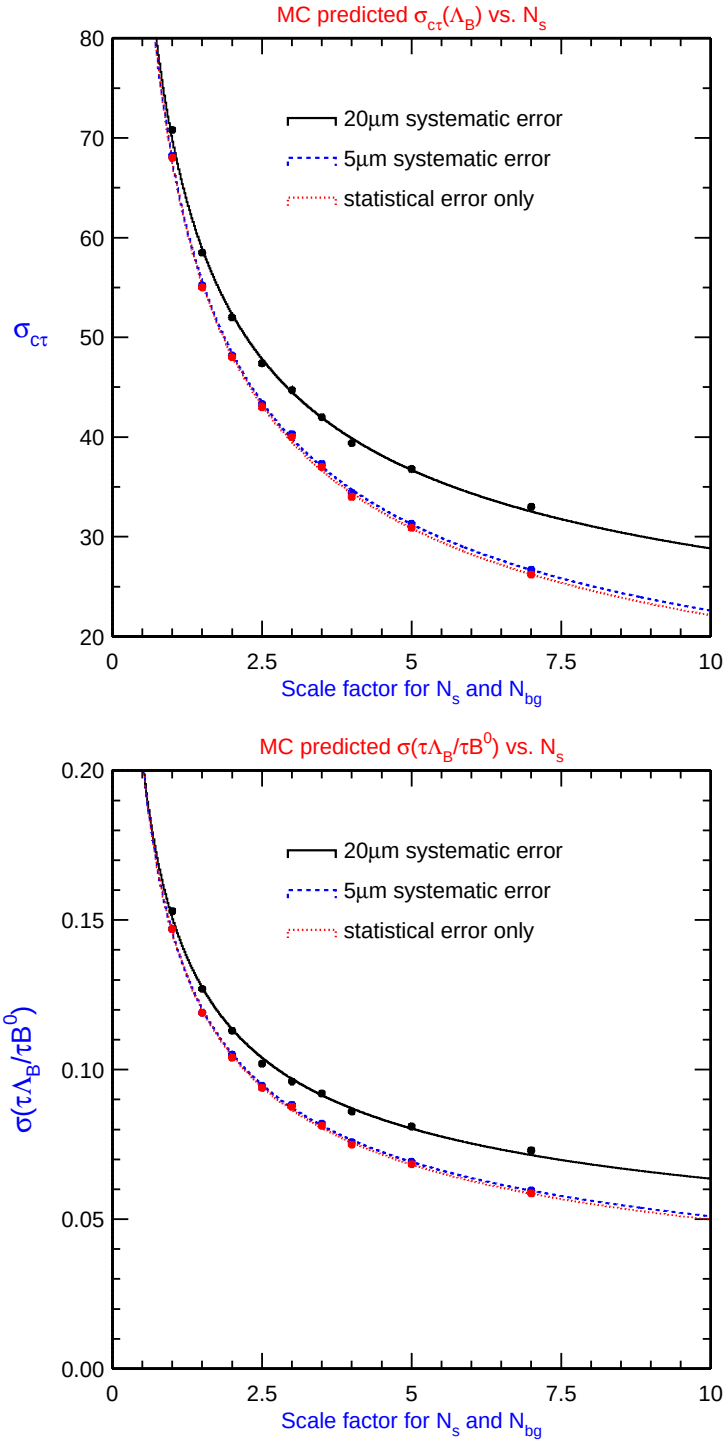

Figure 5.14: Predictions by toy Monte Carlo for error on Λ_B lifetime (top) and ratio of Λ_B to B^0 lifetime (bottom). The x-axis is a scale factor to multiply by the current statistics. We show the results for a statistical error only, and for 20μm and 5μm sytstematic errors.

Chapter 6

Systematic Errors and Cross-Checks

6.1 Overview

In this chapter, we evaluate systematic errors in the measurement of the Λ_B lifetime, and perform a series of cross-checks.

The systematic errors are are due to

1. ct resolution
2. choice of fitting model
3. tracking chamber occupancy, and its effect on the mass resolution
4. tracking bias for long-lived particles

To check that our requirements on $L_{xy}(V_0)$ and $p_T(B)$ do not cause any bias, we vary the values required, and repeat the fit for $c\tau$.

The systematic errors discussed in the following sections are summarized in Table 6.8.

6.2 Resolution Function

We use only the J/ψ vertex in our determination of the decay point of the Λ_B. This is in contrast to, for instance, the three track vertex of $B^+ \to J/\psi K^+$. Because we use only the J/ψ we can make use of other studies which have been done using the higher-statistics sample of inclusive J/ψ 's. These studies do not require reconstruction of a B.

The dependence of the scale factor for the $L_{xy}(J/\psi)$ resolution, s_{ct}, on $p_T(J/\psi)$ has been measured in CDF Internal Note 6272: *Optimization of Silicon Track Selection for Run II B-Fraction Measurement* [57]. The scale factors are extracted by fitting gaussians to the cores of the distributions of $L_{xy}/\sigma_{L_{xy}}$ for different ranges in $p_T(J/\psi)$. The measured values are shown in Figure 6.1. No errors are given. Had all of the track parameter errors been correct, the scale factor would have been 1.0, and independent of $p_T(J/\psi)$.

Our fit to the B^0 lifetime yields a scale factor s_{ct} of 1.26±0.05. This is larger than any of those measured in [57]. We quantify any bias on our lifetime measurement due to this difference by forcing our scale factor to agree with those obtained in [57]. We fit the following function to the values obtained in [57]:

$$\begin{cases} 0.94966 + 0.03085 * (p_T(J/\psi) - 2.8637) & p_T(J/\psi) < 9 \\ 1.075 & 9 \leq p_T(J/\psi) \leq 10 \\ 1.036 & p_T(J/\psi) > 10 \end{cases}$$

We scale each of our errors on σ_{ct} according to this function, and then perform the lifetime fit fixing the scale factor to 1.0. We obtain $c\tau = 415 \pm 31\mu$m, and assign the 1μm difference as a systematic error.

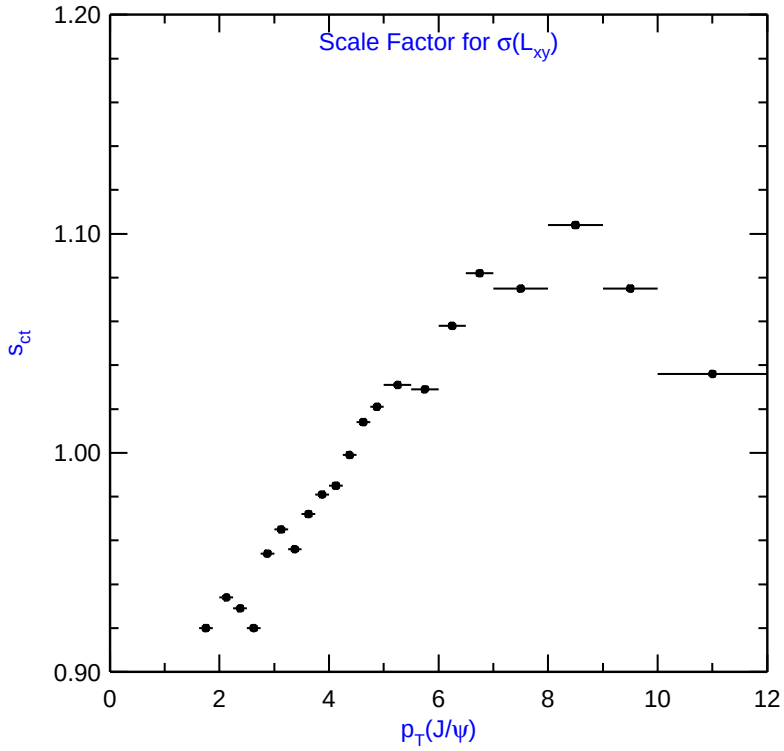

Figure 6.1: Scale Factors measured in [57] as a function of $p_T(J/\psi)$.

6.3 Fitting Model

The tails in the lifetime distribution are the result of both tails in the resolution function and long-lived background. In our lifetime fit, we take these into account using two exponentials: one positive going and one negative going. They are added to the gaussian resolution function which represents prompt background smeared by detector resolution.

Other models may be used, and there is no definite answer as to which is correct. We evaluate sources of systematic error due to the choice of fitting model by trying other well-motivated models, and measuring the change in the fitted B^0 lifetime.

In our first alternative fitting model, we convolute the exponential tails in the background with the gaussian resolution function, as opposed to simply adding them. We obtain $c\tau(B^0) = 403 \pm 30\mu$m, which is 11μm lower than our standard value.

In the second alternative fitting model, we add an additional positive going exponential to the background fit. This results in no change in the B^0 lifetime.

We also fit the data using a modified version of the simultaneous mass and lifetime fitter, which takes into account the errors on the mass per event. The parameter s_M, a scale factor for the errors on the mass, replaces the width of the mass peak. The likelihood function for this model is fully described in Section 5.2.3. Using this model, the B^0 lifetime is $436 \pm 34\mu$m, 22μm higher higher than our central value.

In our standard fitting method we fit the signal regions and sidebands simultaneously. As a final check, we fit in two steps. We first fit the sidebands only. The sidebands contain no signal, so we fit for only the parameters of the background function. Then, we do the full fit, constraining the background functions to those

obtained in the sideband only fit. We expect the lifetime here to be similar to our central value, because most of the information on the background comes from the sidebands. We obtain a result which is 2μm lower than our standard value.

The largest variation seen in the studies described is 22μm, which we assign as a systematic error.

6.4 Cross Check on Selection Requirements

To check that our requirements of $L_{xy}(K_s^0) > 0.25$ cm and $p_T(B^0) > 4.5$ GeV do not bias the lifetime, we vary the values used for these requirements. The results are shown in Tables 6.1 and 6.2. We fit these data to a straight line. The fits are shown in Figure 6.2. The slopes of the lines are consistent with zero. We also divide the full sample into four separate samples, based on $p_T(B^0)$ and $L_{xy}(K_s^0)$. We measure the lifetime in each bin. The results are shown in Tables 6.3 and 6.4. The lifetime shows no dependence on $p_T(B^0)$ or $L_{xy}(K_s^0)$. We assign no systematic error.

$p_T(B^0)$ requirement (GeV)	$c\tau$ (μm)
2.0	358 ± 29
3.0	380 ± 29
4.0	409 ± 30
4.5	414 ± 31
5.0	389 ± 29
6.0	389 ± 31
7.0	415 ± 37
8.0	397 ± 37
9.0	392 ± 37
10.0	427 ± 48

Table 6.1: B^0 lifetime with various requirements on $p_T(B^0)$.

$L_{xy}(K_s^0)$ requirement (cm)	$c\tau(B^0)(\mu$m)
0.25	414 ± 31
1.0	417 ± 32
5.0	404 ± 35
7.0	409 ± 38
10.0	393 ± 31
11.0	389 ± 43
13.0	416 ± 47
15.0	431 ± 52
20.0	459 ± 66
25.0	410 ± 71

Table 6.2: B^0 lifetime with various requirements on $L_{xy}(K_s^0)$.

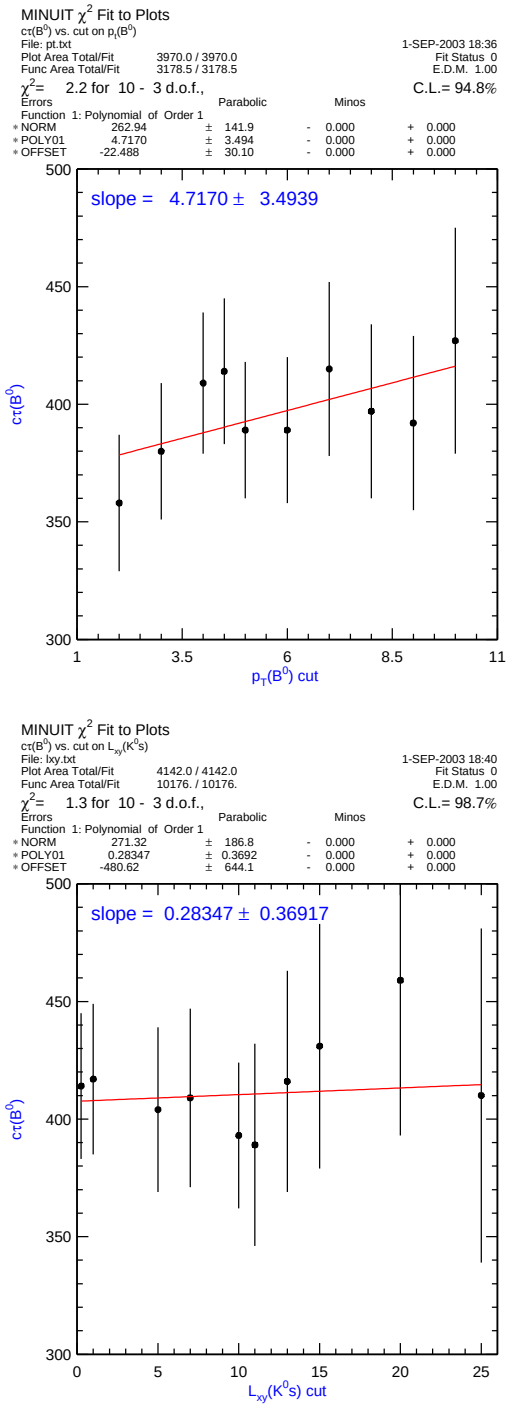

Figure 6.2: Measured B^0 lifetime for different requirements on $p_T(B^0)$ and $L_{xy}(K^0_s)$. We fit the data to a straight line. In both cases the slopes are consistent with zero.

$p_T(B^0)$ requirement (GeV)	$c\tau(\mu\text{m})$
$4.5 < p_T(B^0) < 8.5$	406 ± 50
$8.5 < p_T(B^0) < 10.5$	520 ± 89
$10.5 < p_T(B^0) < 13.5$	378 ± 62
$p_T(B^0) > 13.5$	313 ± 63
standard requirement = 4.5 GeV	

Table 6.3: B^0 lifetime in 4 bins of $p_T(B^0)$.

$L_{xy}(K^0_s)$ requirement (cm)	$c\tau(\mu\text{m})$
$0.25 < L_{xy} < 7.0$	416 ± 55
$7.0 < L_{xy} < 11.0$	467 ± 86
$11.0 < L_{xy} < 20.0$	301 ± 53
$L_{xy} > 20.0$	459 ± 66
standard requirement = 0.25cm	

Table 6.4: B^0 lifetime in 4 bins of $L_{xy}(K^0_s)$.

$L_{xy}(K^0_s)$ requirement (cm)	This Analysis $c\tau(\mu$m)	COT only for K^0_s $c\tau(\mu$m)
$0.25 < L_{xy} < 7.0$	416 ± 55	286 ± 55
$7.0 < L_{xy} < 11.0$	467 ± 86	468 ± 81
$11.0 < L_{xy} < 20.0$	301 ± 53	”
$L_{xy} > 20.0$	459 ± 66	”
$L_{xy} > 0.25$ (full sample)	414 ± 31	388 ± 33

Table 6.5: B^0 lifetime in 4 bins of $L_{xy}(K^0_s)$, for both this analysis, and an analysis where COT-only tracks are always used for the K^0_s.

6.5 V_0 Tracking in the COT

A reasonable approach to this analysis might have been to always use COT-only tracks for K^0_s and Λ, but this is not the method we have chosen. As previously mentioned, we use COT-only tracks for V_0's with $L_{xy} > 11$ cm, since the SVX ends at 10.6 cm. For $L_{xy} < 11$ cm, we use `defTracks`, and drop any SVX hits from a radius smaller that the radius of decay of the V_0. This is done by finding the COT only tracks corresponding to those `defTracks`, determining the radius of decay r_{COT} of the V_0 using the COT-only tracks, and then dropping any SVX hits on the `defTracks` coming from layers which have r less than than r_{COT}.

We observe a few problems when using the COT only method. The first can be seen in Table 6.5. The B^0 lifetime for candidates with $L_{xy}(K^0_s) < 7$ cm is significantly smaller when using COT-only tracks. We do not observe this problem when we allow SVX hits on the tracks. We must point out that the samples here do not contain exactly the same events. The sample changes because when we compute the values of quantities on which we make requirements, we are using different tracks.

An additional effect shows up more significantly in the COT-only analysis. This is the dependence of the B^0 lifetime on decay direction of the B^0 in the transverse plane. We draw a 2d vector from $(0,0)$ to the beamspot, take the dot product with (p_x, p_y) of the B^0 and define the following: When the dot product is greater then zero, we say the B^0 goes "up". When it is less than zero, we say the B^0 goes "down". See Figure 6.3. If we divide the samples into up and down, we obtain the results in Table 6.6. For our standard analysis, we obtain $c\tau = 439 \pm 44\mu$m for "up" and $c\tau = 315 \pm 75\mu$m for "down": a difference of 1.4σ. For the COT-only analysis, we obtain $c\tau = 441 \pm 50\mu$m for "up" and $c\tau = 288 \pm 50\mu$m for "down": a difference of 2.2σ.

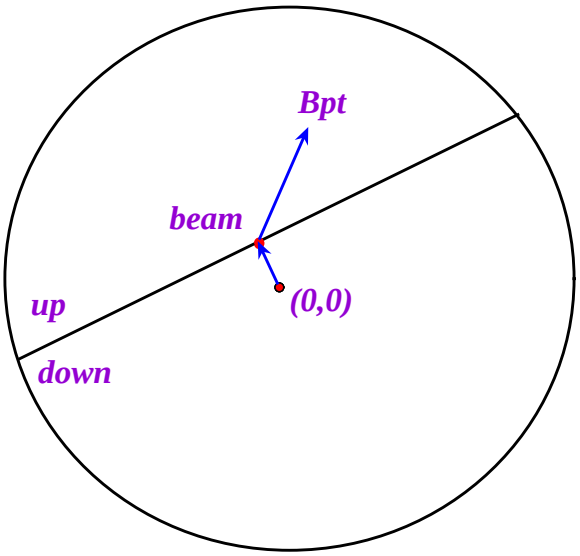

Figure 6.3: Definition of decay direction in systematic error study

We see that the difference in lifetime for "up" and "down" is more apparent in the case where COT-only tracks are used for the K^0_s. In addition, the widths of the B^0

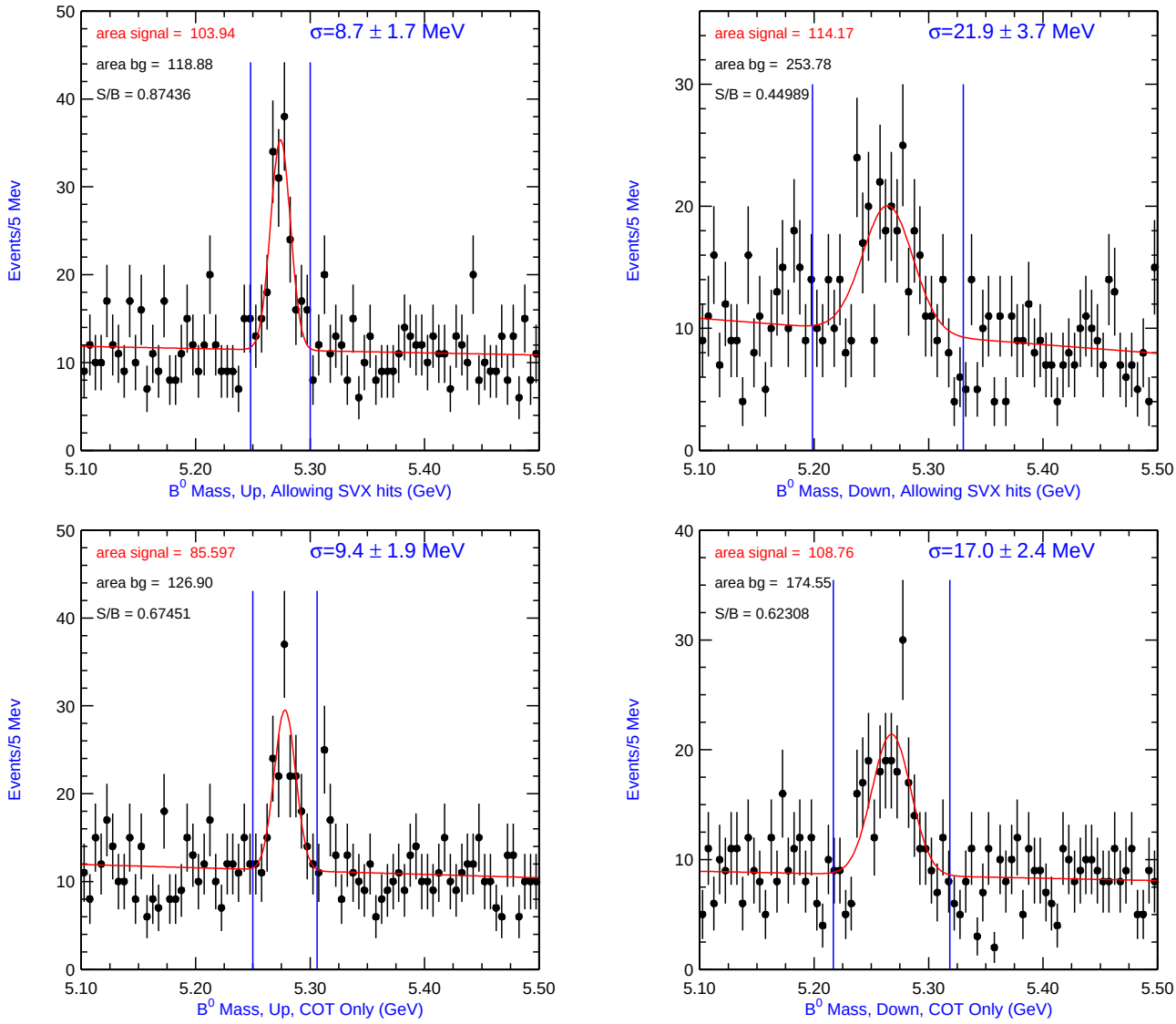

Figure 6.4: B^0 invariant mass for our standard analysis(top), and for an analysis where COT-only tracks are always used for K^0_s reconstruction(bottom). For both cases, the invariant mass is shown for two different B^0 decay directions: up and down (See Figure 6.3.)

Direction	Standard Analysis			COT-only for K_s^0
	N_{signal} ($L_{xy}(K_s^0) < 11$ cm)	N_{signal} ($L_{xy}(K_s^0) > 11$ cm)	$c\tau(\mu\text{m})$	$c\tau(\mu\text{m})$
all	102 ± 21	102 ± 19	414±31	388±33
up	67 ± 12	36 ± 11	439 ± 44	441 ± 50
down	35 ± 24	65 ± 12	315 ± 75	288 ± 50
Δ significance (up-down)			1.4σ	2.2σ

Table 6.6: Variation of B^0 lifetime with direction of decay, for this analysis, and for the case when COT-only tracks are always used for the K_s^0.

mass peaks are different depending on the decay direction of the B^0. The differences in the mass widths, however, are not any larger in the case of the COT-only analysis. Figure 6.4 shows the plots of invariant mass corresponding to the lifetime entries in the table. One possible explanation for these effects is a misalignment between the SVX and COT. It is also possible that the errors assigned to COT track parameters are underestimated more than those for tracks with SVX hits, and this causes a selection bias.

We have also compared results from the standard analysis to the COT-only analysis for the case where $L_{xy}(K_s^0)$ <11 cm, where both K_s^0 tracks have SVX hits. We measure the lifetime using three different strategies:

1. Treat the K_s^0's as we normally do when $L_{xy} < 11$ cm:

   make requirements on all K_s^0 quantities computed with SVX tracks, and use pion SVX tracks for computation of B^0 invariant mass

2. Treat the K_s^0's as we normally do when $L_{xy} > 11$ cm:

   make requirements on all K_s^0 quantities computed with COT-only tracks, and use pion COT-only tracks for computation of B^0 invariant mass

3. Hybrid of the above: Make requirements using SVX tracks, but use COT-only tracks for pions in the computation of the B^0 mass.

The values obtained for the lifetimes in the three cases are shown in Table 6.7. These results indicate that the bias is in the COT selection. That is for case 2), the only case in which COT selection is used, we obtain a much lower value of $c\tau$ then for cases 1) and 3), where the values of $c\tau$ differ by only 3μm.

Strategy	$c\tau(B^0)(\mu\text{m})$
1	403 ± 42
2	329 ± 63
3	406 ± 54

Table 6.7: Values obtained for the B^0 lifetime in 3 different treatments of the case where $L_{xy}(K^0_s) > 11$ cm and both pions from the K^0_s have SVX hits.

Since approximately half of the sample in our standard analysis uses COT-only tracks for the K^0_s, we assign a systematic error due to V_0 tracking in the COT. This is the difference between our result for the B^0 lifetime doing the standard analysis, and the result obtained when using COT-only tracks for the K^0_s.

$$\text{Error} = c\tau(B^0) - c\tau(B^0,\text{COT-only}) = 414\mu\text{m - } 388\mu\text{m} = 26\mu\text{m}$$

6.6 Luminosity/Occupancy

We have observed statistically significant variations in the width of the B^0 mass peak as a function of run number (see Section A.2). Pursuing the effect further, we divide the B^0 control sample data into 3 bins of instantaneous luminosity; the boundaries we use are $1.17\times10^{31}\text{cm}^{-2}\text{s}^{-1}$ and $1.7\times10^{31}\text{cm}^{-2}\text{s}^{-1}$. The invariant mass

distributions for B^0 candidates in the three different regions are shown in Figure 6.5. The width is very large in the highest luminosity region (24 ± 5 MeV) and the signal to noise is significantly worse than in the lower luminosity regions (0.32 compared to 0.72). In the two lower luminosity regions, the widths agree within the statistical error, and are compatible with the monte-carlo width prediction of 13 MeV. Since the width of the B^0 mass peak is dominated by detector resolution, it should not be related to the lifetime. However, increased luminosity results in increased occupancy, which can worsen mass resolution. It is possible that this degradation is a sign of increased tracking failures in the denser environment, which may bias the lifetime.

We fit the B^0 lifetime for the low($< 1.7\times10^{31}\mathrm{cm}^{-2}\mathrm{s}^{-1}$) and high($> 1.7\times10^{31}\mathrm{cm}^{-2}\mathrm{s}^{-1}$) luminosity regions, using both the separate and the 2d simultaneous fitting methods. The results we obtain with the two methods are quite different, and are shown in Figure 6.6 and Figure 6.7. The results of the separate fit, which we use for the determination of the central value, indicate that B^0's in the low and high luminosity region have the same lifetime, within errors. We obtain $c\tau = 438 \pm 39\mu$m for low luminosity and $c\tau = 383 \pm 55\mu$m for the high luminosity. There is however a 2σ difference when using the 2-d simultaneous fit. We obtain $455 \pm 40\mu$m for the low luminosity region, and $324 \pm 50\mu$m for the high. We believe that this does not necessarily mean that there is a bias at large luminosity. It is possible that the mass resolution is so poor that signal events are being smeared into the background region, giving it an artificially high lifetime. The separate fit is less sensitive to this effect since events between 3 and $6\sigma_m$ are not used in the fit.

We do assign a systematic error, since it is possible that this effect manifests itself when doing the separate fit, only to a lesser extent. The error is estimated by

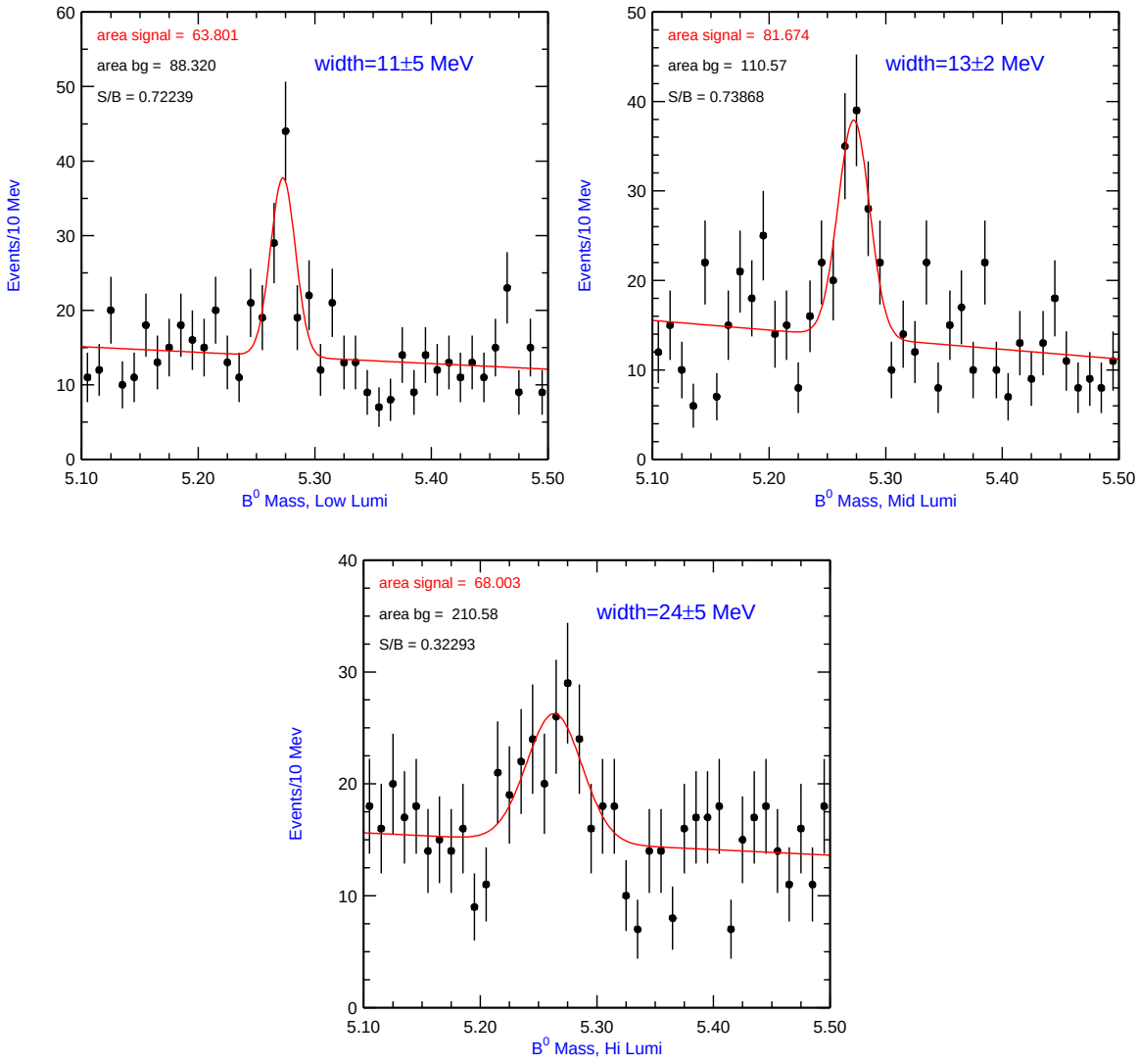

Figure 6.5: Width of the B^0 mass peak in 3 regions of instantaneous luminosity. We divide the data at 1.170×10^{31} and 1.7×10^{31} cm^{-2} s^{-1}

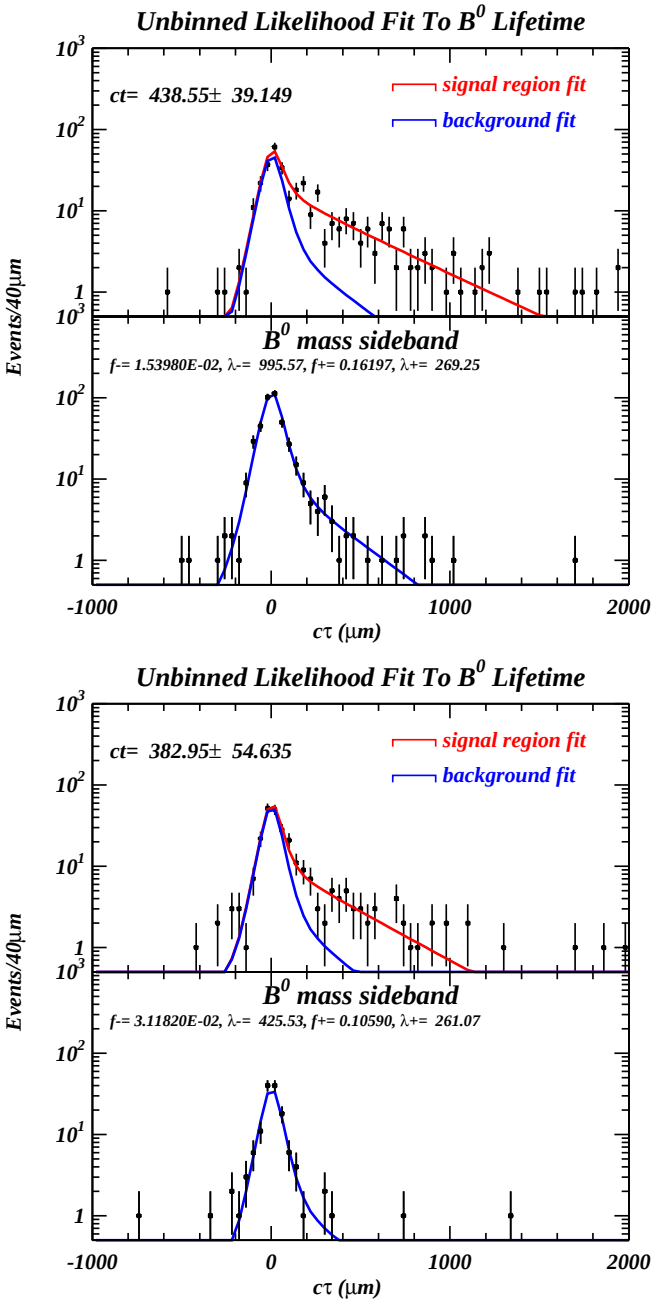

Figure 6.6: Results of the separate mass/lifetime fit in two luminosity regions. The upper plot shows the B^0 lifetime fit for the 2/3 of the data with instantaneous luminosity less than $1.7\times10^{31}\mathrm{cm}^{-2}\mathrm{s}^{-1}$. The lower plot shows the B^0 lifetime fit for the remaining data with higher instantaneous luminosity.

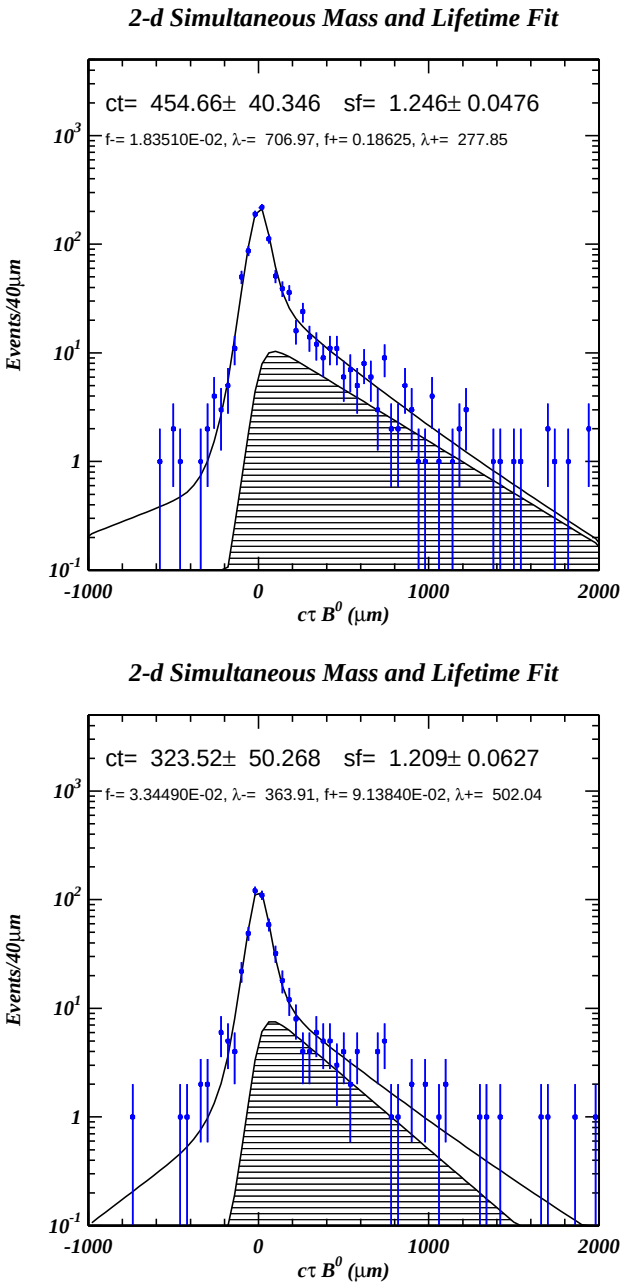

Figure 6.7: Results of the 2-d simultaneous mass and lifetime fit in two luminosity regions. The upper plot shows the B^0 lifetime fit for the 2/3 of the data with instantaneous luminosity less than $1.7\times10^{31}\mathrm{cm}^{-2}\mathrm{s}^{-1}$. The lower plot shows the B^0 lifetime fit for the remaining data with higher instantaneous luminosity.

taking the difference between the fit lifetime value using the separate fit in the high luminosity region and the world average B^0 lifetime. The difference is then weighted by the fractional contribution of the high luminosity data to the entire sample.

$$\Delta c\tau = c\tau(\text{PDG}) - \text{c}\tau(\text{hi}) = (462 - 383)\mu\text{m} = 79\mu\text{m}$$

$$\text{Weight(hi)} = \frac{1}{1+\left(\frac{\sigma_{\text{c}\tau(\text{hi})}}{\sigma_{\text{c}\tau(\text{lo})}}\right)^2}$$

$$\text{Error} = \Delta\text{c}\tau \times \text{Weight(hi)} = 25\mu\text{m}$$

We assign a 25μm systematic error due to detector occupancy.

6.7 SVX Alignment

For our systematic error due to imperfect alignment of the SVX, we use $\pm 5\mu$m, which was obtained using the B_s lifetime control sample, $B^+ \to J/\psi + K^+$ [55].

6.8 Summary of Systematic Errors

Table 6.8 summarizes the errors described in the preceding section. All systematic errors, excluding for the error due to SVX aligment, were determined using the $B^0 \rightarrow J/\psi K_s^0$ control sample.

Source	Value ($\pm\mu$m)
ct Resolution Function	1
SVX Alignment	5
Occupancy	25
Fitting Model	22
V0 Tracking	26
Total	43

Table 6.8: Systematic errors

Chapter 7

Conclusions

We have reconstructed 46 ± 9 Λ_B decays in the mode $\Lambda_B \to J/\psi\Lambda$, where $J/\psi \to \mu^+\mu^-$ and $\Lambda \to p^+\pi^-$, and 246 ± 16 B^0 decays in the mode $B^0 \to J/\psi K_s^0$, where $J/\psi \to \mu^+\mu^-$ and $K_s^0 \to \pi^+\pi^-$. We use the B^0 sample as a control sample for the Λ_B lifetime measurement. For the B^0 lifetime, we obtain a result within 1.5σ of the current world average of 462 μm. Having validated our method, we measure the lifetime of the Λ_B. We obtain

$$c\tau(\Lambda_B) = 374 \pm 78(stat.) \pm 43(syst.)\mu\text{m}$$

$$\tau(\Lambda_B) = 1.25 \pm 0.26(stat.) \pm 0.14(syst.)\text{ps}$$

where the systematic error was evaluated using our control sample of $B^0 \to J/\psi K_s^0$. This is the first measurement of the Λ_B lifetime in a fully reconstructed mode.

Using the current PDG world average for the B^0 lifetime, we obtain

$$\frac{\tau(\Lambda_B)}{\tau(B^0)} = 0.806 \pm 0.192 \tag{7.1}$$

This in in agreement with both the theoretical prediction and the current PDG world average from semileptonic Λ_B decay modes. This measurement is statistically limited. More data is needed to test the agreement between the theoretical prediction and the experimental value for $\tau(\Lambda_B)/\tau(B^0)$ in this decay mode.

Appendix A

Appendices

A.1 COT Tracking Algorithms

The J/ψ sample that we use in this analysis has been "officially" processed by Production version 4.8.4a. During Production, muons are reconstructed and track reconstruction, both COT and SVX, is performed.

When we perform our analysis using the output of the official Production, we find that the lifetime in our B^0 control sample is low. Figure A.1 shows the lifetime fits using the separate fit and the 2d simultaneous mass and lifetime fit. With the separate fit, we obtain $c\tau(B^0) = 363 \pm 27\mu$m. This is 3.7σ below the PDG average of 462μm [56]. With the 2-d simultaneous mass and lifetime fit, we obtain $373 \pm 28\mu$m, 3.25σ below the world average.

We have investigated whether or not this can be due to a bias in one of the pattern recognition algorithms used in the COT Tracking. CDF currently has two algorithms which perform COT tracking. The first algorithm, Segment Linking (SL) is very

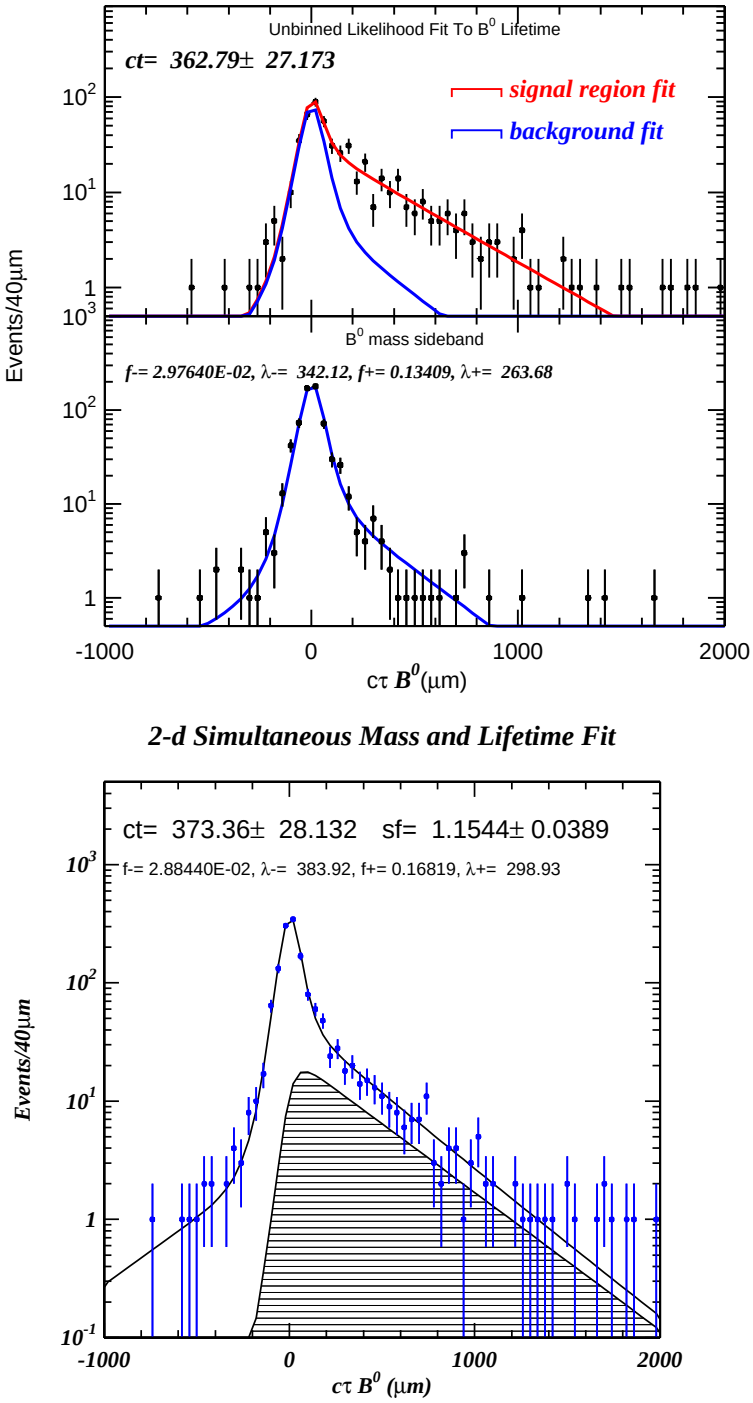

Figure A.1: B^0 control sample lifetime with standard Production. Top: lifetime with separate fit. Bottom: lifetime with 2-d simultaneous mass and lifetime fit.

similar to the Run I tracking algorithm which is described in detail in Reference [47]. This method links full segments at the pattern recognition stage. The second algorithm, Histogram Linking (HL) is a supplemental algorithm intended to add tracks that SL failed to find. Hits added to the track are not required to be part of a complete segment. This algorithm is most efficient for primary tracks because the search road is constrained to point to the beam spot, thus assuming a track with negligible impact parameter. The implementation and performance of this algorithm are described in [48].

During the axial pattern recognition stage of COT tracking, both algorithms are run. When this is complete, stereo reconstruction is performed. Finally, a merging algorithm determines which tracks have been found by both HL and SL by examining the hit content. If a matched pair is found, it checks whether the tracks have

1. 3 or more axial layers with at least 6 hits each
2. 3 or more stereo layers with at least 6 hits each
3. at least 20 axial hits and 20 stereo hits

If both satisfy the above, the SL track is kept. If only the HL satisfies the above, the HL track is kept. If neither satisfy the above, the track with more hits is kept.

These are stringent requirements for V_0's. Since V_0's have a long lifetime, they decay later, and naturally have fewer hits than standard prompt tracks. Long lived particles also have much larger impact parameters, but the HL tracking is generally biased towards small impact parameter. Given this, we suspect that there may be a bias on the lifetime caused by the use of HL tracks. We have rerun the tracking in three different configurations in order to compare results:
1) SL only, 2) HL only, 3) the default way: SL and HL merged.

First, we examine events which were found in both 1) and 3), and events that were found in 3) but not 1). Figure A.2 shows ct of the B^0 using the J/ψ vertex only for the secondary vertex. The top plot shows the events found in both the merged sample and the SL-only sample. The bottom plot shows events shows those found only in the merged sample, but not the SL-only sample. i.e., the bottom plot shows the supplemental events added by HL. In this plot, both the signal and the sideband regions have approximately zero lifetime. This gives evidence that a bias is present. The efficiency for finding B^0 events in the merged sample (as a result of HL tracking) is smaller for events with large ct than for events with small ct.

To investigate the effect on the K_s^0 we examine the events which are common between the merged and SL only samples. Then, in the case where one of the tracks from the K_s^0 is an HL track in the merged sample, we plot the difference in L_{xy} for the SL K_s^0 and the merged K_s^0. This is shown in Figure A.3. The mean of the distribution is 3.009 cm, with an error of approximately 0.4 cm, which demonstrates that there is statistically significant bias induced by HL in the K_s^0 decay length distribution

Given the biased distributions, we believe that there is sufficient motivation for the elimination of HL tracks, provided there is not too much loss in signal. The effect of the removal of HL Tracking is shown on the left in Figure A.4. Here, we plot invariant mass distributions of B^0 candidates in the SL-only sample and in the default merged sample. In the merged sample, we obtain 206 ± 24 B^0 candidates, and in the SL-only sample we obtain 205 ± 28 candidates. The loss of events in excluding HL tracks is negligible.

Differences in HL/SL events are almost always due to loss or misreconstruction of the K_s^0. When the merging runs, if the SL track does not pass the above hit require-

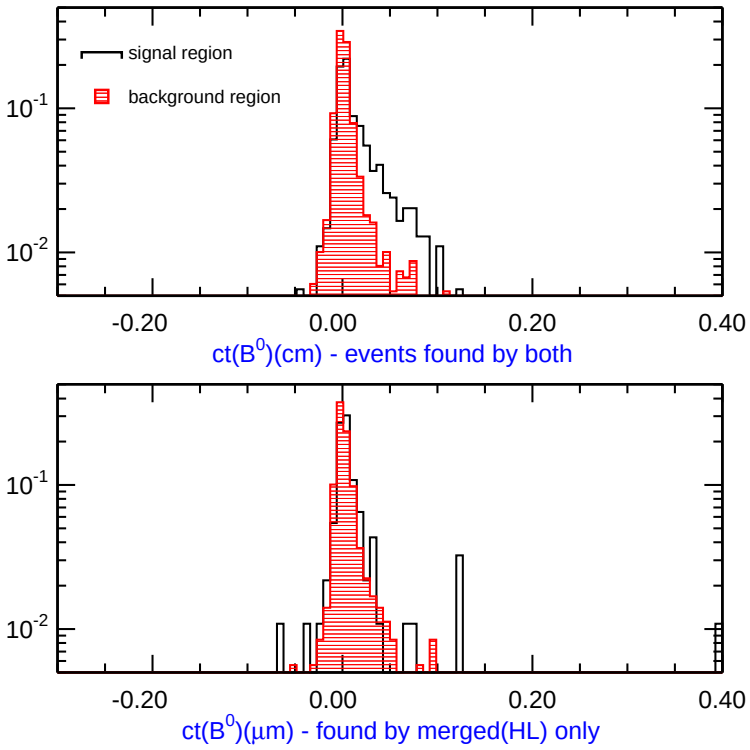

Figure A.2: Distributions of B^0 proper decay lengths(ct) for events found by different tracking algorithms. The top plot shows events found in both the merged sample and the sample of SL only. The bottom plot shows those found in the merged sample, but not in the SL only sample. These events are due to the tracks added by HL. In both the upper and lower plots, the signal regions are shown in the unshaded histograms, and the sideband regions are shown in the shaded histograms.

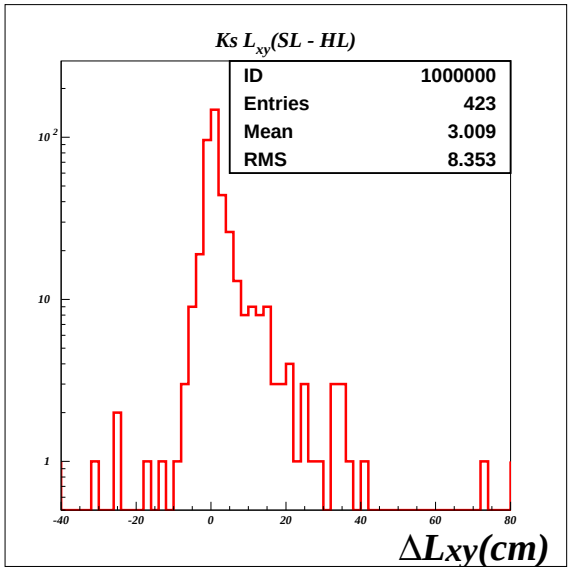

Figure A.3: L_{xy}(SL)-L_{xy}(HL) for same events, SL only sample and merged sample. The merged sample consists of events where one or more of the tracks from the K_s^0 are HL.

ments, but the HL track does, the K_s^0 sometimes becomes so biased or badly vertexed, that it no longer passes the analysis requirements for the B^0 sample. We would like to emphasize that the HL/merged tracking mainly effects the K_s^0 reconstruction. The muons from the J/ψ will be effected only a small percentage of the time.

Finally, we examine the lifetime fits from our B^0 control sample. We compare fits in data where HL only was run, to those where SL only was run. The fits are shown in Figure A.5.

We obtain $c\tau = 338 \pm 36 \mu$m for the HL sample, and $414 \pm 31 \mu$m for the SL sample. The current world average is 462μm [56]. Since both of the above measurements are from the same data sample, the significance is no longer Δ/σ. Even if this were the case, the effect is very large. Thus, for this analysis and the measurement of the Λ_B lifetime, we use only data which has been reprocessed with SL-only tracking. All

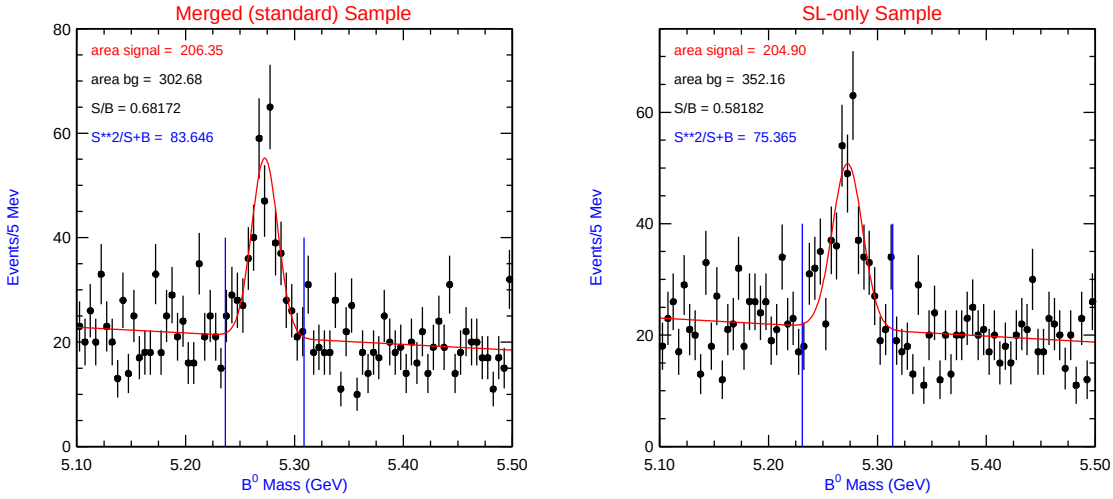

Figure A.4: B^0 mass distribution from merged sample and SL-only sample

plots presented in this thesis, excluding the appendices, have been made using the SL only sample.

We would like to stress that whatever the source of this bias, it cannot be eliminated by simply selecting SL only tracks from a merged set of SL and HL tracks. It is necessary to rerun the tracking to recover the "lost" SL tracks, which are rejected in favor of an HL track with more hits. In addition, we would like to emphasize that this is a selection bias on the $J/\psi K_s^0$ sample, rather than a systematic bias on lifetime. We use the J/ψ vertex for the determination of L_{xy} and ct. The HL tracking has little effect on J/ψ vertex itself. It does however, have a large effect on the K_s^0 - many are misreconstructed.

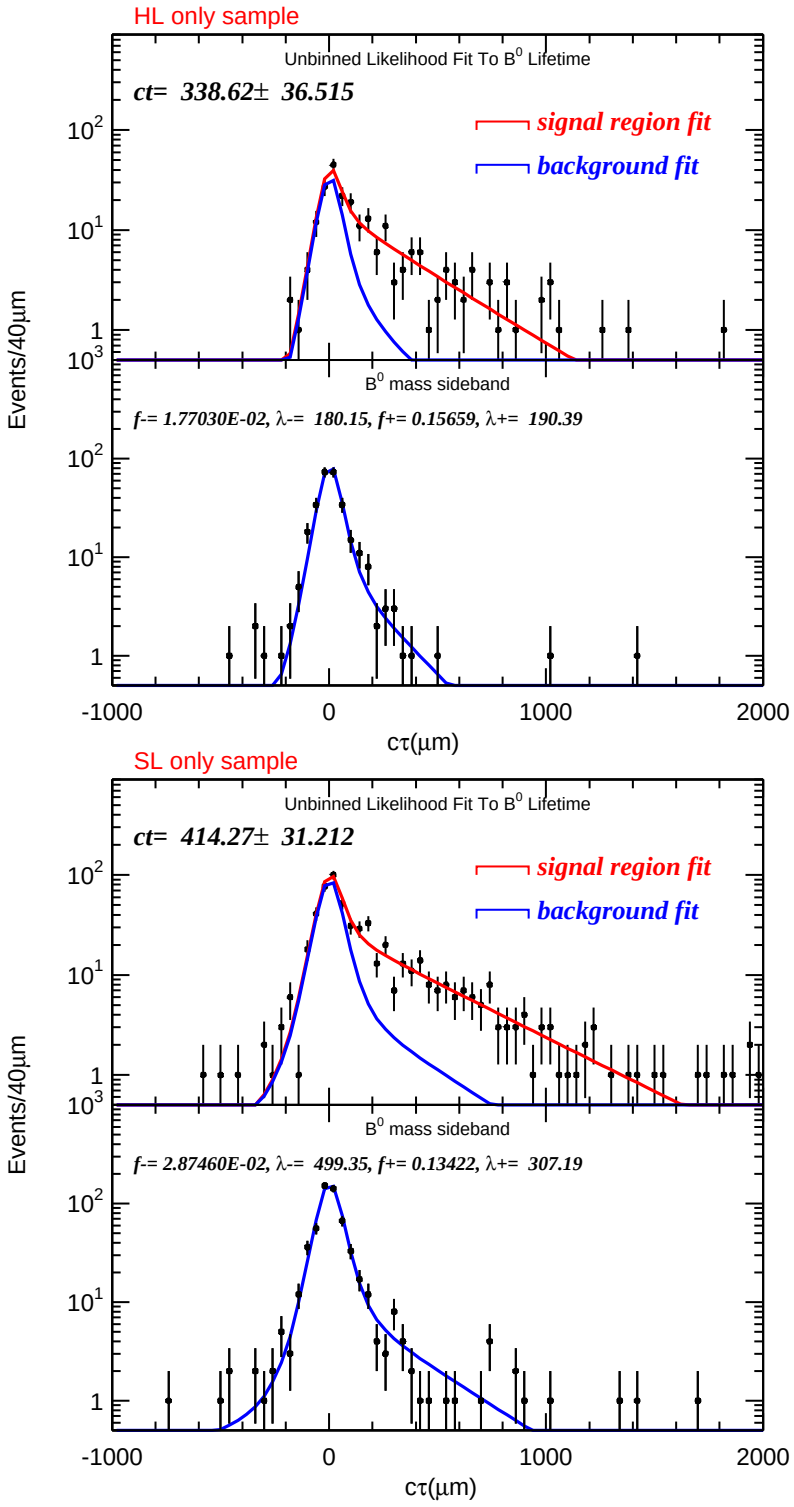

Figure A.5: Fits for the B^0 control sample lifetime with HL only tracking (top) and SL only tracking(bottom)

A.2 Run Dependence

This section discusses results obtained when running on the J/ψ dataset processed by the "official" version of Production, and on the reprocessed version with SL-only COT tracking. The motivation for the reprocessing is discussed in Section A.1.

Decreases in event yield have been seen in many of the exclusive B to J/ψ decay modes, as well as in some of the semileptonic modes. That is, we reconstruct more B^0 per J/ψ before Sept. 4, 2002 than we do after that date. This is not the date on which things definitely change for the worse. It corresponds to run 150958 which was a natural run at which to split the data, since this had been done in Production.

In addition to the decrease in signal yield, we observe a large change in the width of the B^0 invariant mass peak, from 7.2 ± 1.4 MeV to 15.4 ± 2.6 MeV. This is shown in Figure A.6. The figure shows results using the dataset from the "official" version of Production, but the results are approximately the same when using the reprocessed sample. The signal to background ratio is down by a factor of 2 in the later data. Figure A.6 also shows the mass pull distributions for the B^0. Before run 150958, the width of the pull was 1.03 ± 0.18. If the tracking errors are estimated correctly, the width should be 1.0. After run 150958, the width is 1.73 ± 0.29.

Since the B^0 width is dominated by detector resolution, there is no reason *a priori* that a broadening of the width should result in a change in lifetime. We have checked this in the "official" sample and in the reprocessed sample.

In the "official" sample, We fit the B^0 lifetime for the earlier and later data using the separate fitter. The results are shown in Figure A.7. In the earlier data, we obtain $c\tau(B^0) = 407 \pm 45\mu$m. In the later data we obtain $c\tau(B^0) = 341 \pm 36\mu$m.

Here, we use the average background fraction obtained when fitting the mass peak including all of the data. The values are statistically consistent with each other, but the value for the later data is inconsistent with the world average of 462μm. With the 2-d simulataneous mass and lifetime fit, we obtain $408 \pm 45\mu$m for the early data, and $343 \pm 36\mu$m for the later data. Here f_B is determined seperately for each subset of data, but the results are approximately the same.

We also check for a run-dependent lifetime in SL-only reprocessed sample, using the same methods as described above. With the separate fit, we obtain $c\tau(B^0) = 439 \pm 53\mu$m for the earlier data, and $412 \pm 41\mu$m for the later data. With the 2-d simultaneous mass and lifetime we obtain $411 \pm 40\mu$m in the early data, and $421 \pm 48\mu$m in the later data.

Though the run-dependent width effect remains in the SL-only sample, the difference in lifetimes in the earlier and later data is smaller.

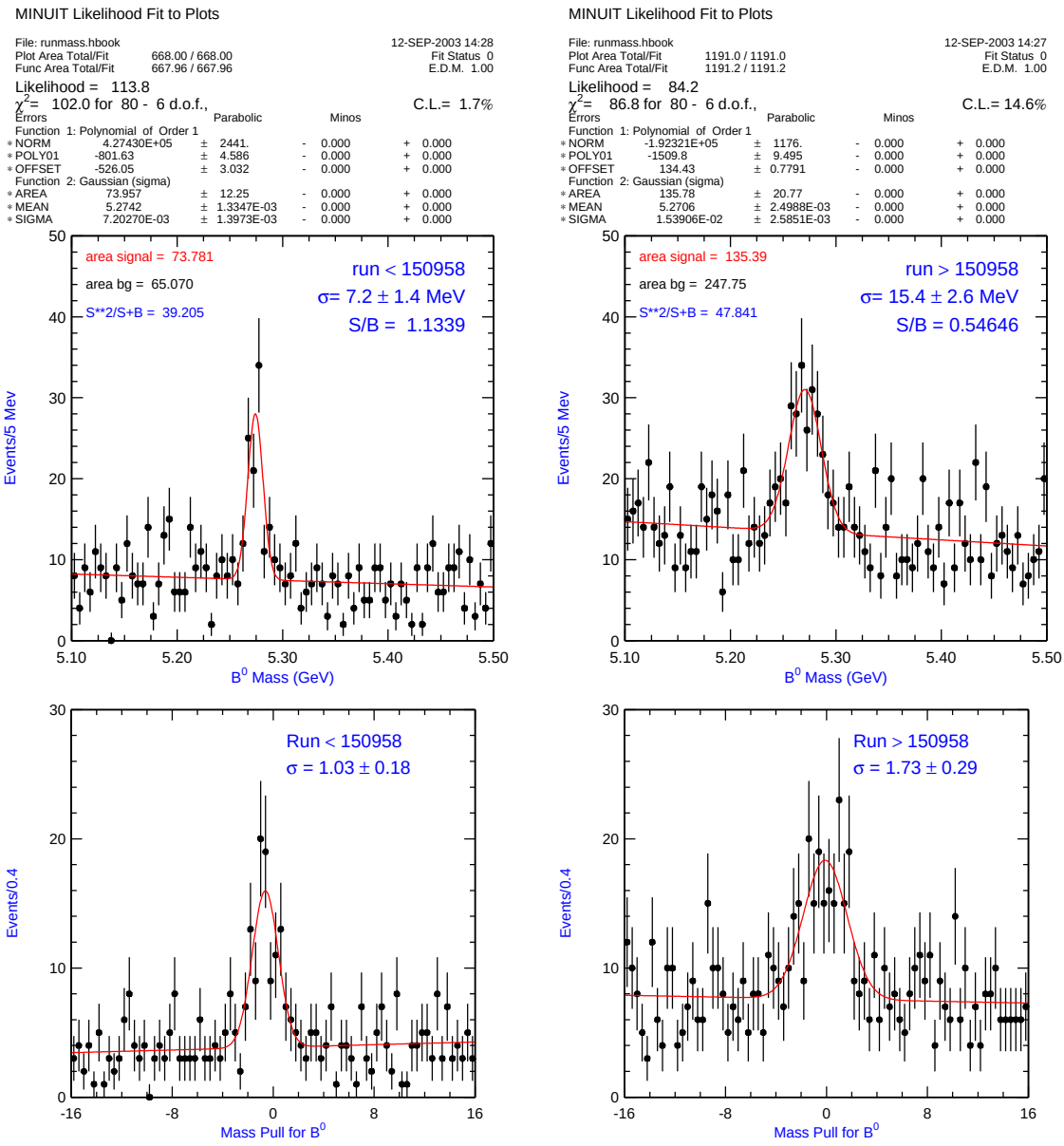

Figure A.6: B^0 mass peaks for two different run ranges

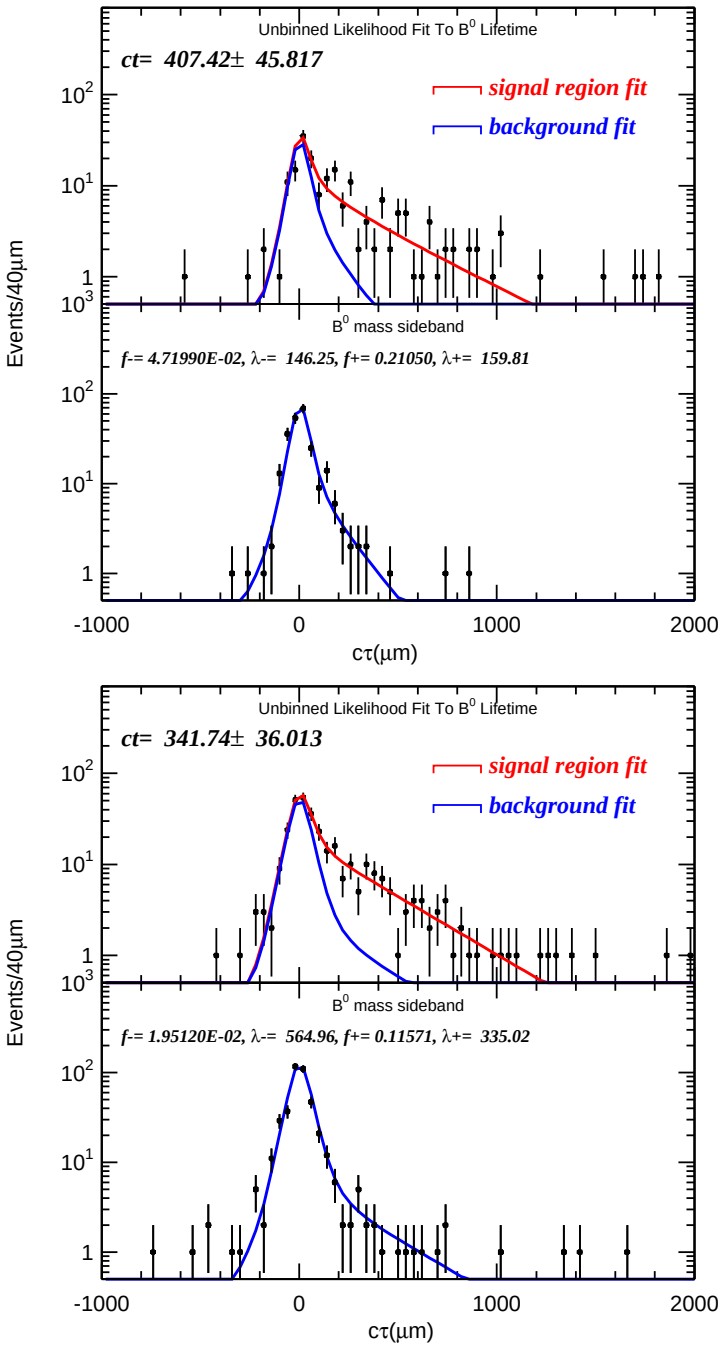

Figure A.7: Separate mass/lifetime fit for B^0 using two different run sections. The fit on the top includes data from runs 138425-150958 ($\approx 25pb^{-1}$with SVX integrated). The fit on the bottom includes data from runs 150958-156487 ($\approx 40pb^{-1}$ with SVX integrated). The data used here are the output of the "official" Production run, with merged COT tracking

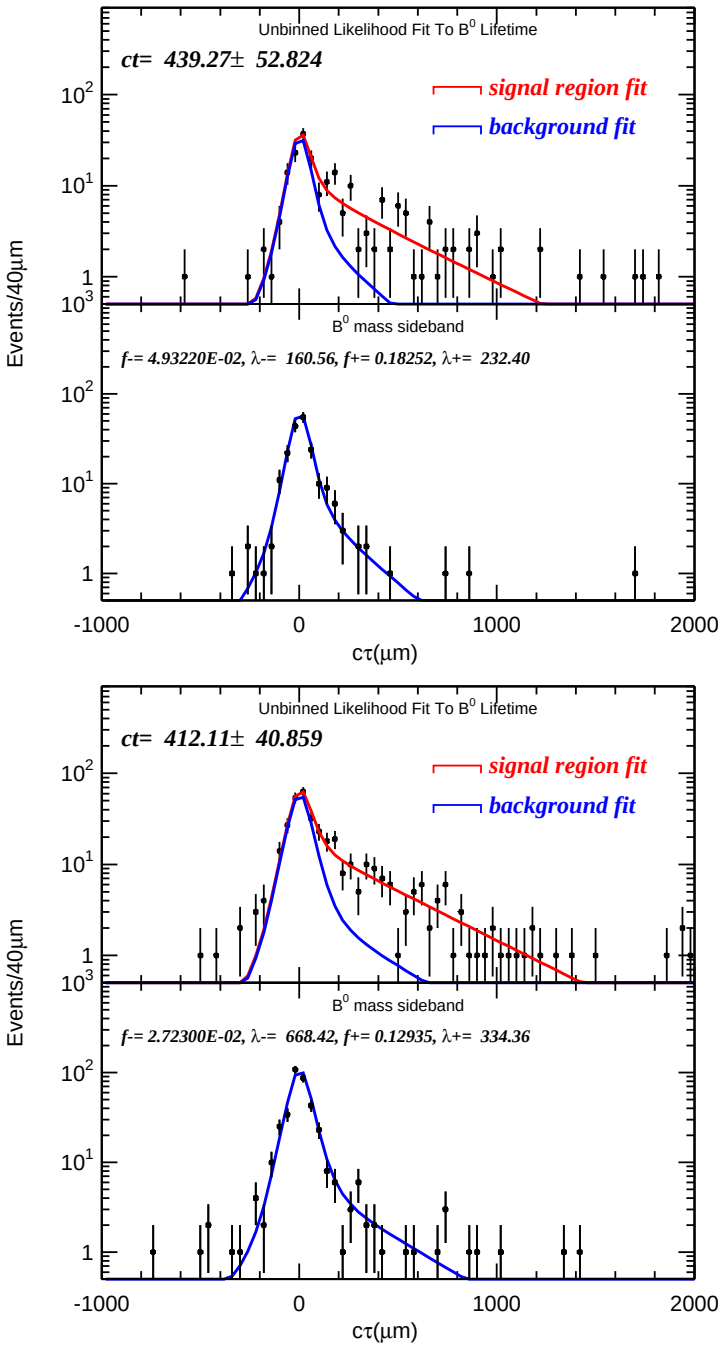

Figure A.8: top: Separate mass/lifetime fit for B^0 using two different run sections. The fit on the top includes data from runs 138425-150958 ($\approx 25pb^{-1}$with SVX integrated).The fit on the bottom includes data from runs 150958 to 156487 ($\approx 40pb^{-1}$ with SVX integrated).The data used here are from the reprocessed sample, with SL-only COT tracking

A.3 CDF Specific Details

1. We use `KalFitter` to refit our tracks.

2. We do not use the Phantom Layer when refitting our tracks.

3. We are running on 4.8.4a Production, so we use use `Pass08`, for calibration, which loads alignment table `'100030 1 GOOD'`.

4. Primary vertices are from the `VertexColl`

5. We use only beamlines determined using SVX tracks (`SvxBeam`), with "history code" 19.

Bibliography

[1] C. Albajar *et al.*, First Observation of the Beauty Baryon Λ_B in the decay channel $\Lambda_b \rightarrow J/\psi\Lambda$ at the CERN proton-antiproton collider, *Phys. Rev. D* **273**, 540 (1991).

[2] DELPHI Collaboration (P. Abreu *et al.*), Search for Exclusive Decays of the Λ_B Baryon and Measurement of its Mass, *Phys. Lett. B* **374**, 351 (1996).

[3] ALEPH Collaboration (D. Buskulic *et al.*), Measurement of the Mass of the Λ_B Baryon *Phys Lett. B*, **380**, 442 (1996).

[4] F. Abe *et al.*, Search for $\Lambda_b \rightarrow J/\psi\Lambda$ in $p\bar{p}$ Collisions at $\sqrt{s} = 1.8\,TeV$, *Phys.Rev. D* **47**, R2639 (1993).

[5] F. Abe *et al.*, Observation of $\Lambda_b \rightarrow J/\psi\Lambda$ at the Fermilab Proton-Antiproton Collider, *Phys.Rev. D* **55**, 1142 (1997).

[6] F. Abe *et. al.*, Measurement of Λ_b^0 Lifetime Using $\Lambda_b^0 \rightarrow \Lambda_c^+ l^- \bar{\nu}$, *Phys. Rev. Lett.* **77**, 1439 (1996).

[7] G. Kane, Modern Elementary Particle Physics, Addison-Wesley, (1993).

[8] I. I. Bigi, The Lifetimes of Heavy Flavour Hadrons - A Case Study in Quark-Hadron Duality, UND-HEP-99-BIG 07 (1999).

[9] I. I. Bigi, Lifetimes of Heavy-Flavour Hadrons - Whence and Whither, UND-HEP-95-BIG 06 (1995).

[10] G. Bellini, I. I. Bigi, and P. J. Dornan, Lifetimes of Charm and Beauty Hadrons, UND-HEP-96BIG02 (1996).

[11] M. Neubert, Heavy-Quark Effective Theory and Weak Matrix Elements, CERN-TH/98-2 (1998).

[12] ALEPH, CDF, DELPHI, L3, OPAL, SLD, Combined Results on b-Hadron Production Rates and Decay Properties, CERN-EP/2001-050 (2001).

[13] I. I. Bigi, Heavy Quark Expansions for Inclusive Heavy-Flavour Decays and the Lifetimes of Charm and Beauty Hadrons, UND-HEP-96-BIG 06, 20 (1996).

[14] J. L. Rosner, Enhancement of the Λ_B Decay Rate, hep-ph/9602265, 2(1996).

[15] M. Neubert and C.T. Sachrajda, Spectator Effects in Inclusive Decays of Beauty Hadrons, *Nucl. Phys.* B**432**, 339(1997).

[16] LEP B Lifetimes Working Group, `http://lepbosc.web.cern.ch/LEPBOSC/lifetimes/lepblife.html`

[17] C. W. Schmidt, The Fermilab 400-MeV Linac upgrade, FERMILAB-CONF-93-111 (1993).

[18] J. Marriner, Stochastic Cooling Overview, FERMILAB-CONF-03-158 (2003).

[19] Fermilab Beams Division, Run II Handbook,
http://www-bd.fnal.gov/runII/index.html

[20] The Collider Detector at Fermilab, A compilation of articles reprinted from Nuclear Instruments and Methods in *Physics Research* - *A*(1988).

[21] The CDF II Collaboration, The CDF II Detector Technical Design Report, FERMILAB-Pub-96/390-E, (1996).

[22] G. Gomez for the TOF group, The CDF-II Time of Flight Detector, CDF internal Note 6258, (2003).

[23] E.J. Thomson *et. al*, Online Track Processor for the CDF Upgrade, *IEEE Transactions on Nuclear Science*, **49** No. 3, (2002).

[24] W. Ashmanskas *et. al*, The CDF Silicon Vertex Trigger, FERMILAB-CONF-03/168-E (2003).

[25] W. Riegler *et. al*, COT Detector Physics Simulations, CDF internal Note 5050 (2000).

[26] R. Wagner *et. al*, CDF Central Outer Tracker, CDF Note 6267 (2003).

[27] A. Sill, CDF Run II Silicon Tracking Projects, *Nuclear Instr. and Meth.*, **A447** (2000).

[28] P. Tamburello, COT Standalone Tracking,
http://www-cdf.fnal.gov/internal/people/links/PeterTamburello/CT_TrackingModule.html

[29] K. Bloom, Outside-In Tracking Description,
http://www-cdf.fnal.gov/upgrades/computing/projects/reconstruction/tracking/user-docs/OIoverview.html

[30] G. Ascoli *et. al*, CDF Central Muon Detector, *Nucl. Instr. and Meth.*, **A268** (1988).

[31] J. Lewis *et. al*, The 1992 CDF Muon System Upgrade, CDF internal Note 2858, (1994).

[32] P. Schlabach, CDF Central Muon Detector,
http://www-cdf.fnal.gov/internal/upgrades/muon/cmu.html

[33] P. Schlabach, CDF Central Muon Upgrade Detector,
http://www-cdf.fnal.gov/internal/upgrades/muon/cmp.html

[34] The CDF II Collaboration, The CDF II Detector Technical Design Report, FERMILAB-Pub-96/390-E, (1996).

[35] P. Schlabach, CDF Central Muon Upgrade Detector,
http://www-cdf.fnal.gov/internal/upgrades/muon/cmx.html

[36] The CDF Production Farm, http://fpcc.fnal.gov/

[37] F. Abe *et. al.*, Measurement of Λ_b^0 Lifetime Using $\Lambda_b^0 \to \Lambda_c^+ l^- \bar{\nu}$, *Phys. Rev. Lett.* 77, 1439 (1996).

[38] T. Yamashita *et. al*, Measurement of $Br(\Lambda_b \to J/\psi\Lambda)$, CDF internal Note 6643 (2003).

[39] L. Hollaway and J. Strologas, Determination of the XTRP maps, CDF internal Note 4146 (1997).

[40] J. Marriner, Secondary Vertex Fit with Mass and Pointing Constraints (`CTVMFT`), CDF internal Note 1996, (1993).

[41] K. Anikeev *et. al.*, Description of Bgenerator II, CDF internal Note 5092 (1999).

[42] J. Lewis and P. Avery, CLEOMC: The CDF Interface to the CLEO Monte Carlo (QQ), Cdf Internal Note 2724 (1994).

[43] CDF Detector Simulation, `http://www-cdf.fnal.gov/cdfsim/cdfsim_main.html`

[44] K. Anikeev, Blessed Result for B_s Lifetime, `http://www-cdf.fnal.gov/physics/new/bottom/030715.blessed-excl-lft/`

[45] K. Burkett, Measurement of the Lifetime of the B_s^0 Meson and the Width Difference in the $B_s^0 - \bar{B}_s^0$ System in $p\bar{p}$ Collisions at $\sqrt{s} = 1.8$ TeV, PhD Thesis (1997).

[46] A. Korn *et. al.,* Update on Calibration of Energy Loss and Magnetic Field using J/ψ Events in Run II, CDF internal Note 6355

[47] A. Mukherjee, CTC and VTX Tracking, CDF internal Note 5490

[48] P. Gatti(thesis), Performance of the new tracking system at CDF II, CDF internal Note 5561

[49] M. Bishai *et. al.*, COT and SVXII Tracking Performance, CDF internal Note 5391

[50] CDF Update at internal J/ψ Meeting by K. Anikeev,
www.fnal.gov/internal/physics/bottom/jpsi/Feb11_03/konstantin_feb11.ps

[51] K. Anikeev,
www.fnal.gov/internal/physics/bottom/jpsi/Feb11_03/konstantin_feb11.ps

[52] H. Stadie *et. al*, VXPrim in Run II, CDF internal Note 6047 (2002).

[53] CERN Application software group, MINUIT Function Minimization and Error Analysis, CERN, D506 (1998).

[54] L. Flores-Castillo *et al.*, Measurement of exclusive B lifetimes in the modes: Jpsi K+, Jpsi K*+, Jpsi K*0, and Jpsi Kshort CDF internal Note 6387, (2003).

[55] K. Anikeev *et al.*, B Meson Lifetime Measurements Using Exclusively Reconstructed Decays B $\rightarrow$ JPsi X, CDF internal Note 6266.

[56] Particle Data Group Particle Physics Booklet, July 2002.

[57] M. Bishai and S. Waschke, Optimization of Silicon Track Selection for Run II B-Fraction Measurement, CDF internal Note 6272.